



This project has received funding from the European Union's Horizon 2020 research and innovation programme under grant agreement No. 700748

## LIQUEFACT

Assessment and mitigation of liquefaction potential across Europe: a holistic approach to protect structures/ infrastructure for improved resilience to earthquake-induced liquefaction disasters.

H2020-DRA-2015

GA no. 700748



### Deliverable D4.5

#### Liquefaction mitigation techniques guidelines

(to be used for WP6 and WP7)

Author(s):	Alessandro Flora, Emilio Bilotta, Gianluca Fasano, Lucia Mele, Valeria Nappa, Anna Chiaradonna, Stefania Lirer.
Responsible Partner:	UNINA
Version:	3.0
Date:	30.01.2020
Distribution Level (CO, PU)	PU



This project has received funding from the European Union's Horizon 2020 research and innovation programme under grant agreement No. 700748

## Document Revision History

Date	Version	Editor	Comments	Status
30 April 2019	2			Final
30 January 2020	3		Final	Submitted

## List of Partners

Participant	Name	Country
ARU (Coordinator)	Anglia Ruskin University Higher Education Corporation	United Kingdom
UNIPV - Eucentre	Università degli Studi di Pavia	Italy
UPORTO	Universidade do Porto	Portugal
UNINA	Università degli Studi di Napoli Federico II.	Italy
TREVI	Trevi Società per Azioni	Italy
NORSAR	Stiftelsen Norsar	Norway
ULJ	Univerza v Ljubljani	Slovenia
UNICAS	Università degli Studi di Cassino e del Lazio Meridionale	Italy
SLP	SLP Specializirano Podjetje za Temeljenje Objektov, D.O.O, Ljubljana	Slovenia
ISMGEO	Istituto Sperimentale Modelli Geotecnici Società a Responsabilità Limitata	Italy



This project has received funding from the European Union’s Horizon 2020 research and innovation programme under grant agreement No. 700748

Istan-Uni	Istanbul Universitesi	Turkey
-----------	-----------------------	--------

## 1 CONTENTS

<b>1 MAIN GROUND IMPROVEMENT TECHNIQUES FOR THE MITIGATION OF LIQUEFACTION RISK .....</b>	<b>12</b>
1.1 GENERAL CONSIDERATIONS.....	12
1.2 DENSIFICATION.....	15
1.2.1 Dynamic compaction techniques.....	15
1.2.2 Compaction grouting .....	17
1.3 DRAINAGE.....	18
1.4 DESATURATION .....	19
<b>2 DESIGN ISSUES.....</b>	<b>21</b>
2.1 RISK OF LIQUEFACTION: A DEFINITION OF THE SAFETY FACTOR .....	21
2.2 RISK OF CRITICAL MECHANISMS BEFORE LIQUEFACTION .....	22
<b>3 PORE PRESSURE INCREMENT RATIO IN FREE FIELD CONDITIONS .....</b>	<b>24</b>
3.1 A NEW EXPRESSION FOR $r_U(FS_{LIQ,FF})$ .....	24
3.2 EXPERIMENTAL VERIFICATION OF THE SIMPLIFIED EXPRESSION OF $r_U(FS_{LIQ,FF})$ .....	29
<b>4 DESIGN APPROACHES .....</b>	<b>32</b>
<b>5 HORIZONTAL DRAINS.....</b>	<b>36</b>
5.1 INTRODUCTION .....	36
5.2 BACKGROUND ON DYNAMIC CONSOLIDATION .....	37
5.3 NUMERICAL SOLUTION OF CONSOLIDATION FOR HORIZONTAL DRAINS .....	39
5.3.1 Numerical results .....	40
5.3.2 Validation of results against FE analyses .....	46
5.3.3 Charts of excess pore pressure ratio with upper pervious surface .....	52
5.3.4 Charts of excess pore pressure ratio with upper impervious surface .....	55
5.4 DESIGN METHOD FOR HORIZONTAL DRAINS.....	58



This project has received funding from the European Union's Horizon 2020 research and innovation programme under grant agreement No. 700748

5.5	DESIGN HINTS.....	59
<b>6</b>	<b>INDUCED PARTIAL SATURATION .....</b>	<b>61</b>
6.1	INTRODUCTION .....	61
6.2	BACKGROUND ON ENERGETIC MODEL.....	61
6.3	ENERGETIC APPROACHES TO PREDICT LIQUEFACTION RESISTANCE OF UNSATURATED SANDY SOILS .....	66
6.3.1	CRR vs $q_{c1Ncs}$ for different value of $S_r$ .....	69
6.4	DESIGN METHOD FOR INDUCED PARTIAL SATURATION .....	72
6.4.1	Procedure 1: increasing CRR .....	73
6.4.2	Procedure 2: increasing $N_{liq}$ .....	73
6.5	DESIGN HINTS.....	74
	<b>REFERENCES .....</b>	<b>76</b>
<b>A.</b>	<b>Appendix A – definition of <math>q_{c1Ncs}</math> and <math>(N_1)_{60cs}</math> .....</b>	<b>87</b>
<b>B.</b>	<b>Appendix B – procedure to build the analytical expressions of <math>b(q_{c1Ncs})</math>, <math>b((N_1)_{60cs})</math>, <math>\beta(FC, q_{c1Ncs}, \Delta q_{c1N})</math>, <math>\beta(FC, (N_1)_{60cs}, \Delta(N_1)_{60})</math> .....</b>	<b>88</b>
<b>C.</b>	<b>Appendix C – HORIZONTAL DRAINS PARAMETRIC ANALYSES.....</b>	<b>92</b>
C.1	MODEL WITHOUT STRUCTURE (SINGLE LAYER).....	95
C.1.1	Efficiency in term of $r_u$ .....	95
C.1.2	Efficiency in terms of settlements .....	97
C.1.3	Local response .....	97
C.2	MODEL WITHOUT STRUCTURE (DOUBLE LAYER).....	98
C.2.1	Excess pore pressure ratio: $r_u$ .....	98
C.2.2	Efficiency in terms of $r_u$ .....	99
C.3	MODELS WITH STRUCTURE (SINGLE LAYER).....	101
C.3.1	Efficiency in term of $r_u$ .....	101
C.3.2	Efficiency in terms of settlements .....	102
C.3.3	Local response .....	103
C.4	COMPARISON BETWEEN EFFICIENCY WITHOUT AND WITH STRUCTURE .....	104
C.5	EFFECT OF HORIZONTAL EXTENSION OF DRAINAGE SYSTEM.....	105
C.5.1	Configuration $H'/d=5$ $s/d=5$ .....	106



This project has received funding from the European Union's Horizon 2020 research and innovation programme under grant agreement No. 700748

C.5.2	Configuration $H'/d=5$ $s/d=10$ .....	107
<b>D.</b>	<b>Appendix D – IPS PARAMETRIC ANALYSES.....</b>	<b>109</b>
D.1	ANALYSED SCHEMES .....	110
D.2	ANALYSES WITHOUT STRUCTURE (SINGLE LAYER) .....	112
D.2.1	Excess pore pressure ratio $r_u$ .....	112
D.2.2	Efficiency in terms of $r_u$ .....	114
D.2.3	Efficiency in terms of settlements .....	115
D.2.4	Local response .....	116
D.3	ANALYSES WITHOUT STRUCTURE (DOUBLE LAYER) .....	117
D.3.1	Excess pore pressure ratio $r_u$ .....	117
D.3.2	Efficiency in terms of $r_u$ .....	118
D.4	ANALYSES WITH STRUCTURE (SINGLE LAYER) .....	119
D.4.1	Excess pore pressure ratio: $r_u$ .....	119
D.4.2	Efficiency in terms of $r_u$ .....	121
D.4.3	Efficiency in terms of settlements .....	121
D.4.4	Local response .....	122
D.5	COMPARISON EFFICIENCY WITH AND WITHOUT STRUCTURE .....	123
D.6	EFFECT OF HORIZONTAL EXTENSION OF IPS SYSTEM .....	123
D.6.1	Excess pore pressure ratio: $r_u$ .....	124
D.6.2	Efficiency in terms of $r_u$ .....	125
D.6.3	Efficiency in terms of settlements .....	125
D.6.4	Local response .....	125



This project has received funding from the European Union's Horizon 2020 research and innovation programme under grant agreement No. 700748

## List of Figures

Figure 2.1 - Schematic representation of the possible effects of pore pressure increments for a loose (A), a medium dense (B) and a dense (C) sand, in the cases of a critical mechanism triggered by (a)  $\Delta u_{mec} < \Delta u_{liq}$  and (b)  $\Delta u_{mec} > \Delta u_{liq}$ ..... 23

Figure 3.1 - Relationships between  $r_u$  and  $FS_{liq,ff}$  based on experimental evidences (after Marcuson et al., 1990) ..... 24

Figure 3.2 - Conceptual correlation between a value of  $CRRM=7.5; \sigma'v=1$  and the correspondent cyclic resistance curve (obtained varying the magnitude M) in the CRR-N plane ..... 25

Figure 3.3 - Liquefaction factor of safety vs. the equivalent number of cycles N ..... 26

Figure 3.4 - Conceptual conversion from an irregular to a regular loading history of (a) shear stress (Seed and Idriss, 1971) and (b) pore pressure ratio (as proposed in this paper) ..... 27

Figure 3.5 - Charts with the proposed relationship between the free field pore pressure ratio,  $r_{u,ff}$  and the free field liquefaction safety factor,  $FS_{liq,ff}$  for different fine contents: (a)  $FC=0\%$ , (b)  $FC=10\%$ , (c)  $FC=20\%$  and (d)  $FC=30\%$  ..... 28

Figure 3.6 - Grain size distribution curves of the soils: Pieve di Cento sand (Mele et al., 2019), Sant'Agostino sand (Mele et al., 2018), Sendai sand (Regnier et al., 2018; OYO Corporation, 2014), Ottawa sand (El Ghoraiby et al., 2017, Vasko, 2015), Ticino sand (Mele, 2019) and Messina gravel (Flora et al., 2012)..... 29

Figure 3.7 - Cyclic resistance curves from cyclic triaxial tests on the soils of Fig. (6): Messina gravel with  $Dr = 68\%$  (Flora et al., 2012), Ticino sand with  $Dr = 40\%$  (Mele, 2019), Ottawa sand with  $Dr = 62\%$  (El Ghoraiby et al., 2017; Vasko, 2015), Pieve di Cento sand with  $Dr = 48\%$  (Mele et al., 2019), Sant'Agostino sand  $Dr = 45\%$  (Mele et al., 2018), Sendai sand with estimated  $Dr = 69\%$  (OYO Corporation, 2014) investigated in cyclic triaxial tests..... 30

Figure 3.8 - Comparison between the proposed analytical curves and the experimental data from literature for (a) Ticino sand (Mele, 2019), (b) Ottawa sand (El Ghoraiby et al., 2017; Vasko, 2015), (c) Pieve di Cento sand (Mele et al., 2019), (d) Messina gravel (Flora et al., 2012), (e) Sant'Agostino sand (Mele et al., 2018) and (f) Sendai sand (OYO Corporation, 2014) ..... 31

Figure 4.1 –Trends of how the physical processes affect the stress-based liquefaction curve (Modified from Green, 2001). See Table 4.2 for list of physical processes. .... 33

Figure 4.2 - Conceptual representation of two possible design approaches (a and b) to improve soil resistance to liquefaction. .... 35

Figure 5.1 - geometrical layout: (a) numerical model domain; (b) numerical solution domain; (c) numerical solution domain with increased  $s/d$ . .... 39

Figure 5.2 - Vertical profiles of  $r_u$  mean (continuous grey lines) and  $r_u$  max (dashed black lines) at the end of shaking, with  $Tad=50$  and  $Neq/Nl=1$ . .... 41



This project has received funding from the European Union's Horizon 2020 research and innovation programme under grant agreement No. 700748

Figure 5.3 - Vertical profiles of  $r_u$  mean (continuous grey lines) and  $r_u$  max (dashed black lines) with  $H'/d=10$  and  $s/d=10$  at the end of shaking: effect of  $N_{eq}/N_I$  with  $T_{ad}=50$ . ..... 42

Figure 5.4 - Vertical profiles of  $r_u$  mean (continuous grey lines) and  $r_u$  max (dashed black lines) with  $H'/d=10$  and  $s/d=10$  at the end of shaking: effect of  $T_{ad}$  for  $N_{eq}/N_I=1$  and 2. .... 43

Figure 5.5 - Vertical profiles of  $r_{u,max}$  at the end of shaking with  $N_{eq}/N_I=1$  and  $T_a$ . ..... 44

Figure 5.6 - Contours of excess pore pressure ratio in the solution domain at the end of shaking, with  $N_{eq}/N_I=1$ ,  $s/d=10$ ,  $T_{ad}=50$ . ..... 45

Figure 5.7 - Geometry of centrifuge test model (modified after Airoldi et al., 2018). ..... 48

Figure 5.8 - Comparison between test measurements and FEM model results: acceleration spectra; excess pore pressure history. .... 49

Figure 5.9 - Vertical profiles of excess pore pressure ratio for  $s/d$  equal to 5 and 10 at two times ( $t^*=t/t_d$ ). Continuous and dashed lines refer to Plaxis and numerical analyses, respectively. .... 51

Figure 5.10 -  $r_u$  charts for  $H'/d=5$ . (Fasano et al, 2019). ..... 52

Figure 5.11 -  $r_u$  charts for  $H'/d=10$ . (Fasano et al, 2019). ..... 53

Figure 5.12 -  $r_u$  charts for  $H'/d=15$ . (Fasano et al, 2019). ..... 54

Figure 5.13 – numerical model and solution domain for impervious upper surface. .... 55

Figure 5.14 -  $r_u$  charts for  $H'/d=5$ . (De Sarno et al, 2019). ..... 56

Figure 5.15 -  $r_u$  charts for  $H'/d=10$ . (De Sarno et al, 2019). ..... 57

Figure 5.16 - Design charts for  $H'/d=10$  and  $N_{eq}/N_I=1$  (Fasano et al, 2019). ..... 59

Figure 5.17 - Schematic effect of shallow drainage ( $H'/d=5$ ;  $s/d=5$ ). ..... 60

Figure 6.1 - Volumetric strain versus number of cycles (Mele et al., 2018). ..... 62

Figure 6.2 - Volumetric strain versus net stress for different degrees of saturation (a) and average curves (b) (Mele et al., 2018). ..... 62

Figure 6.3 - Dimensionless effective stress vs. dimensionless volumetric strain for some of the tests reported by Mele et al. (2018). ..... 63

Figure 6.4 - Experimental values of  $\sigma'_{un,liq}/\sigma'_{un,0}$  and  $S_{r0}$  (Mele et al, 2018), along with a best fitting curve (eq. 28). ..... 65

Figure 6.5 - Definition of the specific deviatoric energy  $E_{s,sk}$  for a single cycle in the  $q:\epsilon_s$  plane (Mele et al., 2018). ..... 66

Figure 6.6 - Ratio between unsaturated and saturated liquefaction resistance at  $N_{cyc}=15$  ( $\Delta CRR_{,15}^{ctx}$  and  $\Delta CRR_{,15}^{css}$ ) versus  $E_{v,liq}/p_a$  (Mele and Flora, 2019). ..... 67

Figure 6.7 - Cyclic triaxial and corrected triaxial data (Castro correlation) in the plane  $CRR \cdot (1 - 5 \cdot E_{v,liq})_{10}$  vs  $E_{s,liq}$  (Mele and Flora, 2019). ..... 68



This project has received funding from the European Union's Horizon 2020 research and innovation programme under grant agreement No. 700748

Figure 6.8 - Normalized cyclic resistance curves for cyclic triaxial and corrected data (Castro correlation) Mele and Flora, 2019). .....68

Figure 6.9 - CRR vs  $qc_{1Ncs}$  (Idriss and Boulanger, 2014).....69

Figure 6.10 - CRR vs  $qc_{1Ncs}$  for different  $S_r$ . .....72

Figure 6.11 - Possible procedures to calculate the degree of saturation needed to increment liquefaction resistance of sandy soils. On the left: procedure 1 (increase CRR); on the right: procedure 2 (increase  $N_{liq}$ ).....73

Figure C. 1 - Scheme of the adopted configurations. 92

Figure C. 2 –  $r_u$  profile every 0.5s in a vertical of the model ( $H' / d = 5$   $s / d = 5$ , without structure) .....94

Figure C. 3 - Efficiency in terms of  $r_u$  in free field conditions .....95

Figure C. 4 - Comparison of  $E_{ru}$  within 2 m from the groundwater level. ....96

Figure C. 5 - Comparison of  $E_{ru}$  within 11.5 m from the groundwater level. ....96

Figure C. 6 - Ratio between the free-field ground surface settlement with drains and without (model 17 m deep).....97

Figure C. 7 - Response spectra of models in free field conditions (13 m model).....98

Figure C. 8 – Comparison between envelopes of  $r_u$  for single and double layer. ....99

Figure C. 9 - Efficiency in terms of  $r_u$  as a function of the integration range .....100

Figure C. 10 - Efficiency in terms of  $r_u$  as a function of the integration range. ....101

Figure C. 11 - Efficiency in terms of  $r_u$  beneath the structure, along its the vertical axis. ....102

Figure C. 12 - Efficiency in terms of  $r_u$  beneath the foundation beam.....102

Figure C. 13 - Efficiency in terms of settlement in the models with structure (model 17m deep). .....103

Figure C. 14 - Pseudo-acceleration response spectra at the ground surface of models with structure.....104

Figure C. 15 - Efficiency comparison in terms of  $r_u$  between the models with structure and free field in the vertical axis foundation beam. ....105

Figure C. 16 - Schemes used to analyse the extension of the drained ground .....106

Figure C. 17 - Comparison of the efficiencies  $E_{ru}$  calculated in the various schemes of Figure C.14 for the case  $H'/d=5$   $s/d=5$ . ....106

Figure C. 18 - Efficiency in terms of settlement calculated in the various schemes of Figure C. 16 for the case  $H'/d=5$   $s/d=5$ . ....107



This project has received funding from the European Union's Horizon 2020 research and innovation programme under grant agreement No. 700748

Figure C. 19 - Comparison of the efficiencies  $E_{ru}$  calculated in the various schemes of Figure C.14 for the case  $H'/d=5$   $s/d=10$ . .....108

Figure C. 20 - Efficiency in terms of settlement calculated in the various schemes of Figure C.14 for the case  $H'/d=5$   $s/d=10$ . .....108

Figure D. 1 - Cyclic resistance curves ( $D_r=52\%$ ,  $\sigma'_{v0}=50$  KPa) with different degree of saturation and point representative of the seismic input (red dot) ..... 110

Figure D. 2 - Schematic of the numerical model with framed structure ..... 111

Figure D. 3 - Isochrones of  $r_u$  every 0.5 s (black lines) and maximum envelope (red line) ...112

Figure D. 4 - Envelopes of  $r_u$  for different value of the treated thickness,  $t_{IPS}$ . .....113

Figure D. 5 - Envelopes of  $r_u$  for different degree of saturation ( $t_{IPS}=6m$ ).....114

Figure D. 6 - Efficiency in terms of  $r_u$  as a function of the integration range .....115

Figure D. 7 - Efficiency in terms of settlements as a function of the degree of saturation. .116

Figure D. 8 - Response spectra of pseudo-acceleration at ground level for all configurations. ....116

Figure D. 9 - PGA values at ground level for all configurations .....117

Figure D. 10 – Comparison between envelopes of  $r_u$  for single and double layer layout. ....118

Figure D. 11 – Comparison between efficiency of IPS for single and double layer layout....119

Figure D. 12 - Envelopes of  $r_u$  for different value of the treated thickness,  $t_{IPS}$  (with building) .....120

Figure D. 13 - Envelopes of  $r_u$  for different degree of saturation ( $t_{IPS}=6m$ ), with building ...120

Figure D. 14 - Efficiency in terms of  $r_u$  as a function of the integration range. ....121

Figure D. 15 - Efficiency in terms of settlements as a function of the degree of saturation.121

Figure D. 16 - Response spectra at ground level for all configurations. ....122

Figure D. 17 - PGA values at the base of the structure for all configurations .....122

Figure D. 18 - Efficiency in free-field (continuous line) and with structure (dashed line) ....123

Figure D. 19 - Schematic of the numerical model:  $d_{IPS}$  is the lateral extension of the IPS layer from the building. ....124

Figure D. 20 - Envelopes of  $r_u$  for different horizontal extension of IPS.....124

Figure D. 21 - Efficiency in terms of  $r_u$  as a function of the integration range .....125

Figure D. 22 - Efficiency in terms of settlement in function of  $d_{IPS}/B$ .....125

Figure D. 23 - Response spectra at ground level for different value of  $d_{IPS}/B$ .....126



This project has received funding from the European Union's Horizon 2020 research and innovation programme under grant agreement No. 700748

Figure D. 24 - PGA values at the base of the structure for different value of  $d_{IPS}/B$ .....126



This project has received funding from the European Union's Horizon 2020 research and innovation programme under grant agreement No. 700748

## List of Tables

Table 4.1 - Approaches for increasing soil capacity and decrease demand (modified after Woeste et al., 2016).....	32
Table 5.1 - Centrifuge test calibration parameters. ....	48
Table 5.2 - Earthquake characteristics; $T_r$ is the return period, $M_w$ is the moment magnitude, $R_{ep}$ is the epicentral distance, $t_d$ is the significant duration, $a_{max}$ refers to maximum acceleration at the bottom of centrifuge model.....	48
Table 5.3 - Parameters for numerical model (*). ....	49
Table C. 1 - Layout of drains.....	93
Table D. 1 - Configurations adopted for parametric analyses.....	111



This project has received funding from the European Union's Horizon 2020 research and innovation programme under grant agreement No. 700748

## 1 MAIN GROUND IMPROVEMENT TECHNIQUES FOR THE MITIGATION OF LIQUEFACTION RISK

### 1.1 GENERAL CONSIDERATIONS

Soil liquefaction continues to be a major source of damage to buildings and infrastructure after major earthquake events, resulting in loss of human life as well as in economic losses all over the world (Bardet, Idriss, & O'Rourke, 1997; Ferritto, 1997; Seed et al., 2003). Damage is related both to the horizontal ground displacements caused by liquefaction of loose granular soils, as illustrated in several case studies in the United States and Japan (O'Rourke and Hamada, 1992; Hamada and O'Rourke, 1992), and to the transient loss of shear strength of the soil that induces sudden, large vertical displacements as well as overall instabilities.

Ground improvement methods are widely used at many sites worldwide as a way of mitigating liquefaction damage. A detailed list of all the possible choices in terms of ground improvement and of all the contributions in literature is basically impossible, because a very large number of literature contributions and site experiences exist nowadays. However, in most cases ground improvement techniques are used with a rule of thumb approach, thus without following a completely rational path. There is therefore the strong need to put together the existing knowledge in terms of processes, technology and design to allow a more sound approach to the mitigation of liquefaction risk.

The relative success of ground improvement methods in preventing damage caused by a liquefaction event and the mechanisms by which they can mitigate liquefaction continue to be areas of active research. Recent earthquakes in Turkey, Greece, Taiwan and India have highlighted the need to understand the complex behaviour of civil engineering structures when subjected to powerful earthquake vibrations. The Bhuj (India) earthquake of 26 January 2001 highlighted some of the complex problems associated with the liquefaction of ground. For example, a bridge site near the towns of Bhachau and Vondh during the Bhuj earthquake suffered excessive liquefaction. At this site four bridges cross the river channel, which has clearly liquefied, with extensive sand boiling being observed next to the piers. The ground motion at the site was approximately parallel to the longitudinal axis of the bridges. Liquefaction of the foundations led to rotation of the piers of the plate girder bridge. This type of damage was widespread in this earthquake, and many bridges, ports and earth dams suffered as a result of liquefaction-induced settlements and rotations. Similar damage has been observed in other major earthquakes, such as those in 1999 in Greece, Taiwan and Turkey. For example, in Turkey the Adapazari area suffered extensive liquefaction. These examples briefly illustrate some liquefaction-induced damage suffered by structures. Using site investigations it is possible to establish sites that are particularly vulnerable to liquefaction. Subsequent to this, the need to choose a suitable liquefaction remediation measure arises. The particular choice of a ground improvement method may be determined



This project has received funding from the European Union's Horizon 2020 research and innovation programme under grant agreement No. 700748

by the class of structure that is envisaged at the site (cost considerations, technical feasibility etc).

Before entering in more detail into the ground improvement techniques, it is useful to clarify that generally speaking two possible approaches are possible to mitigate liquefaction risk. Specifically, the two main following categories can be identified:

- i) methods aimed at modifying the seismic demand on structures by reducing the site susceptibility to liquefaction;
- ii) methods aimed at enhancing the capacity of structures to prevent their collapse if the ground should liquefy.

The first category includes techniques that improve the liquefaction strength of the soil, usually by one or more of the following factors:

- 1- densification of the liquefiable soil (to be achieved with any kind of compaction)
- 2- stabilization of soil skeleton (to be achieved by different actions)
- 3- immediate dissipation of increased excess pore pressure (by improving drainage capacity)
- 4- desaturation of the liquefiable soil

Appropriate countermeasures in the second category differ by the type of structure. Structural mitigation for liquefaction may be more economical than soil improvement but may slightly impact or have no effect on the soil itself; thus structural mitigation may not reduce the potential of the soils to liquefy during an earthquake and liquefaction and related ground deformations will still occur. While liquefaction has been widely recognized as one of the principal earthquake hazards, it is important to understand and identify key factors that may contribute to the extensive damage of existing structures. The choice of mitigation methods and the selection of proper strengthening techniques will depend on the extent of liquefaction and the related consequences. Youd (1998) has suggested that structural mitigation for liquefaction hazards may be acceptable in the case of small lateral displacements (i.e. less than 0.3 meter) and vertical settlement (i.e. less than 10 centimeters).

Soil liquefaction adversely affects the performance of structures resulting in total and differential settlements, which lead to serious foundation and structural damage, lateral movement of foundations, and bearing failures. The performances of an existing structure can be enhanced in different ways by increasing the structural capacity in terms of ductility, stiffness or strength (separately or, in many cases, at the same time) or by reducing the seismic demand. The most common strategies adopted in the field of seismic retrofit of existing structures are the restriction or change of use, partial demolition and/or mass reduction, removal or lessening of existing irregularities and discontinuities, addition of new



This project has received funding from the European Union's Horizon 2020 research and innovation programme under grant agreement No. 700748

lateral load resisting systems, local or global modification of elements and systems, seismic demand reduction by means of base isolators or steel dissipating braces. Against liquefaction, mitigation techniques based on the structural capacity increase should aim at providing an extra ductility in order to provide the ability to accommodate large deformations. Although many factors influence the selection of the most appropriate technique and therefore no general rules can be defined, an effective strategy could be based on local modification of components that are inadequate in terms of deformation capacity. In particular, local strengthening methods are meant to increase the deformation capacity of deficient components, so that they will not attain their specified limit state under the design seismic excitation. This could allow to significantly increase the structural global deformation capacity even under limited budget constraint. Common approaches mainly include steel or RC jacketing and externally bonded Fiber Reinforced Polymers (FRP) wrapping. Local strengthening could increase the seismic capacity of one or more under-designed components without affecting the overall response mechanism of the structure. This strategy represents a fast and cost-effective improvement in seismic performance and could require only the assessment of local components capacity increase. Indeed, the global analysis to check the attainment of a specific performance level is not required, provided that global mass and structural stiffness are not significantly affected by the local strengthening intervention. Nowadays, the use of externally bonded FRPs has become a common rehabilitation measure in the field of local modification of components since their use is regarded as a selective intervention aiming at increasing the ductility (or the chord rotation capacity) of critical zones of beams and columns through FRP wrapping (confinement) and the shear strength of members and of partially confined beam-column joints, fib Bulletin 14 2003, CNR DT-200/2004, ACI 440.2R-08. The confinement at columns and beams ends, at location where plastic deformation are commonly attained in case of large deformations, could significantly improve members ductility and then the global structural ductility. The shear strengthening of unconfined joint could allow to fully exploit such ductility that is essential to meet large deformation induced by differential settlements. Several experimental studies have confirmed that FRP strengthening interventions could be effective to achieve this goal (Antonopoulos and Triantafillou 2003, Prota et al. 2004, Engindeniz, et al. 2005, Di Ludovico et al. 2008a, b, Boussethahm 2010, and Akguzel and Pampanin 2012).

Ductility has been also acknowledged as a critical issue when related to infrastructures and lifelines. In fact, soil liquefaction can also induce localized deformation to supports of distributed structural systems, such as drainage and water supplying systems. In this case, ductility can prevent structural damages and consequent loss of performance. This topic has been already investigated in scientific literature, where vulnerability and fragility curves have been derived for different distributed structural systems (Pitilakis et al. 2006, Der Kiureghian, A. 2002, et al. 2014, Kakderi & Argyroudis 2014).



This project has received funding from the European Union's Horizon 2020 research and innovation programme under grant agreement No. 700748

Moderate to severe liquefaction may affect many high-rise buildings on shallow foundations and deep foundations in different ways. As an example, in the case of shallow foundations on liquefiable soils, piles can be added to transfer loads to deeper non liquefiable soil; pile foundation can be strengthened by increasing the number of piles and spreading the foundation. In the case of buried structures, methods of remediation which are mostly used are lift prevention piles, compaction grout column, jet grouting, soil cement wall and drain pile, whereas in the case of buried pipelines flexible joints absorbing ground deformations can also be adopted.

In the case of construction with shallow foundations, an important strengthening strategy is based on the connection of all the elements of the foundation. This ensures that the foundation moves and settles in a uniform matter, consequently reducing the shear forces upon the structure overlying the foundation. Stiff foundation mats are a good method for mitigating liquefaction for shallow foundations. A stiff foundation mat can transfer loads from areas of weakness to areas of strength in the soil, thus reducing the potential for damage to the structure. Additionally, it is important to have ductile connections of utility lines that are buried in liquefiable soils in order to allow for deformation and movement of the soil without causing breaks or leaks in utility lines.

The selection of the approach and of the technology largely depends on site conditions and on the structure or infrastructure to protect: in case this is a new one and no sensible structures are in the surrounding, in principle any technique that is feasible for the specific soil characteristics may be adopted. If an existing structure has to be protected, techniques selected to improve the ground surrounding or adjacent to existing structures should be those that would not cause excessive level of disturbance. Special machines without noise and vibrations should be used in this case. One densification technique that produces low levels of vibration during installation is compaction grouting; other low vibration techniques that improve primarily by solidification are permeation grouting, jet grouting, and in situ soil mixing .

Remediation techniques of the second category can be easily applied to existing structures. In this case the allowable deformations of the structures must be defined because the strengthening effect must be judged based on the deformations of the structure. This means that a performance-based design has been undertaken.

## 1.2 DENSIFICATION

### 1.2.1 Dynamic compaction techniques

The most commonly used ground improvement techniques for liquefaction remediation at new construction sites are vibro-compaction, vibro-replacement, dynamic compaction, deep blasting and sand compaction pile (Hayden and Baez, 1994; JGS, 1998). These techniques



This project has received funding from the European Union's Horizon 2020 research and innovation programme under grant agreement No. 700748

improve the ground “primarily by densification and are typically less expensive than other techniques. However, they can produce objectionable levels of work vibration.

Dynamic densification has been extensively used as a liquefaction resistance measure, following the evidence that denser granular soils show a lower tendency to generate excess pore pressure during cyclic loading than equivalent loose deposits. The merit of this technique can be corroborated by the enhanced field performance of improved sites compared with adjacent non-improved sites recorded in past earthquakes, as described in detail by Mitchell et al. (1995) and Hausler and Sitar (2001), among others. In order to minimize earthquake-induced liquefaction risk for bridge foundations as well as other structures, ground remediation techniques have been extensively used to improve the performance of liquefiable soils.

Zen et al. (1997) and Mitchell et al. (1998), reviewing field applications of this technique, assert that it is usually possible to densify the soil to an average value of relative density of about 80%, the effectiveness of the different techniques being affected by the amount of fines in the deposit. In terms of the improvement depth, Mitchell et al. (1998) recommend that densification of the ground beneath a structure should be extended to the bottom of the liquefiable layer. Zen et al. (1997), however, argue that there are no case histories of liquefaction occurring below a depth of 20 m, although the reasons behind that fact are not completely understood. Despite the scientific relevance of this issue, its practical implications are minor, as the costs of densification depend much more on the lateral extent of the improvement zone than on its depth. In addition, modern equipment available for vibro-compaction makes it possible, if required, to densify granular deposits up to a depth of 35 m, according to Moseley and Priebe (1993).

Soil densification is generally considered highly reliable, and the standard remedial measure against liquefaction. It reduces the void space of the soil, thereby decreasing the potential for volumetric change that would lead to liquefaction. Resistance to shear deformation also increases with increased density. Several sites improved by densification performed well during the 1964 Niigata, Japan, 1978 Miyagiken-oki, Japan, 1989 Loma Prieta, California, and 1994 Northridge, California, earthquakes (Watanabe, 1966; Ishihara et al., 1980; Mitchell and Wentz, 1991; Graf, 1992a; Hayden and Baez, 1994).

Stamatopoulos et al. (2011) presented a research project specially focused on the developing countries with scarce technology for ground improvement, with the aim to develop design rules for the use of preloading as a mitigating measure against soil liquefaction. The test field located in Albania near Durres was presented with data from 4 boreholes (SPT values, fines content, plasticity index) and estimated factors of safety for an earthquake with a magnitude  $M=6$  and maximum acceleration at the surface  $a_{max}=0.26g$  and alternatively  $a_{max}=0.35g$ . It was calculated that the soil between depths from 6 to 15 m are susceptible to liquefaction in their original state. In Albania, recently the vibro stone columns were introduced and used for the first time in the Ferry Terminal of Durres (Kosho, 2011).



This project has received funding from the European Union's Horizon 2020 research and innovation programme under grant agreement No. 700748

Lalić (2006) presented in many details the method of soil improvement by explosives that was successfully used also in Croatia for the breakwater construction. This method is of particular interest since it is technically and cost effective in fully saturated cohesive and cohesionless soils up to large depths (40 m) and on large surface areas. The obvious shortcoming of the method is its limitation to unpopulated areas.

The use of stone columns to tackle liquefaction risk is very promising: the columns provide drainage, densify the surrounding soil during installation, and may act as rigid inclusions, even though their stiffness and strength are obviously well below those of piles. However, if properly design, they do have the positive effect, even under static loads, to reduce settlements and improve the bearing capacity of the foundation system. Recently, the performance of such columns has been enhanced by encasing them in geotextiles, that improve their stiffness by lateral confinement. and their drainage capacity avoiding occlusion by fine content of surrounding soil.

### 1.2.2 Compaction grouting

Compaction grouting is a technique to densify and thus increase the strength of loose, liquefaction susceptible soils. Compaction grouting involves the injection of a very stiff grout (normally a cement-water mixture) that does not permeate the native soil, but results in the controlled growth of a grout bulb mass that displaces the surrounding soil. The compaction grout is injected through grout pipes (typically 5-10 cm in diameter) that are progressively inserted or withdrawn from a soil mass such that a grout column or series of bulbs is created over the treated depth interval. First, a grout pipe casing is driven into the ground to reach the susceptible soil. Then, as the pipe is withdrawn in stages, a stiff cement grout mixture is pumped through the pipe and is extruded from the tip at each stage to form expanding grout bulbs within the soil mass. The bulbs of grout displace the adjoining soil and densify the immediately surrounding zone. The grout bulbs inherently densify the loosest soil in the vicinity of the grout pipe and thus treat the most susceptible material.

The vast majority of compaction-grouting experience has involved arresting, eliminating, or reversing foundation settlements. Because the success of a settlement related application is often evident as the work progresses, there is generally no incentive to directly quantify the effects of compaction grouting on the treated soil.

One of the principal advantages of compaction grouting is that its maximum effect is in the weakest soil zone (Brown and Warner 1973). In addition, it is effective in fine-grained soils that were formerly considered ungroutable (Brown and Warner 1973). A primary use of compaction grouting has been to compact loose fills or natural loose soils, underpin structures that have suffered differential settlement, and lift the structure, foundation, and subgrade to level (Graf 1969, 1992). It has also been used for improving in situ soils to reduce the liquefaction potential during earthquakes (Boulanger and Hayden 1995), and as a



This project has received funding from the European Union's Horizon 2020 research and innovation programme under grant agreement No. 700748

construction tool to limit ground movement during soft ground tunnelling (Baker, 1982). Compaction grouting involves a set of complex parameters due to different possible soil conditions as well as grouting variables, e.g., grout hole spacing, grouting stage length, injection rate, limiting injection pressure, injection pipe diameter, and so forth. The application of the method, however, relied heavily on practical experience and empiricism.

### 1.3 DRAINAGE

Another common ground improvement method that is used to mitigate liquefaction-induced damage is the installation of drains. Many kinds of technologies to realize a drainage system are available in the engineer practices. Preformed drains or stone columns can be installed by vibro-replacement or auger-casing. In the vibro-replacement technique the potential for liquefaction is mitigated by increasing the density of soil surrounding drains, allowing drainage for the control of pore pressures, introducing stiff elements (stone columns) which can potentially carry higher stress levels causing reduction in stress levels in the surrounding soil (Priebe, 1989, 1991), and providing a deformation restricting effect. The typical auger-casing system instead generally involves little or no densification. However, current Japanese practice involves an auger-casing with an internal gravel feeding and compaction-rod system, thus adding the important densification effect (Ono et al. 1991). Systems for installing synthetic drains have also been developed (JGS, 1998). The low vibration drain pile technique has been used in Japan for liquefaction remediation near existing structures. Following the 1993 Kushiro-Oki, Japan, earthquake, Iai et al. (1994a, 1994b) observed that quay walls having back fill treated by the gravel drain pile and sand compaction pile techniques suffered no damage, while quay walls having untreated backfill were severely damaged due to liquefaction.

Mitchell et al. (1995) and Hausler and Sitar (2001) document some of the sites where drains were used as a liquefaction mitigation measure. They report that, following moderate-sized earthquakes, these sites performed better than comparable unimproved sites. Design of drains in practice is guided by the seminal work carried out by Seed and Booker (1977), who developed design charts for the drain radius and drain spacing based on analytical methods. These charts are used depending on the site conditions, the hydraulic conductivity of the site and the drain material. The main assumptions of Seed and Booker's work include the fact that the individual drains called 'unit cells' are part of an infinite number of drain groups: that is, every drain is surrounded by identical drains in all directions. However, real field drains would of course have boundaries. The drains can be divided into internal drains, sub-perimeter drains and perimeter drains. The behaviour of internal drains would be close to the unit cell assumption made by Seed and Booker. However, the sub-perimeter and perimeter drains would behave quite differently from the unit cell drains. Traditional ground improvement



This project has received funding from the European Union's Horizon 2020 research and innovation programme under grant agreement No. 700748

using drains was carried out by installing stone columns or drains with similar high-permeability materials.

Shaking table tests (starting from the old but still actual work carried out by Sasaki and Taniguchi, 1982) indicate that gravel drains can accelerate the dissipation of excess pore water pressures, thereby limiting the loss of shear strength and reducing the uplift pressures acting on buried structures. At Cambridge, centrifuge modelling (Brennan and Madabhushi, 2006) has been carried out to investigate the mechanism by which drains affect the performance of a liquefiable site. It is generally agreed that the drains bring about a positive effect by relieving the excess pore pressures that are generated during an earthquake. The main question in this regard is whether the additional drainage is able to prevent the generation of full excess pore pressures, or whether they merely help to dissipate excess pore pressures quickly after the earthquake loading: that is, full excess pore pressures will be generated, but the duration for which a site stays fully liquefied will be reduced. Most of the past studies have been focused on the drainage characteristics of stone columns. However, recent experimental and analytical research have shown that a major gain from stone columns lies in their ability in: (i) densifying surrounding soils during construction, (ii) restricting shear deformation and offering containment of the “encapsulated” soils, and (iii) providing stiffening-matrix effects (i.e., reducing the stresses in adjacent soil).

Increasing the rate of consolidation by soil drainage with either prefabricated wick drains, stone columns or their combination is a well adopted technique and widely used in most of SE European countries. It is a rare topic in papers, as it appears to be a matter of professional routine and not a subject of current research.

#### 1.4 DESATURATION

Some recent studies have shown that the inclusion of gas bubbles in soil leads to a reduction in the degree of saturation and an increase in the liquefaction resistance of sand (Copp, 2003; Pietruszczak et al., 2003; Okamura & Soga, 2006; Okamura & Teraoka, 2006; Okamura et al., 2006, 2011; Yegian et al., 2006, 2007; Pande & Pietruszczak, 2008). Several methods have been proposed to introduce gas bubbles into sand. These include (a) air injection (Okamura et al., 2011) (b) water electrolysis (Yegian et al., 2006) (c) sand compaction pile (Okamura et al., 2006) (d) use of sodium perborate (Eseller-Bayat, 2009).

Yegian et al (2007) proposed a system for providing a partial level of saturation to a mass of sand, through generation of gas bubbles. The system includes a solution that is operable to generate gas bubbles and a solution generator that prepares the solution. A conduit delivers the solution to the sand, so that the solution generates the gas bubbles during and after being delivered to the sand. A probe may be used to determine whether the sand is susceptible to liquefaction before the solution is delivered and to assess a change in degree of partial saturation after the solution has been delivered. The systems and methods are based on



This project has received funding from the European Union's Horizon 2020 research and innovation programme under grant agreement No. 700748

injection of a dissolved, ecofriendly chemical, which reacts and generates gas over time in saturated sand. The technique can be applied safely at a new site as well as underneath existing structures, without causing disturbance and distress to the structure.

In recent years, attempts have been made to apply microbiology to geotechnical engineering. Most of these studies have been focused on either enhancement of shear strength (De Jong et al., 2006; Whiffin et al., 2007; Ivanov & Chu, 2008; Harkes et al., 2010) or reduction of permeability of soil (Stabnikov et al., 2011; Chu et al., 2012) by induction of calcite crystallization using microbial hydrolysis of urea. Another potential application of biotechnologies in geotechnical engineering is to mitigate liquefaction hazard of saturated sand deposits by formation of tiny gas bubbles in situ using a microbial denitrification (i.e. nitrate reduction) process. Biogas will offer another method for mitigation of liquefaction after it has been established. An important question regarding the desaturation method is whether or not gas bubbles in sands can remain for a long time. According to Yegian et al. (2007), within a duration of 442 days, there was little change in the degree of saturation (from 82.1% to 83.9%) under hydrostatic conditions. Similar tests were also carried out by He (2013) using biogas. The result was similar to that in Yegian et al. (2007). Thus, the tiny gas bubbles generated by bacteria will be stable at least under hydrostatic conditions. For the biogas method adopted, nitrogen gas was generated through a dissimilatory reduction of nitrate, or in common terms, denitrification.



This project has received funding from the European Union's Horizon 2020 research and innovation programme under grant agreement No. 700748

## 2 DESIGN ISSUES

### 2.1 RISK OF LIQUEFACTION: A DEFINITION OF THE SAFETY FACTOR

Ground improvement techniques are effective in mitigating liquefaction risk in a number of ways. They can increase the strength and stiffness of the soil, thus preventing contraction of the soil skeleton and reducing pore pressure increase, or directly focus on the dissipation or reduction of excess pore pressures to prevent the reduction in effective stresses during the earthquake. For both of these cases, the factor of safety against liquefaction is typically used as a proxy for evaluation.

Codes of practice usually make explicit reference to a factor of safety in free field conditions ( $FS_{liq,ff}$ ) defined with a stress-based procedure (Seed and Idriss, 1971) as the ratio between the seismic loading required to trigger liquefaction and the one expected from the earthquake. Typically, both the liquefaction resistance and the seismic demand are written as cyclic stress ratios (respectively CRR and CSR), and the factor of safety is expressed as:

$$FS_{liq,ff} = \frac{CRR}{CSR} = \left( \frac{CRR_{M=7.5, \sigma'_v=1}}{CSR} \right) \cdot MSF \cdot K_{\sigma} \cdot K_{\alpha} \quad (1)$$

where  $CRR_{M=7.5, \sigma'_v=1}$  is the resistance referred to a magnitude  $M=7.5$  and to  $\sigma'_v=103$  kPa,  $MSF$  is the magnitude scaling factor, introduced to account for the effect of the duration of the seismic event,  $K_{\sigma}$  and  $K_{\alpha}$  are correcting factors to account respectively for the effective overburden stress and for an initial static shear stress on the horizontal plane. The expressions of all the factors of equation (1) are not reported here for the sake of brevity, and can be easily found in literature (e.g., National Academies, 2016).

A comprehensive review of CPT-based and SPT-based liquefaction triggering procedures is reported by Boulanger and Idriss (2014), who proposed charts to quantify the cyclic resistance ratio  $CRR_{M=7.5, \sigma'_v=1}$  as:

$$CRR_{M=7.5, \sigma'_v=1} = \exp \left( \frac{q_{c1Ncs}}{113} + \left( \frac{q_{c1Ncs}}{1000} \right)^2 - \left( \frac{q_{c1Ncs}}{140} \right)^3 + \left( \frac{q_{c1Ncs}}{137} \right)^4 - 2.8 \right) \quad (2a)$$

$$CRR_{M=7.5, \sigma'_v=1} = \exp \left( \frac{(N_1)_{60cs}}{14.1} + \left( \frac{(N_1)_{60cs}}{126} \right)^2 - \left( \frac{(N_1)_{60cs}}{23.6} \right)^3 + \left( \frac{(N_1)_{60cs}}{25.4} \right)^4 - 2.8 \right) \quad (2b)$$

where  $q_{c1Ncs}$  and  $(N_1)_{60cs}$  are the corrected CPT tip resistance and the corrected SPT blow count (defined in Appendix A).



This project has received funding from the European Union's Horizon 2020 research and innovation programme under grant agreement No. 700748

In the simplified procedure, CSR is usually expressed as:

$$CSR = 0.65 \frac{\tau_{\max}}{\sigma'_v} = 0.65 \cdot \frac{a_{\max}}{g} \cdot \frac{\sigma_v}{\sigma'_v} \cdot r_d \quad (3)$$

where the coefficient 0.65 is introduced to transform the irregular shear stress history (represented by  $\tau_{\max}$ ) in one having an equivalent constant shear stress amplitude,  $\sigma_v$  and  $\sigma'_v$  are the vertical total and effective stresses at a depth  $z$ ,  $a_{\max}$  is the maximum horizontal acceleration,  $g$  is the gravity acceleration and  $r_d$  is a shear stress reduction factor accounting for soil deformability, whose expression can be found in Boulanger and Idriss (2014).

At a generic depth  $z$ , the assessment of the liquefaction potential is done by verifying that

$$FS_{liq,ff} \leq FS_{liq,ff,min} \quad (4)$$

Where  $FS_{liq,ff,min}$  is the minimum tolerable value, according to Code's indications.

## 2.2 RISK OF CRITICAL MECHANISMS BEFORE LIQUEFACTION

Once  $FS_{liq,ff}$  is estimated with equation (1), and a related site integral indicator of liquefaction potential like the Liquefaction Potential Index LPI (Iwasaki et al., 1984) or the Liquefaction Severity Number LSN (Van Ballegoy et al., 2014) is quantified, a designer will be satisfied if a minor risk of liquefaction results from calculation. However, with this approach nothing is known on seismically induced pore pressure increments  $\Delta u$  that, even if not causing liquefaction, reduce soil stiffness and shear strength. These reductions induce settlements and reduce bearing capacity safety margins for existing structures (e.g., Cascone and Bouckovalas, 1998; Karamitros et al. 2013), possibly triggering for them unforeseen limit states.

Figure 2.1 reproduces schematically the possible effects of pore pressure increments in different soils and different situations, when a building is founded on a liquefiable soil. In Figure 2.1a, no other critical mechanism than liquefaction is possible. Then, the loose soil (A) will need to be improved, while for the medium dens (B) and dense (C) nothing has to be done, as long as the safety conditions prescribed by the ruling code have been satisfied.

Figure 2.1b depicts a situation in which the pore pressure increment leading to a critical mechanism is lower than that leading to liquefaction ( $r_u=1$ ); then, for the case represented in the figure the building on the loose (A) and on the medium dense (B) sand will need to be verified with reference to the relevant critical mechanism (for instance, bearing capacity



This project has received funding from the European Union's Horizon 2020 research and innovation programme under grant agreement No. 700748

failure). If ground improvement is adopted to reduce  $\Delta u$  to values lower than  $\Delta u_{mec}$ , the design process is complete.

While the values of the pore pressure increments caused by the seismic action  $\Delta u$  are of relatively minor interest if only the liquefaction potential has to be checked (via the safety factor  $FS_{liq,ff}$ ), it becomes of the utmost importance to estimate them if a critical mechanism is possible before liquefaction. In this latter case, two issues have to be faced: the estimate of  $\Delta u_{mec}$  and that of  $\Delta u$ . Actually, with reference to the second issue, what is of interest to the designer is not the knowledge of the free field value  $\Delta u_{ff}$  (or of the equivalent  $r_{u,ff}$ ) but the knowledge of the distribution of pore pressure increments (or an average value) underneath the foundation or the geotechnical structure to protect,  $\Delta u_{found}$  ( $r_{u,found}$ ).

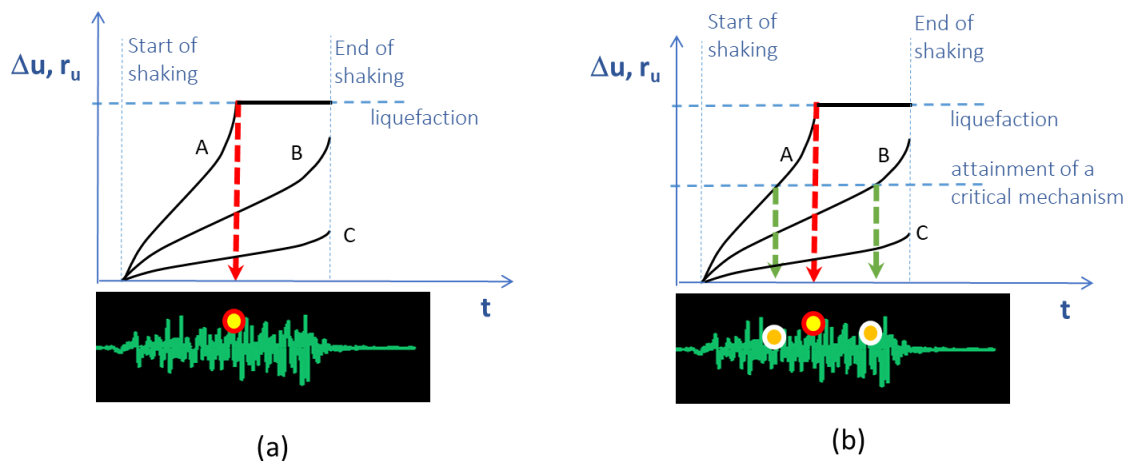


Figure 2.1 - Schematic representation of the possible effects of pore pressure increments for a loose (A), a medium dense (B) and a dense (C) sand, in the cases of a critical mechanism triggered by (a)  $\Delta u_{mec} < \Delta u_{liq}$  and (b)  $\Delta u_{mec} > \Delta u_{liq}$ .



This project has received funding from the European Union's Horizon 2020 research and innovation programme under grant agreement No. 700748

### 3 PORE PRESSURE INCREMENT RATIO IN FREE FIELD CONDITIONS

#### 3.1 A NEW EXPRESSION FOR $r_u(FS_{liq,ff})$

As previously mentioned, there are situations in which it is needed to estimate  $\Delta u_{ff}$  in free field conditions before liquefaction. Few indications exist in literature, all attempting to correlate  $\Delta u_{ff}$  to  $FS_{liq,ff}$  Iwasaki et al. (1984) proposed the empirical correlation:

$$r_{u,ff} = FS_{liq,ff}^{-1/b} \quad (5)$$

where  $r_{u,ff}$  is the pore pressure ratio (defined as the ratio between  $\Delta u_{ff}$  and the initial effective overburden stress,  $\sigma'_{v0}$ ) and  $b$  is one of the two parameters needed to define the cyclic resistance curve of a soil, as explained in the following. Equation (5) is of limited practical interest if values of  $b$  are not given as a function of soil intrinsic and state properties. The new equation proposed in the following, which stems from considerations in all similar to the ones done by Iwasaki et al. (1984), in particular, is more sound as it is not only based on the shape of the cyclic resistance curve, but also on the way pore pressures build up during the cyclic shaking, which in turn depends on soil grading and relative density. Marcuson et al. (1990) have collected laboratory data on gravels and sands and have produced a qualitative chart to estimate  $r_{u,ff}(FS_{liq,ff})$  (Figure 3.1) depending on soil grading. Again, this chart is of limited interest, as it indicates wide ranges of  $r_{u,ff}$  for a given value of  $FS_{liq,ff}$ .

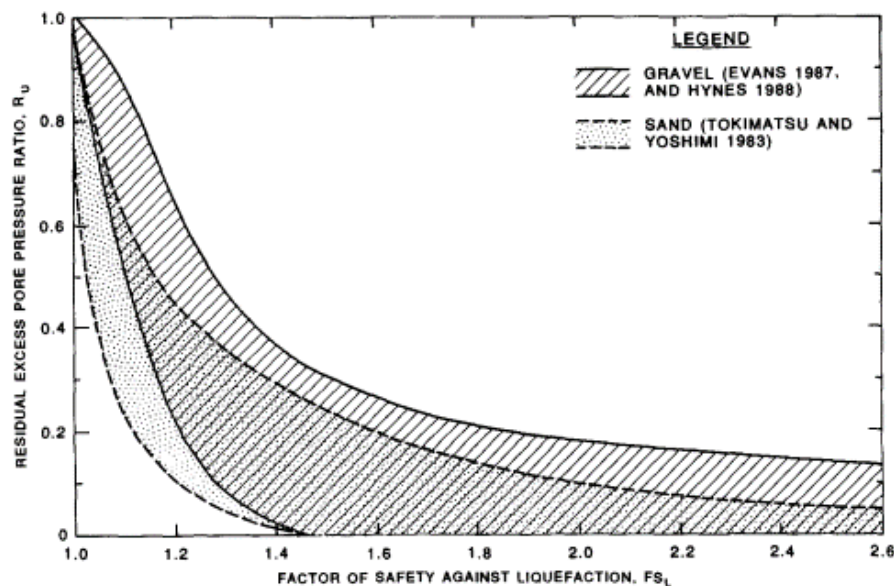


Figure 3.1 - Relationships between  $r_u$  and  $FS_{liq,ff}$  based on experimental evidences (after Marcuson et al., 1990)



This project has received funding from the European Union's Horizon 2020 research and innovation programme under grant agreement No. 700748

Equation (6) says that any value of  $CRR_{M=7.5, \sigma'_v=1}$ , which is a function of  $q_{c1Ncs}$  or  $(N_1)_{60cs}$ , represents a whole cyclic resistance curve in the CRR vs. N plane, once a value of the effective overburden stress,  $\sigma'_v$ , is given and a relationship between the magnitude, M, and an equivalent number of cycles, N, is assumed (Figure 3.2). The latter has been dealt with in a number of papers (Cubrinovski et al., 2018), and is affected by some uncertainty. As will be shown in the following, however, in this work there is no need to express such a relationship, and therefore this uncertainty is not a matter of concern.

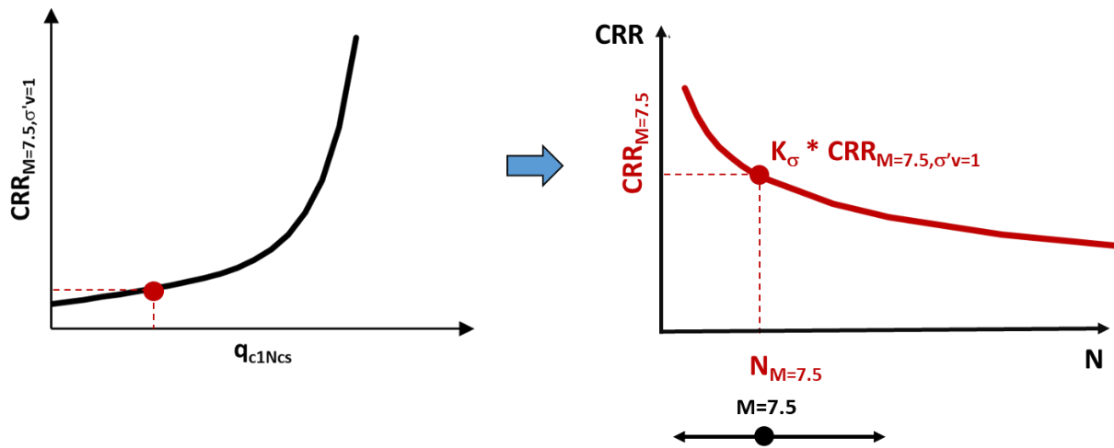


Figure 3.2 - Conceptual correlation between a value of  $CRR_{M=7.5; \sigma'_v=1}$  and the correspondent cyclic resistance curve (obtained varying the magnitude M) in the CRR-N plane

The CRR(N) relationship can be simply expressed with a power function (Idriss and Boulanger, 2008) as:

$$CRR = a \cdot N^{-b} \quad (6)$$

where the coefficient a and the exponent b depend on soil physical and mechanical properties (via  $q_{c1Ncs}$ ) and on  $\sigma'_v$ :

$$a, b = f(q_{c1Ncs}, \sigma'_v) \quad (7)$$

Combining equations (1) and (6):

$$FS_{liq,ff} = a' \cdot N^{-b} \quad (8)$$



This project has received funding from the European Union's Horizon 2020 research and innovation programme under grant agreement No. 700748

in which:

$$a' = \frac{a}{CSR} = f(CSR, q_{clNcs}, \sigma'_v) \quad (9)$$

Obviously, at liquefaction (i.e. for  $N=N_L$ )  $FS_{liq,ff} = 1$ . For  $N < N_L$ ,  $FS_{liq,ff} > 1$  (Figure 3). Then, equation (8) can be conveniently rearranged as:

$$FS_{liq,ff} = \left( \frac{N}{N_L} \right)^{-b} \quad (10)$$

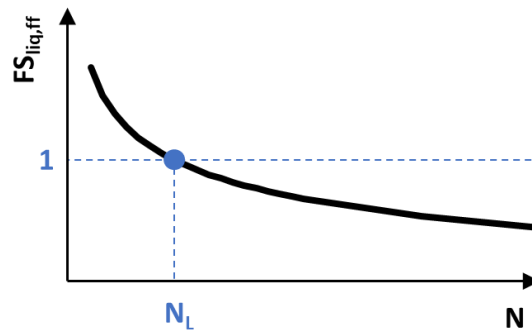


Figure 3.3 - Liquefaction factor of safety vs. the equivalent number of cycles  $N$

Once such a simple expression of the safety factor is available, there is the need to link  $r_u$  to the same independent variable ( $N/N_L$ ). In principle, this is not an easy task, as the irregular seismic shaking leads to an irregular pore pressure build-up history. However, as proposed by Chiaradonna and Flora (2019) a simplification can be introduced considering a regular  $\Delta u$  build-up history (Figure 4), similarly to what has been proposed by Seed and Idriss (1971) to calculate CSR considering instead of the irregular shear stress history caused by the earthquake an equivalent constant amplitude cyclic shear stress (equation 3).



This project has received funding from the European Union's Horizon 2020 research and innovation programme under grant agreement No. 700748

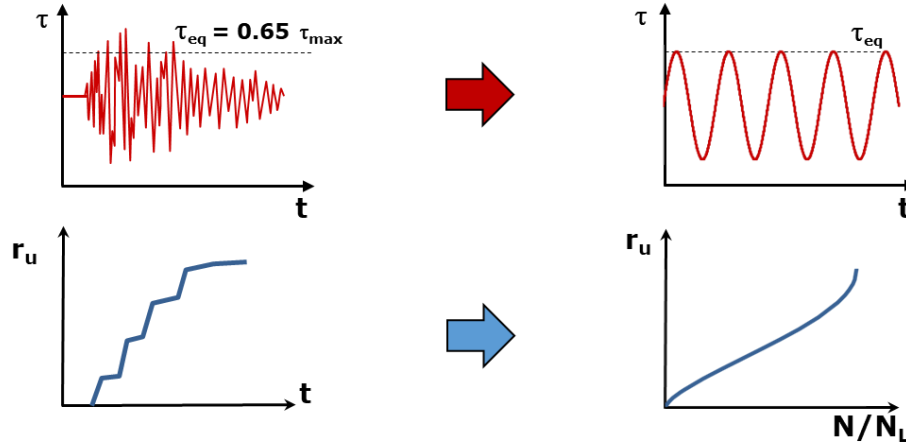


Figure 3.4 - Conceptual conversion from an irregular to a regular loading history of (a) shear stress (Seed and Idriss, 1971) and (b) pore pressure ratio (as proposed in this paper)

The analytical relationship  $r_{u,ff}(N/N_L)$  proposed by Booker et al. (1976) has been used in this work:

$$r_{u,ff} = \frac{2}{\pi} \arcsin \left( \frac{N}{N_L} \right)^{1/2\beta} \quad \text{with } r_{u,ff} \leq 1 \quad (11)$$

in which the parameter  $\beta$  depends on soil physical and mechanical properties. Then, by combining equations (10) and (11), it results:

$$r_{u,ff} = \frac{2}{\pi} \arcsin \left( FS_{liq,ff}^{-\frac{1}{2b\beta}} \right) \quad \text{with } FS_{liq,ff} \geq 1 \quad (12)$$

which is the equation proposed by Chiaradonna and Flora (2019), needed to link the pore pressure ratio  $r_u$  to the current safety factor  $FS_{liq,ff}$  before liquefaction. As previously mentioned, by combining the two equations the formal dependence on the ratio  $N/N_L$  disappears, allowing to overlook the complex issue of relating the equivalent number of cycles,  $N$ , to earthquake magnitude.

In order to make equation (12) of practical use, a procedure has been implemented to link the parameters  $b$  and  $\beta$  to soil grading and density, via the normalized resistances  $q_{c1Ncs}$  and  $\Delta q_{c1N}$ , or  $(N1)_{60cs}$  and  $\Delta(N1)_{60}$ , and the fine content  $FC$  (see Appendix A for the definitions). In detail,  $b$  and  $\beta$  can be expressed as:



This project has received funding from the European Union's Horizon 2020 research and innovation programme under grant agreement No. 700748

$$b = -1.487 \cdot 10^{-8} \cdot q_{c1Ncs}^3 + 1.291 \cdot 10^{-5} \cdot q_{c1Ncs}^2 - 5.722 \cdot 10^{-4} \cdot q_{c1Ncs} + 0.163 \quad (13a)$$

$$b = -1.000 \cdot 10^{-6} \cdot (N_1)_{60cs}^3 + 2.216 \cdot 10^{-4} \cdot (N_1)_{60cs}^2 + 1.727 \cdot 10^{-3} \cdot (N_1)_{60cs} + 0.1557 \quad (13b)$$

$$\beta = 0.01166 \cdot FC + 0.3536 \cdot (q_{c1Ncs} - \Delta q_{c1N})^{0.264} - 0.2805 \quad (14a)$$

$$\beta = 0.01166 \cdot FC + 0.1091 \cdot ((N_1)_{60cs} - \Delta(N_1)_{60})^{0.5} + 0.5058 \quad (14b)$$

The details of the procedure are reported in Appendix B. By so doing, simple charts of  $r_{u,ff}(FS_{liq,ff})$  can be drawn, as reported in Figure 3.5 for fine contents  $FC = 0, 10, 20$  and  $30\%$ . For  $FC \neq 0$  and a given value of  $D_r$ , minor differences exist in the curves if expressed in terms of  $q_{c1Ncs}$  or  $(N_1)_{60cs}$ , because of the different analytical relationships linking  $b$  to the normalized resistances (equations 13).

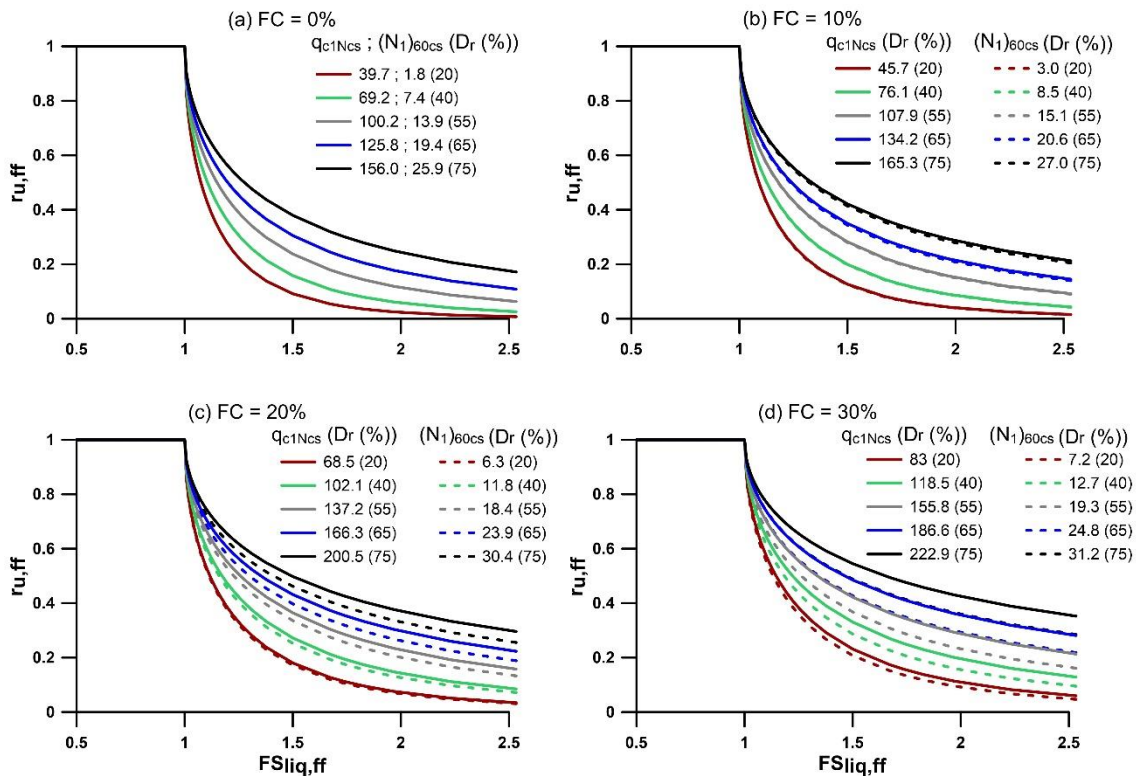


Figure 3.5 - Charts with the proposed relationship between the free field pore pressure ratio,  $r_{u,ff}$  and



This project has received funding from the European Union's Horizon 2020 research and innovation programme under grant agreement No. 700748

the free field liquefaction safety factor,  $FS_{liq,ff}$  for different fine contents: (a)  $FC=0\%$ , (b)  $FC=10\%$ , (c)  $FC=20\%$  and (d)  $FC=30\%$

Equation (12) is more comprehensive than equation (4), as it takes into account both the shape of the  $CRR(N)$  curve (via the parameter  $b$ ) and of the  $r_u(N)$  (via the parameter  $\beta$ ).

### 3.2 EXPERIMENTAL VERIFICATION OF THE SIMPLIFIED EXPRESSION OF $r_u(FS_{LIQ,FF})$

Equation 12 has been compared with the experimental results of published undrained cyclic triaxial tests carried out on six different granular soils, whose grading are reported in Figure 3.6

Ottawa F65 sand and Ticino sand are clean sands; Pieve di Cento and Sant'Agostino sands are materials with some fine. Messina sandy gravel was retrieved in Calabria (Italy), near the Sicily Strait. For all these soils,  $D_r$  of the tested specimens was given. This was not the case of Sendai sand, for which  $D_r$  was estimated from the SPT blow count ( $N_{SPT} = 12$ ) close to the retrieval depth (3 m, OYO Corporation, 2014), calculating  $N_{60}$  for an energy ratio of 75% (typical value for Japan, as assumed also by Ziotopoulou, 2010).

Figure 3.7 reports the cyclic resistance curves  $CRR(N)$  of the six soils (best fitting of the experimental data), used to calculate the safety factor from the laboratory tests ( $FS_{liq,ff}=CRR(N)/CSR$ ).

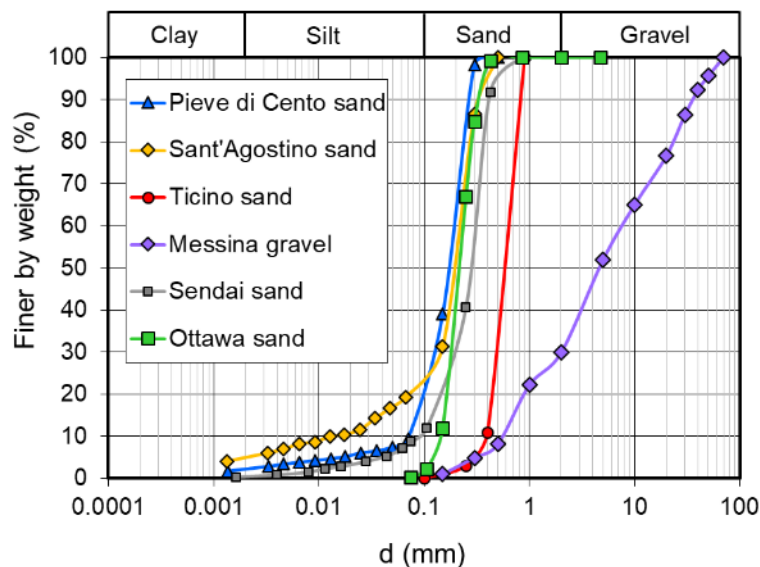


Figure 3.6 - Grain size distribution curves of the soils: Pieve di Cento sand (Mele et al., 2019), Sant'Agostino sand (Mele et al., 2018), Sendai sand (Regnier et al., 2018; OYO Corporation, 2014),



This project has received funding from the European Union's Horizon 2020 research and innovation programme under grant agreement No. 700748

*Ottawa sand (El Ghoraiby et al., 2017, Vasko, 2015), Ticino sand (Mele, 2019) and Messina gravel (Flora et al., 2012).*

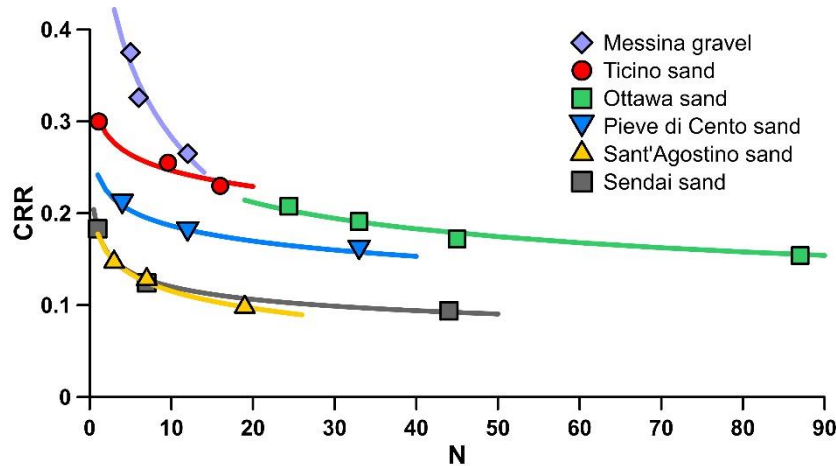


Figure 3.7 - Cyclic resistance curves from cyclic triaxial tests on the soils of Fig. (6): Messina gravel with  $D_r = 68\%$  (Flora et al., 2012), Ticino sand with  $D_r = 40\%$  (Mele, 2019), Ottawa sand with  $D_r = 62\%$  (El Ghoraiby et al., 2017; Vasko, 2015), Pieve di Cento sand with  $D_r = 48\%$  (Mele et al., 2019), Sant'Agostino sand  $D_r = 45\%$  (Mele et al., 2018), Sendai sand with estimated  $D_r = 69\%$  (OYO Corporation, 2014) investigated in cyclic triaxial tests

Figure 3.8 compares the experimental  $r_{u,ff}(FS_{liq,ff})$  trends for the different soils with the curves obtained for the FC and  $D_r$  of the pertinent tested soil (equation 12). Irrespective of soil grading and density, the agreement is good, being extremely good for  $FS_{liq,ff} < 1.5$  (i.e., for the range of values of  $FS_{liq,ff}$  of higher practical interest). For  $FS_{liq,ff} > 1.5$ , with the exception of the test on Messina gravel with the lowest value of CSR, the analytical prediction of  $r_{u,ff}$  is conservative, corresponding to values of  $r_{u,ff}$  slightly higher than the experimentally calculated ones.



This project has received funding from the European Union's Horizon 2020 research and innovation programme under grant agreement No. 700748

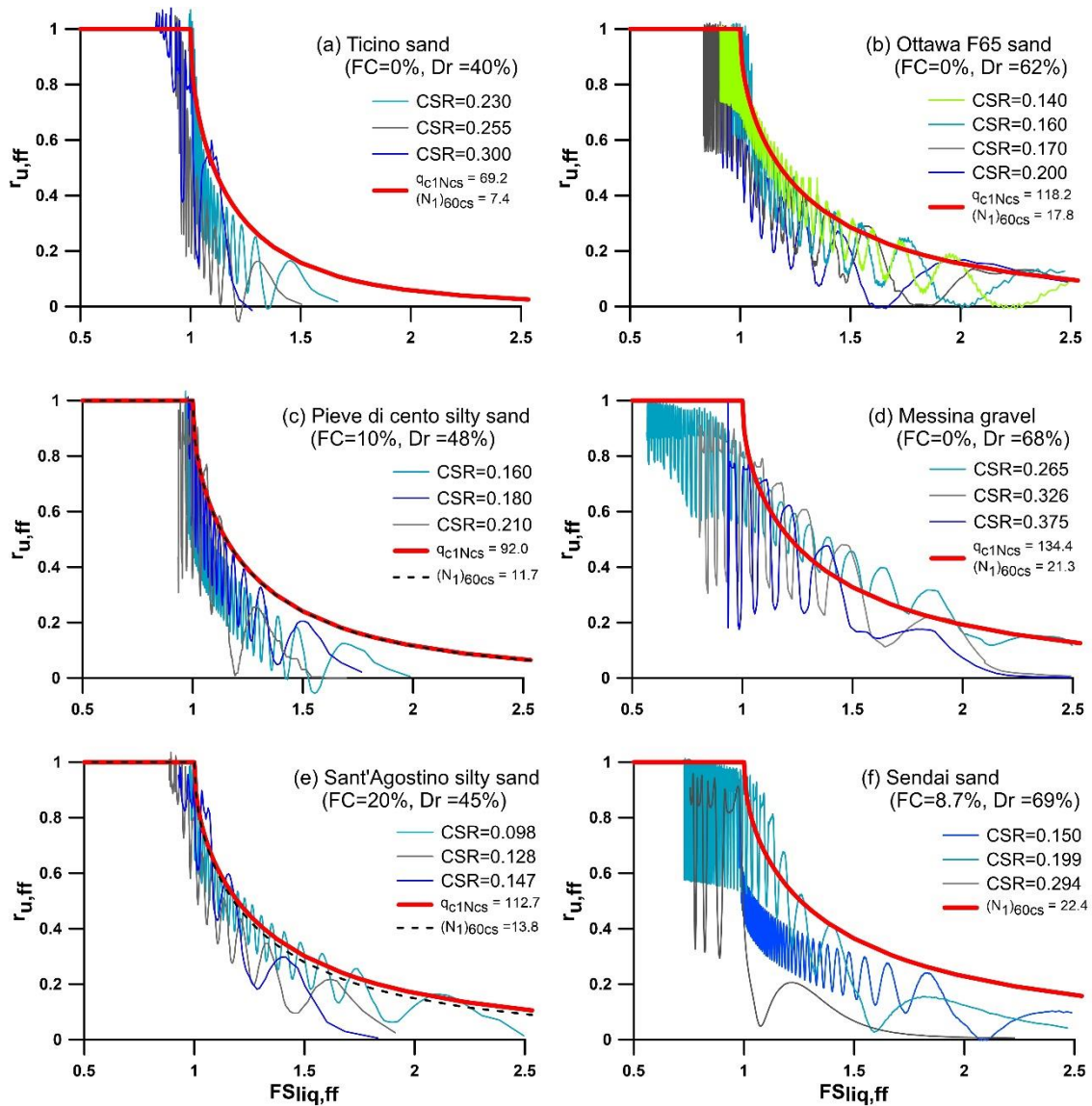


Figure 3.8 - Comparison between the proposed analytical curves and the experimental data from literature for (a) Ticino sand (Mele, 2019), (b) Ottawa sand (El Ghorraiby et al., 2017; Vasko, 2015), (c) Pieve di Cento sand (Mele et al., 2019), (d) Messina gravel (Flora et al., 2012), (e) Sant'Agostino sand (Mele et al., 2018) and (f) Sendai sand (OYO Corporation, 2014)



This project has received funding from the European Union's Horizon 2020 research and innovation programme under grant agreement No. 700748

## 4 DESIGN APPROACHES

The factor of safety can be increased (and the pore pressure increments decreased) by either increasing the soil capacity CRR, decreasing the demand CSR or by some combination of both such that the ratio has a net positive increase. Table 4.1 shows approaches for increasing soil capacity and decreasing demand (after Woeste et al., 2016).

Table 4.1 – Main approaches for increasing soil capacity and decrease demand (modified after Woeste et al., 2016)

Increase Capacity	Decrease Demand
C1) Increase soil density C2) Provide a mechanism for rapid dissipation of excess pore water pressure C3) Provide a mechanism to reduce excess pore water pressure	D1) Soil reinforcement/Shear stress redistribution

To determine the effect that ground improvement techniques will have on the FS it is useful to examine them in terms of how they either increase capacity or decrease demand.

The liquefaction potential of sandy soils is commonly evaluated using the “simplified” procedure (Whitman, 1971; Seed and Idriss, 1971). This procedure was developed semi-empirically and is based on field observations and laboratory data. The procedure quantifies the FS against liquefaction by defining the capacity of the soil as the cyclic resistance ratio (CRR) and the demand imposed as the cyclic stress ratio (CSR). The CRR can be estimated by the standard penetration test (SPT) corrected blow count ( $N_{1,60cs}$ ), or other in-situ indices. The CSR is proportional to the peak horizontal acceleration. Additionally, strong ground motion duration needs to be taken into account, which is correlated to earthquake magnitude. Towards this end, CSR is often presented in normalized form such that durational effects match those of a magnitude 7.5 event (i.e.,  $CSR_{M=7.5}$ ).



This project has received funding from the European Union's Horizon 2020 research and innovation programme under grant agreement No. 700748

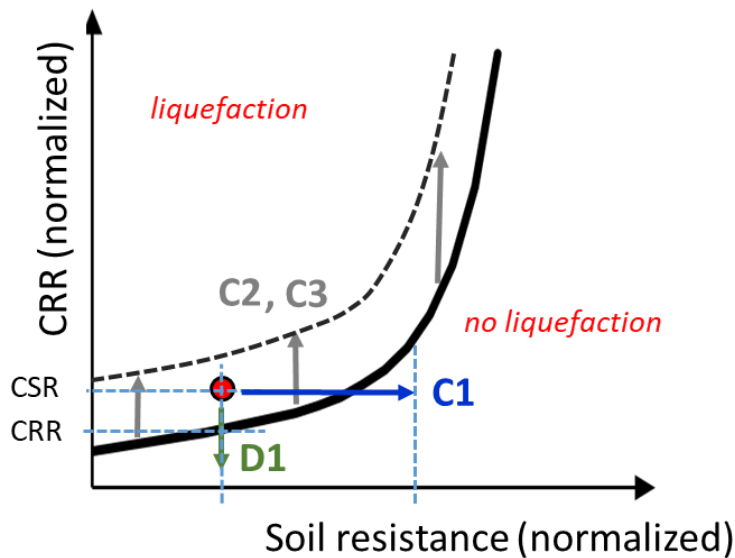


Figure 4.1 - Trend of how the physical processes affect the stress-based liquefaction curve (Modified after Green, 2001).

Figure 4.1 shows a plot of the simplified liquefaction evaluation procedure. For a more in-depth discussion on the simplified procedure refer to Youd et al. (2001) and Idriss and Boulanger (2008). As can be seen in this figure, if a site subjected to a given earthquake scenario plots above the CRR curve, then liquefaction is predicted to occur. Conversely, if a site subjected to an earthquake scenario plots below the CRR curve then liquefaction is not predicted to occur. It is useful to view the liquefaction mitigation mechanisms (Table 4.1) associated with soil improvement techniques (Table 2) in terms of the simplified liquefaction evaluation chart. As shown in Fig. 4.1, increasing soil density (C1) or increasing the lateral effective confining stress (C2) results in an increase in penetration resistance. For these scenarios the boundary between “liquefaction” and “no liquefaction” is assumed to be unaffected. In contrast, preventing contraction of the soil skeleton (C3) or enhancing a rapid dissipation of excess pore water pressure (C4) produces a shift of the boundary between the zones of “Liquefaction” and “No Liquefaction,” thereby effectively reducing the zone of “Liquefaction”. Finally, reduction of demand by shear stress redistribution (D1) results in a decrease of the  $CSR_{M=7.5}$  moving the point of interest down into the zone of “No Liquefaction” (Green, 2001).



This project has received funding from the European Union's Horizon 2020 research and innovation programme under grant agreement No. 700748

It is also interesting to analyze the pore pressure build up mechanism during the seismic action in the CRR:N plane, where N is the equivalent number of constant amplitude cycles that represent in a simplified way the duration of shaking for a given Magnitude. If  $FS_{ff,liq} < 1$  (i.e.  $CRR < CSR$ ) (Figure 4.2) the demand plots above the CRR curve, and some action has to be taken to have  $FS_{ff,liq} \geq FS_{min}$ , because otherwise liquefaction will take place ( $N_{liq} < N_{eq}$ ).

Two approaches are possible, as depicted in Figure 4.2.

- Approach a): increase CRR to CRR mod. As previously said, this action can be done for instance increasing soil density (C1), i.e. changing one of the soil state properties.
- Approach b): increase  $N_{liq}$  to  $N_{liq,mod}$ , reducing the tendency of the soil to accumulate pore pressure increments. In this case, soil resistance has not been changed (i.e. soil state is not affected by the action). An example is the use of drains that enhance a rapid dissipation of excess pore water pressure (C4). Drains are designed considering a limit value of the excess pore water pressure, while nothing is directly said on the increase of the safety factor. Obviously, with this second approach a further step needed to accommodate code's prescriptions is to find a correlation between  $\Delta u$  (or  $r_u$ ) and  $FS_{liq}$ . The approach suggested in the previous section may be of help to this aim.



This project has received funding from the European Union's Horizon 2020 research and innovation programme under grant agreement No. 700748

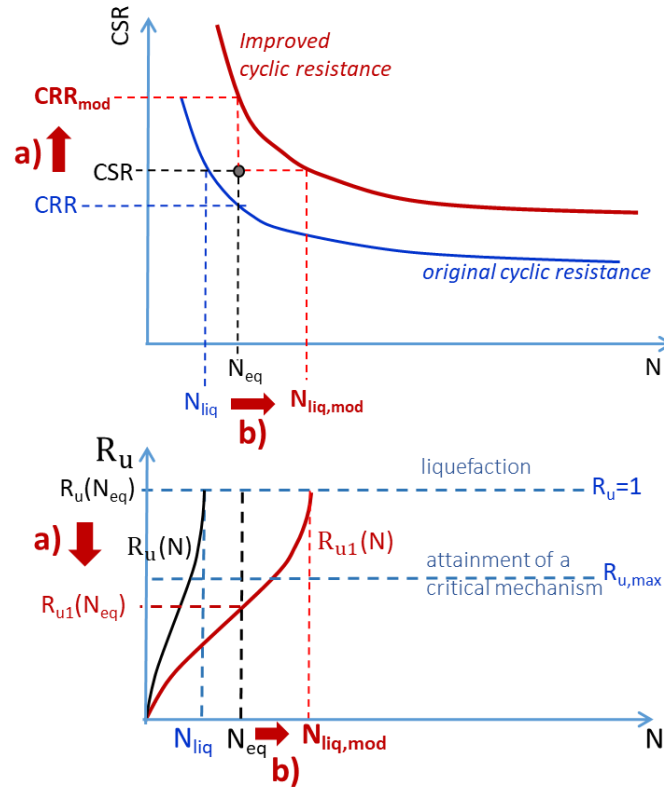


Figure 4.2 - Conceptual representation of two possible design approaches (a and b) to improve soil resistance to liquefaction.

The two approaches obviously lead to the same final result, i.e. the change of position of the CRR:N curve, which finally plots above the demand. Obviously, checking the effectiveness of ground improvement on site is much easier in the case of technologies that change CRR, as this can be indirectly controlled by quantifying the change in soil resistance via CPT or SPT. On the contrary, when using drains the possibility to check the performance of the technology is only theoretical.



This project has received funding from the European Union's Horizon 2020 research and innovation programme under grant agreement No. 700748

## 5 HORIZONTAL DRAINS

### 5.1 INTRODUCTION

Dynamic liquefaction is a phenomenon that may occur during earthquakes in loose and saturated sandy soil. It is induced by the pore water pressure build-up due to ground shaking that causes a significant reduction of soil shear strength and stiffness and potential damage to existing structures. Drainage as mitigation action is typically carried out by the insertion of vertical drains (often called for this application “earthquake drains”) and is one of the most efficient ways to protect existing structures (e.g. Harada et al., 2006). Furthermore, the installation of vertical drains is rather straightforward, being made with current tools like gravel columns, small steel cylindrical drains and simple tape drains. The insertion of drains into the liquefiable soil modifies the hydraulic boundary conditions. They can be considered as zero excess pore pressure surfaces that, if properly spaced, accelerate the consolidation process during seismic shaking, with a beneficial reduction of soil susceptibility to liquefaction. Some design methods based on the solution of radial consolidation are already available in literature to assign drains spacing (Seed and Booker, 1976; Bouckovalas et al., 2009). However, since the current technology considers only vertical drains, the application of this technique to mitigate liquefaction risk for existing buildings implies that they cannot be placed below the structures but around the buildings. In such a way, drainage is enhanced around the structure to protect, but not in the volume of soil underneath it, on which the structure is directly resting. Because of these geometrical constraints, the result is a reduced effectiveness of the technology in the built environment. A possible solution to this technological limitation may be obtained by adopting directional drilling (Allouche et al., 2000) to place horizontal or sub-horizontal drains directly underneath existing structures. This is a very promising evolution, whose use should not pose critical installation problems, at least as long as the horizontal drains are shallow (say not deeper than 10 m), and their diameter is not very large (say not more than 30 cm). Obviously, it is possible to deploy horizontal drains in multiple rows in either a square grid or in a staggered layout, as done for vertical drains. However, while (as previously mentioned) design methods already exist for the latter, for horizontal drains there is a lack of both experimental evidences on their effectiveness and of well-established design approaches. In fact, being the drains horizontal, the radial consolidation around each drain occurs in the vertical plane and may be influenced by the presence of a free-drainage ground horizontal surface or layer at a close distance. Furthermore, the hypothesis of an infinite number of drains implicitly assumed in the design of vertical drains is completely unrealistic for horizontal drains, for which only two or three lines of drains may be placed on site. In the following sections, the design approach proposed for an infinite number of vertical drains by Bouckovalas et al. (2009) will be extended to the case of a limited number of shallow horizontal drains.



This project has received funding from the European Union's Horizon 2020 research and innovation programme under grant agreement No. 700748

## 5.2 BACKGROUND ON DYNAMIC CONSOLIDATION

As mentioned above, soil liquefaction is induced in saturated, loose and shallow sandy soil by the build-up of pore water pressure due to cyclic loading in partially or totally undrained condition. When the excess pore pressure equates the initial effective normal stress, the shear strength of cohesionless soils goes to zero. Simultaneously, the shear modulus tends to zero, and considerable deformations can occur even before full liquefaction. Since the pore pressure increments due to seismic excitation are caused by the volumetric – distortional coupling of soil constitutive behaviour, advanced constitutive models should be used to simulate the complex coupled hydro-mechanical consolidation process. In common practice, however, this is never the adopted procedure, and simplifications are introduced to evaluate the seismically induced pore pressure increments. If the design goal is the limitation of pore pressure build-up to a desired, limit value, a simple uncoupled approach can be adopted to design a draining system. The consolidation process is then usually solved in the hypothesis of Terzaghi-Rendulic (Rendulic, 1936). In plane strain conditions, it reads:

$$\frac{k}{\gamma_w} \left( \frac{\partial^2 u}{\partial x^2} + \frac{\partial^2 u}{\partial y^2} \right) = m_v \frac{\partial u}{\partial t} \quad (15)$$

where  $x$  and  $y$  are the spatial coordinates in the plane,  $k$  is the hydraulic conductivity (assuming the soil homogeneous and the permeability isotropic),  $u$  is the excess pore pressure and  $m_v$  is the volumetric compressibility coefficient. As previously mentioned, in the case of ongoing cyclic loading, the quantification of  $u$  is a very complex problem, being it the resultant of concurrent dissipation (due to consolidation) and increment (due to cyclic shaking). A fundamental contribution to the solution was given by Seed et al. (1975), who proposed to write eq. (15) modifying its right-hand term as the algebraic sum of the change of pore pressure,  $du$ , taking place in the time interval,  $dt$ , because of the consolidation process, plus an accumulation term related to the ongoing seismic shaking. By so doing, eq. (15) becomes:

$$\frac{k}{\gamma_w} \left( \frac{\partial^2 u}{\partial x^2} + \frac{\partial^2 u}{\partial y^2} \right) = m_v \left( \frac{\partial u}{\partial t} - \frac{\partial u_g}{\partial N} \frac{\partial N}{\partial t} \right) \quad (16)$$

where  $u_g$  is the pore pressure increment generated during shaking and  $dN$  is the number of cycles taking place in the time interval  $dt$ . Within this framework, that is by far the most popular one adopted to study the dynamic consolidation of soils, different choices can be done to quantify the cyclic pore pressure build up ( $\partial u_g / \partial N$ ). Seed et al. (1975) proposed to this aim a function of the ratio  $N_{eq} / N_l$  between the seismic action, quantified through the number of equivalent cycles,  $N_{eq}$ , and the number of cycles required to cause liquefaction,  $N_l$ . Analysing the experimental results on shaking table by Harada et al. (2006), however, Bouckovalas et al. (2009) observed that the pore water pressure build-up at the early stages



This project has received funding from the European Union's Horizon 2020 research and innovation programme under grant agreement No. 700748

of cyclic loading depends mainly on soil fabric evolution and not on  $r_u$ . In order to cope with this experimental evidence, they proposed a different equation for  $\partial u_g / \partial N$ :

$$\frac{\partial u_g}{\partial N} = \frac{\sigma'_0}{\pi A N_l} \frac{1}{\left(\frac{t}{t_d} \frac{N_{eq}}{N_l}\right)^{1-\frac{1}{2A}} \cos\left(\frac{\pi}{2} r_u\right)} \quad (17)$$

where  $\sigma'_0$  is the initial vertical effective stress,  $A$  is an empirical parameter affecting the shape of the accumulation curve,  $t$  is the time variable,  $t_d$  is the significant duration of seismic shaking,  $r_u$  is the excess pore pressure ratio ( $u_g / \sigma'_0$ ).

In the hypothesis of a linear dependency of the number of cycles on time, it can be written that:

$$\frac{\partial N}{\partial t} = \frac{N_{eq}}{t_d} \quad (18)$$

Hence, by substituting (3) and (4) in (2), and using dimensionless variables, the following form of the equation of consolidation is obtained:

$$T_{ad} \left( \frac{\partial^2 r_u}{\partial \left(\frac{x}{d}\right)^2} + \frac{\partial^2 r_u}{\partial \left(\frac{y}{d}\right)^2} \right) = \frac{\partial r_u}{\partial \left(\frac{t}{t_d}\right)} - \frac{N_{eq}}{\pi A N_l} \frac{1}{\left(\frac{N_{eq}}{N_l} \frac{t}{t_d}\right)^{1-\frac{1}{2A}} \cos\left(\frac{\pi}{2} r_u\right)} \quad (19)$$

where  $d$  is the drain diameter and  $T_{ad}$  is a dimensionless time factor defined as:

$$T_{ad} = \frac{t_d k}{d^2 m_v \gamma_w} \quad (20)$$

in which  $\gamma_w$  is the specific weight of water.  $T_{ad}$  is a non-dimensional time, expressed as a function of a given drain diameter ( $d$ ) and of a specific site seismic hazard through the significant seismic duration ( $t_d$ ).



This project has received funding from the European Union's Horizon 2020 research and innovation programme under grant agreement No. 700748

### 5.3 NUMERICAL SOLUTION OF CONSOLIDATION FOR HORIZONTAL DRAINS

Eq. (5) has been used to solve the dynamic consolidation process considering the presence of horizontal drains, with the final goal to draw simple design charts to assign the spacing among them.

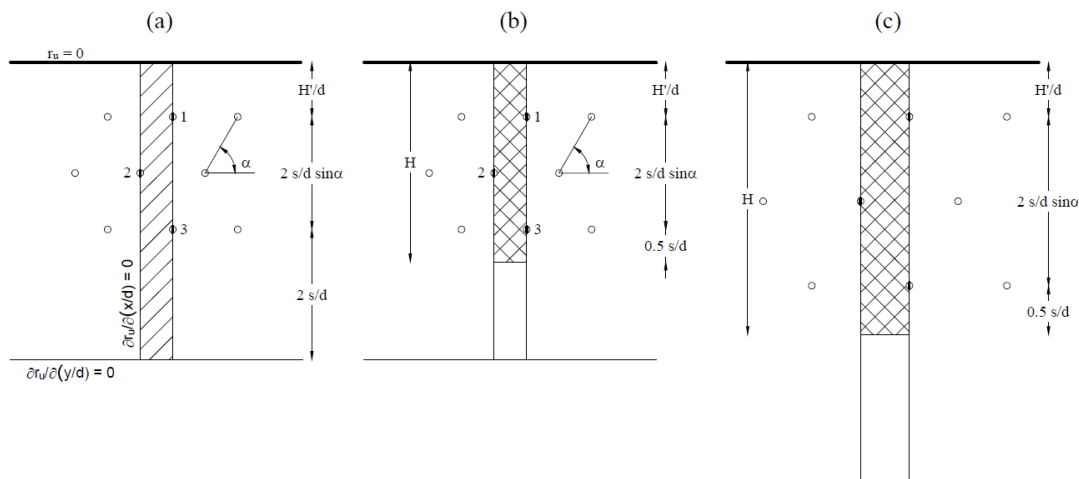


Figure 5.1 - geometrical layout: (a) numerical model domain; (b) numerical solution domain; (c) numerical solution domain with increased  $s/d$ .

The geometrical layout of the problem considered in this work is shown in Figure 5.1. The model is representative of a homogeneous layer of liquefiable soil in which three rows of drains (each one made of an infinite number of constantly spaced drains) are deployed in a staggered arrangement ('quincunces').  $H'$  is the distance from the upper boundary of the upper row of drains. As shown in the figure, the layout is defined by the spacing between the drains,  $s$ , and the angle  $\alpha$  (here assumed equal to  $60^\circ$ , as typical in this configuration). All the dimensions have been normalized to the diameter of the drains  $d$  (Figure 5.1a). The lower boundary, assumed impervious, is located at a depth of  $2s/d$  from the lower row of drains. Its position has been chosen far enough from the drains not to affect the solution. Taking advantage of symmetry, the analyses have been carried out with reference to a numerical domain of reduced area (Figure 5.1a). The left and right boundaries of such a domain are defined by two impervious planes of symmetry (Figure 5.1a). Along the impervious vertical sides of the model, the drains are modelled as segments with zero excess pore pressure. The upper boundary is represented by a surface with zero excess pore water pressure.

Even though the solution of the consolidation process is obtained in the whole numerical model domain, the effect of excess pore water pressure dissipation due to the drains is evaluated only in the part of it having thickness  $H$  from the upper boundary, being



This project has received funding from the European Union's Horizon 2020 research and innovation programme under grant agreement No. 700748

$H=(H'/d+2s/d \cdot \sin \alpha + 0.5 \cdot s/d)$  (Figure 5.1b). This assumption stems from the observation that, at a depth equal or higher than  $0.5 s/d$  below the lower drains ( $z>H$ ), the pore pressure increments are not affected by the presence of the drains, as shown in the following section. These assumptions imply that by changing the normalized spacing  $s/d$  among the drains the geometrical features of both the numerical model and the solution domains are modified (Figure 5.1c).

The problem was solved with an implicit finite difference method (Crank et al. 1947; D'Acunto, 2012) discretizing the domain with a rectangular grid. Spatial variables were related to drain diameter to simplify the design approach; as already pointed out, drain diameter is limited by technology, thus it is easy to assign, and, by consequence,  $H'/d$  can be determined. Each drain segment was discretized by six nodes. By solving the consolidation problem, it is possible to know the excess pore pressure ratio in each point of the model grid, at a dimensionless time  $t/t_d$ . The problem has been solved in a parametric way by varying the geometrical layout (spacing  $s/d$  and distance of the upper surface,  $H'/d$ ), the soil properties (i.e. the volumetric compressibility coefficient,  $m_v$ , and the coefficient of hydraulic conductivity,  $k$ ) and the parameters defining the seismic action ( $T_{ad}$ ,  $N_{eq}/N_I$ ).

### 5.3.1 Numerical results

Once the problem was solved, the average and maximum excess pore pressure ratios, respectively  $r_{u,mean}(t, y/d)$  and  $r_{u,max}(t, y/d)$ , were calculated for each depth to quantify the effect of drains. The vertical profiles of these quantities at the end of the analysis are presented in Figure 5.2, Figure 5.3, Figure 5.4 and Figure 5.5.



This project has received funding from the European Union's Horizon 2020 research and innovation programme under grant agreement No. 700748

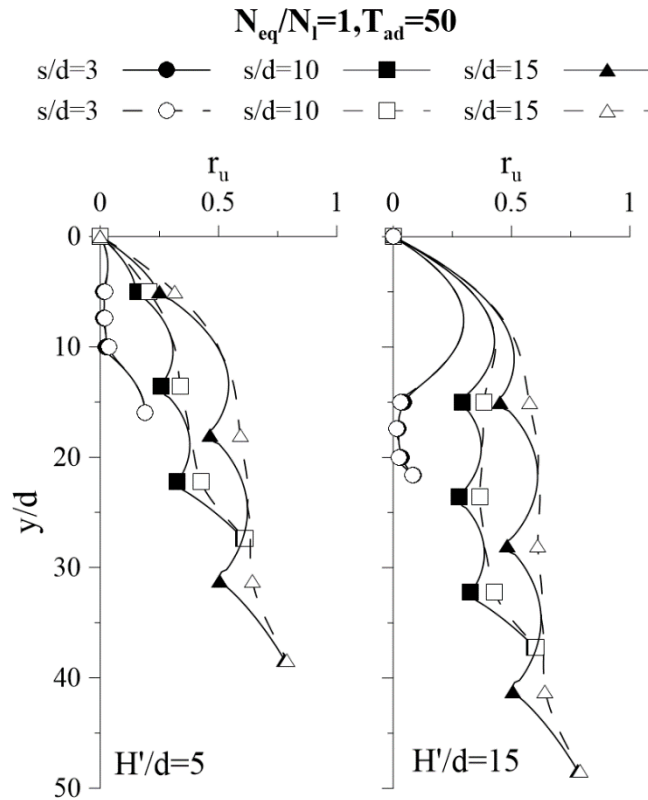


Figure 5.2 - Vertical profiles of  $r_u$  mean (continuous grey lines) and  $r_u$  max (dashed black lines) at the end of shaking, with  $T_{ad}=50$  and  $N_{eq}/N_l=1$ .

In Figure 5.2 the effect of drain spacing with  $T_{ad}=50$  and  $N_{eq}/N_l=1$ , is shown for two different values of  $H'/d$ . The mean and maximum profiles of  $r_u(y/d)$  at the end of shaking are similar, differing more around the depths of drains, with such a difference being a function of drains' spacing: obviously, for closer spacing the effectiveness of drains increases. It is worth noting that when  $s/d$  is much smaller than  $H'/d$ , the maximum value of  $r_u$  is attained in the upper part of the domain, where there is the largest drainage distance. When spacing increases and is higher than  $H'/d$ , the maximum value is attained in the lower part of the domain. It is evident that in the former case the contribution of drains to pore-pressure dissipation prevails on that of the upper draining surface; in the latter case, the opposite holds.



This project has received funding from the European Union's Horizon 2020 research and innovation programme under grant agreement No. 700748

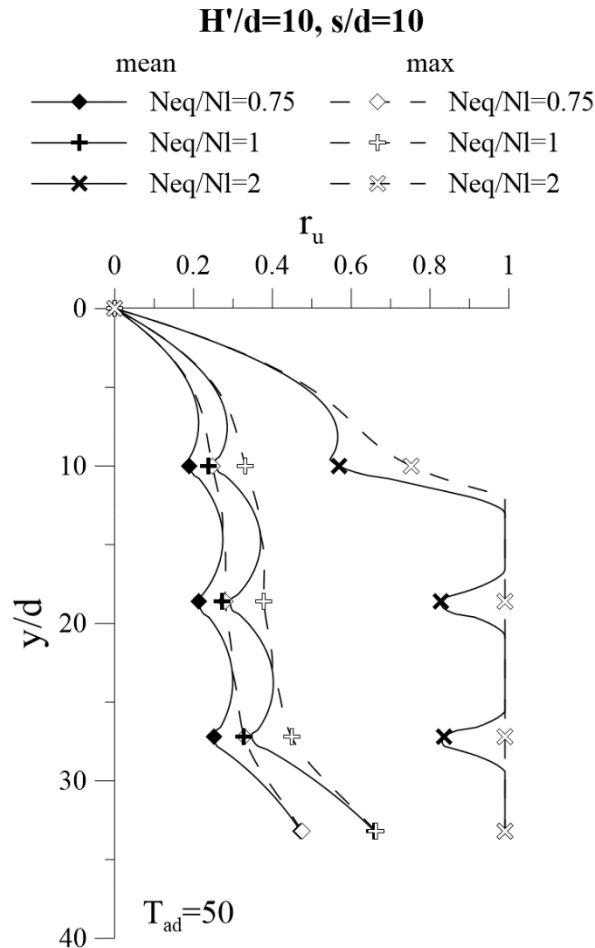


Figure 5.3 - Vertical profiles of  $r_u$  mean (continuous grey lines) and  $r_u$  max (dashed black lines) with  $H'/d=10$  and  $s/d=10$  at the end of shaking: effect of  $N_{eq}/N_l$  with  $T_{ad}=50$ .

In Figure 5.3 the vertical profiles of  $r_u$  with  $T_{ad}=50$ ,  $s/d=10$ ,  $H'/d=10$  and different values of  $N_{eq}/N_l$  are plotted. There is a slight difference between  $N_{eq}/N_l=0.75$  and  $N_{eq}/N_l=1$  and in both cases the excess pore pressure ratio is below 0.6 along the whole vertical. However, when  $N_{eq}/N_l=2$ , the excess pore pressure ratio is equal to 1 everywhere except for the area above the upper row of drains and around the drains themselves. It must be noted that a value of  $N_{eq}/N_l$  lower than 1 implies that during the shaking no liquefaction occurs ( $r_u$  is lower than 1), either with or without drains. Although in these cases liquefaction does not occur, the excess pore pressure build-up reduces both shear stiffness and strength of the soil. This induces non-negligible settlements and deformations under existing structures. Therefore, drains are useful also for  $N_{eq}/N_l \leq 1$ , to reduce pore pressure build-up (or  $r_u$ ) during shaking.



This project has received funding from the European Union's Horizon 2020 research and innovation programme under grant agreement No. 700748

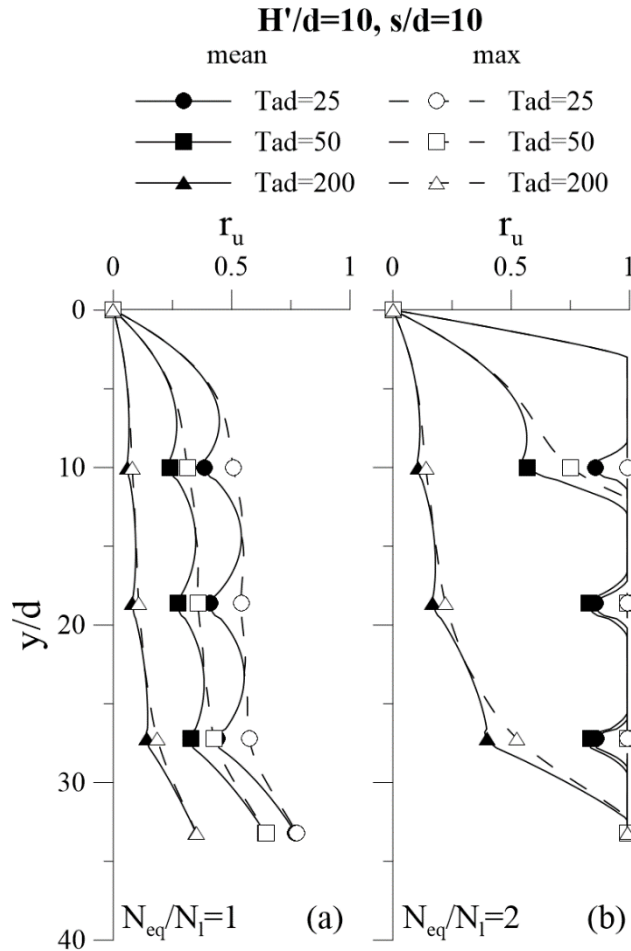


Figure 5.4 - Vertical profiles of  $r_u$  mean (continuous grey lines) and  $r_u$  max (dashed black lines) with  $H'/d=10$  and  $s/d=10$  at the end of shaking: effect of  $T_{ad}$  for  $N_{eq}/N_l=1$  and 2.

In Figure 5.4a and Figure 5.4b the effect of  $T_{ad}$  is shown. When  $N_{eq}/N_l$  is equal to 1, thanks to the drains, liquefaction is impeded even if  $T_{ad}$  is as low as 25 and their effect is enhanced significantly when  $T_{ad}$  increases. When  $N_{eq}/N_l=2$ , however, the effect of  $T_{ad}$  is much more significant. As a matter of fact, with  $s/d=10$  and  $H'/d=10$ , drains are not able to prevent liquefaction when  $T_{ad}$  is low and a smaller spacing is needed.



This project has received funding from the European Union's Horizon 2020 research and innovation programme under grant agreement No. 700748

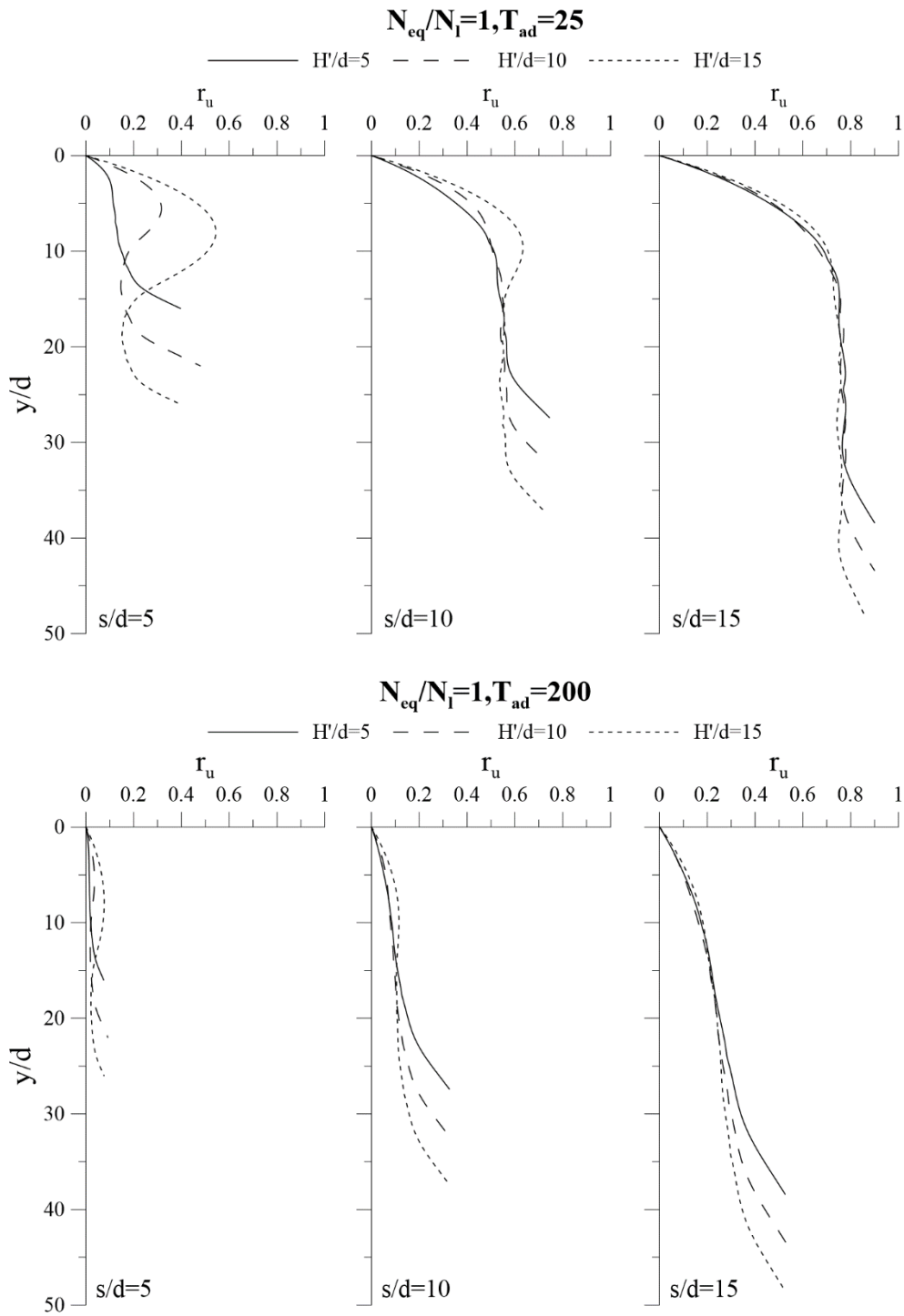


Figure 5.5 - Vertical profiles of  $r_{u,max}$  at the end of shaking with  $N_{eq}/N_1=1$  and  $T_{ad}$ .



This project has received funding from the European Union's Horizon 2020 research and innovation programme under grant agreement No. 700748

Figure 5.5 shows the effect of  $H'/d$  with different choices for spacing and two different values of  $T_{ad}$ . When  $H'/d$  is lower than  $s/d$ , the same maximum excess pore pressure ratios in the upper part of the domain are calculated, regardless of  $T_{ad}$ . This is due to the loss in efficiency of the drains when they are too close to the upper boundary. When increasing  $H'/d$ , the efficiency of drains on the upper part of the domain rises up while the effect of the upper boundary surface decreases. The combination of both effects gives a similar profile of  $r_u$  above the first row of the drains at varying  $H'/d$  ( $< s/d$ ). When  $H'/d$  exceeds the value of  $s/d$ , the negative effect of the increased distance between the upper boundary and the first row of drains exceeds the positive combined effect of the two boundaries and a higher excess pore pressure ratio is calculated.

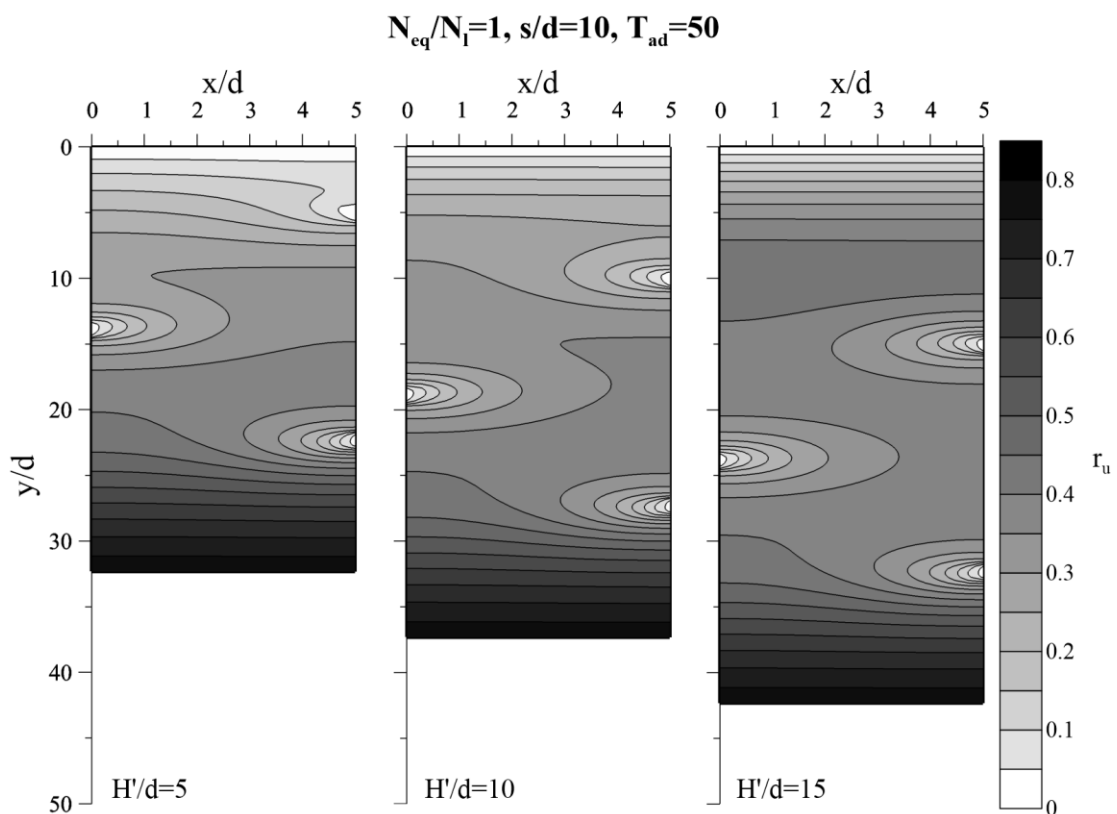


Figure 5.6 - Contours of excess pore pressure ratio in the solution domain at the end of shaking, with  $N_{eq}/N_I=1, s/d=10, T_{ad}=50$ .

The contours of excess pore pressure ratio shown in Figure 5.6 confirm these results. It can be seen a high gradient of  $r_u$  around drains that is independent of  $H'/d$  for the two deeper rows. The effect of the first row of drains is instead dependent of the distance from the upper



This project has received funding from the European Union's Horizon 2020 research and innovation programme under grant agreement No. 700748

boundary. When  $H'/d$  is lower than  $s/d$ , the effect of the upper boundary is predominant on the effect of the drain, lowering its efficiency. When  $H'/d$  is equal to  $s/d$ , there is almost no overlap between the upper boundary and the first row of drains and its efficiency is enhanced. Finally, if  $H'/d$  is higher than  $s/d$ , the drains act almost as a boundary condition with a lower excess pore pressure ratio on the upper part of the domain at a distance from the first row almost equal to half of the spacing. Indeed, in the last case, three areas can be distinguished: an upper part, where the gradients of excess pore pressure ratio are almost vertical, and the behaviour is almost one-dimensional; a middle part, between drains, where  $r_u$  is almost constant except for the area surrounding the drains, where the gradients are much higher; the lower part, where the effect of drains vanishes and again the gradients become vertical. When  $H'/d$  is lower or equal to  $s/d$ , the first two areas are partially overlapped. The contours also show that the difference between the vertical profiles of  $r_{u, mean}$  and  $r_{u, max}$  is negligible in the domain except for the depths corresponding to the rows of drains, as already pointed out.

### 5.3.2 Validation of results against FE analyses

The results obtained with the numerical model adopted in this study were validated using the results of a centrifuge test carried out at ISMGEO (Italy) and presented in deliverable D4.2 (Airoldi et al., 2018). In order to perform the validation accounting for the unavoidable differences between the experimental set up and the geometrical layout considered in this work (Figure 5.1), FEM numerical analyses had to be carried out. Plaxis 2D was used to this aim, and the coupled hydro-mechanical analysis were performed by using UBC3D-PML model (Petalas, 2012). This elastoplastic constitutive model is based on the UBCSand model (Puebla et al., 1997) and simulates the effects of cyclic loading using two yield surfaces of the Mohr-Coulomb type, one linked to isotropic hardening and the other to kinematic hardening. The calibration of model parameters has been performed following the indications of Beaty and Byrne (2011), i.e. expressing the parameters as functions of soil relative density. A wider description of the numerical simulations carried out within the project is reported in deliverable D4.4 (Flora et al., 2018).

The first step of the validation procedure was to simulate with Plaxis2D the seismic centrifuge test with horizontal drains (Airoldi et al. 2018) whose geometrical configuration is reported in Figure 5.7. In the centrifuge, drains were realized by perforated PVC pipes with an external diameter of 6 mm (0.3 m at prototype scale at 50g acceleration) and a thickness of 1 mm. In the numerical analyses, they were modelled as having a finite permeability (while the solution proposed in this paper assumes for the drains, as usual, an infinite permeability), whose value was calibrated on a back analysis of the centrifuge test. In the Plaxis model, tied degree of freedom conditions were used for the lateral boundaries, to simulate the true centrifuge boundary conditions.

The calibration of the model leads to the set of parameters reported in Table 5.1.



This project has received funding from the European Union's Horizon 2020 research and innovation programme under grant agreement No. 700748

LIQUEFACT  
Deliverable D4.5  
Liquefaction mitigation techniques guidelines  
v. 3.0



This project has received funding from the European Union's Horizon 2020 research and innovation programme under grant agreement No. 700748

*Table 5.1 - Centrifuge test calibration parameters.*

RD	$N_{1,60}$	e	n	v	$K_B^e$	$K_G^e$	$K_G^p$	$m_e$	$n_e$	$n_p$	$\phi_{cs}$	$\phi_{peak}$	Rf	$f_{dens}$	$f_{E,post}$
(%)	(-)	(-)	(-)	(-)	(-)	(-)	(-)	(-)	(-)	(-)	(°)	(°)	(-)	(-)	(-)
54.5	13.7	0.7	0.4	0.	2246.0	1036.0	680.6	0.5	0.5	0.4	33.0	34.4	0.7	9.0	1.00
0	0	3	2	3	0	0	0	0	0	0	0	0	4	0	

- Accelerometer
- Pore pressure transducer

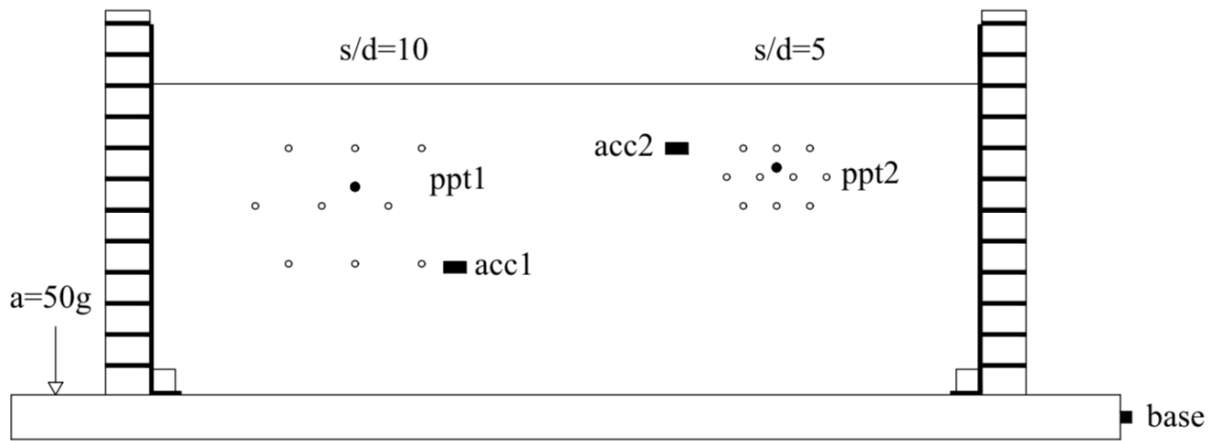


*Figure 5.7 - Geometry of centrifuge test model (modified after Airoidi et al., 2018).*

A standard Italian sand is used for the tests, namely Ticino sand, characterized by a coefficient of permeability  $k=2 \cdot 10^{-3} \text{ m/s}$ . The seismic input applied at the base of the model has the characteristics reported in Table 5.2 and Table 5.3. For further details on the experimental set up and results, the reader is addressed to Deliverable D4.2, for details on the numerical mesh and analysis to Deliverable D4.4.

*Table 5.2 - Earthquake characteristics;  $T_r$  is the return period,  $M_w$  is the moment magnitude,  $R_{ep}$  is the epicentral distance,  $t_d$  is the significant duration,  $a_{max}$  refers to maximum acceleration at the bottom of centrifuge model.*

Source file	$T_r$	$M_w$	$R_{ep}$	$t_d$	$a_{max}$
(-)	(years)	(-)	(km)	(s)	(g)
ESM EU.HRZ..HNE.D.19790415.061941.C.ACC.ASC	2475	6.9	62.9	18.67	0.18



This project has received funding from the European Union's Horizon 2020 research and innovation programme under grant agreement No. 700748

Table 5.3 - Parameters for numerical model (\*)

s/d	a <sub>max</sub>	z	r <sub>d</sub>	CSR	N <sub>I</sub>	N <sub>eq</sub> /N <sub>I</sub>	k	m <sub>v</sub>	T <sub>ad</sub>
(-)	(g)	(m)	(-)	(-)	(-)	(-)	(m/s)	(1/MPa)	(-)
5	0.159	2.3	0.98	0.214	1.2	14	1.7E-03	0.05	689
10		4	0.96	0.209	1.6	11			

(\*) r<sub>d</sub> is the shear stress reduction factor that accounts for dynamic response of the soil profile (Idriss, 1999), CSR is the cyclic stress ratio at depth z; a<sub>max</sub> refers to the acceleration at the top of centrifuge model, k, and m<sub>v</sub> are permeability and volumetric compressibility coefficient of soil

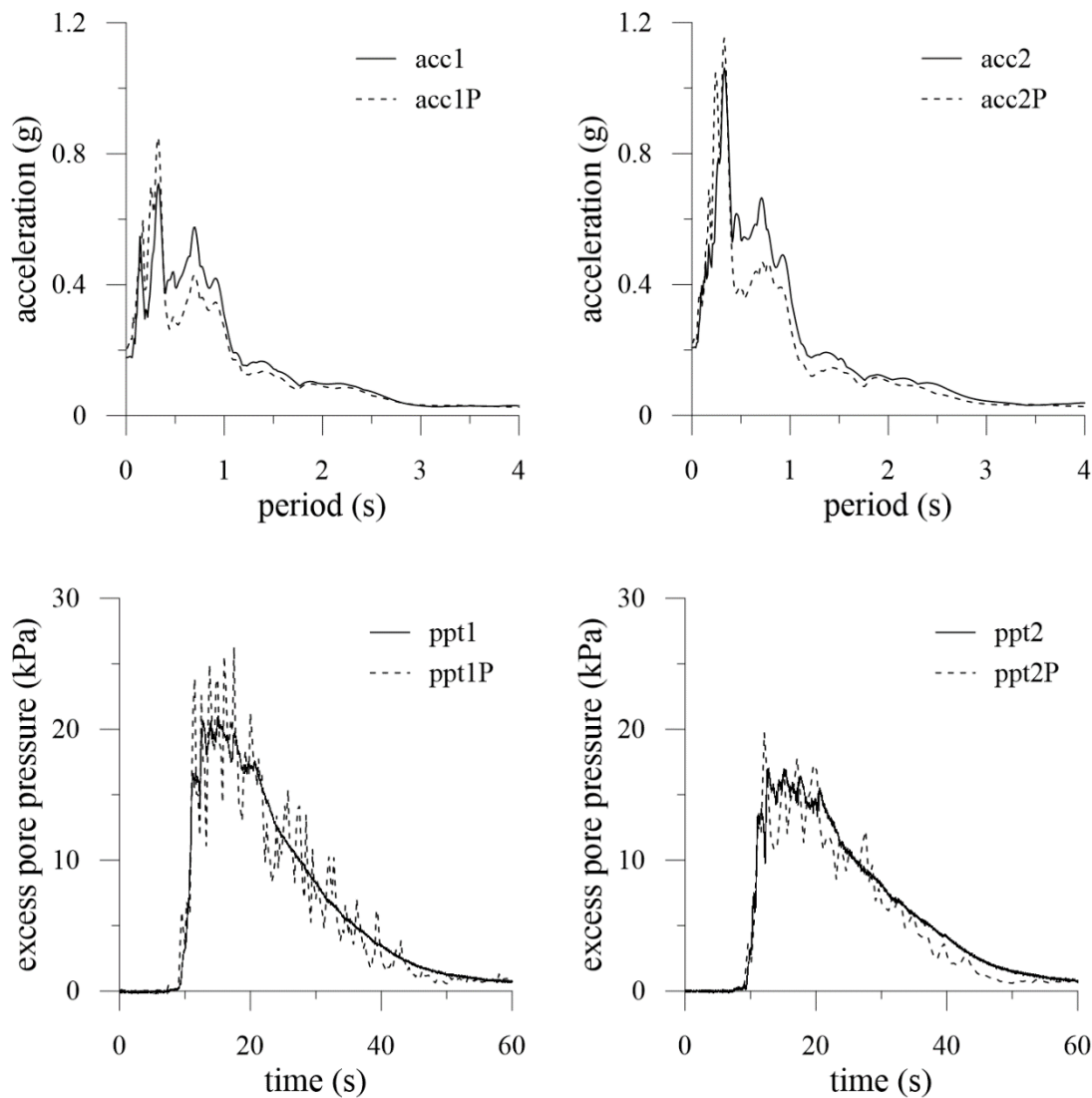


Figure 5.8 - Comparison between test measurements and FEM model results: acceleration spectra;



This project has received funding from the European Union's Horizon 2020 research and innovation programme under grant agreement No. 700748

*excess pore pressure history.*

A good agreement was found with the centrifuge test both in terms of excess pore pressure and acceleration, as shown in Figure 5.8 for both the values of spacing between drains adopted in the centrifuge test.

In order to carry out the validation of the numerical model proposed in this paper, a further step had to be done: once the FEM analyses were proven to be reliable and well calibrated, a further Plaxis2D analysis with the same coupled model was carried out by modelling drains by a zero excess pore pressure surface. In so doing, the results of FEM analyses can be compared to those obtained with the approach proposed in this paper, for which the drains are modelled as surfaces with infinite permeability (being characterized by zero excess pressure). In this comparison, the FEM analyses will be assumed as the “true” results.

In order to carry out the comparison, the volumetric compressibility coefficient ( $m_v$ ) required to determine  $T_{ad}$ , was derived from an isotropic compression curve at an isotropic compressive stress equal to 50 kPa; the number of equivalent cycles,  $N_{eq}$  was calculated based on the procedure suggested by Biondi et al. (2012). The number of cycles required to cause liquefaction was derived by the cyclic resistance curve; the Cyclic Stress Ratio (CSR) was calculated based on the approach proposed by Seed et al. (1975) with the maximum acceleration at ground surface derived by a dynamic total stress analysis. CSR is a function of the depth and by consequence, also  $N_l$  is a function of  $z$ ; thus, a representative depth has to be assumed to assign  $N_{eq}/N_l$ . In a design procedure, the depth would be set at the middle of the layer that has to be treated. Hence, the depth was set at the middle of numerical solution domain (Figure 5.1b), that is equal to 2.3 m and 4 m for  $s/d = 5$  and  $s/d = 10$ , respectively. The upper boundary with zero excess pore pressure is represented by the water table, thus  $H'/d$  (dimensionless distance between upper boundary and first row of drains) is equal to 4.33.

Figure 5.9 shows excess pore pressure ratio vertical profiles related to three vertical sections. The curves are very similar and show an almost constant distribution of excess pore pressure ratio on the horizontal direction. The profiles are reported for two instants, related to the time at which maximum excess pore pressure ratio was observed in Plaxis analysis, and at the end of earthquake significant duration. The dashed lines represent the bottom of the solution domain that is used to produce the design charts. A very good agreement can be observed on  $s/d=5$  at both times along all the vertical profile. The vertical profiles at  $s/d=10$  are quite similar from the top surface to the central row of drains, but numerical analysis overestimates significantly excess pore pressure ratio in the lower part of the domain, that is deeper compared to the case  $s/d=5$ ; this is due to the assumption that CSR is constant with depth, while it should decrease with depth. Thus, the proposed numerical approach overestimates the pore pressure build up in depth compared to the reference FE dynamic analysis. Furthermore, once excess pore pressure ratio achieves unity, the build-up of pore water pressure,  $\partial u_g/\partial t$ , given by eq. (3) is much higher than the dissipation due to drains,  $\partial u/\partial t$ , and



This project has received funding from the European Union's Horizon 2020 research and innovation programme under grant agreement No. 700748

thus the reduction of  $r_u$  calculated in the coupled dynamic analysis performed in Plaxis is not well captured in the numerical analysis.

However, the simplification considered in the proposed method leads to a conservative design approach, and the procedure can be thus considered validated.

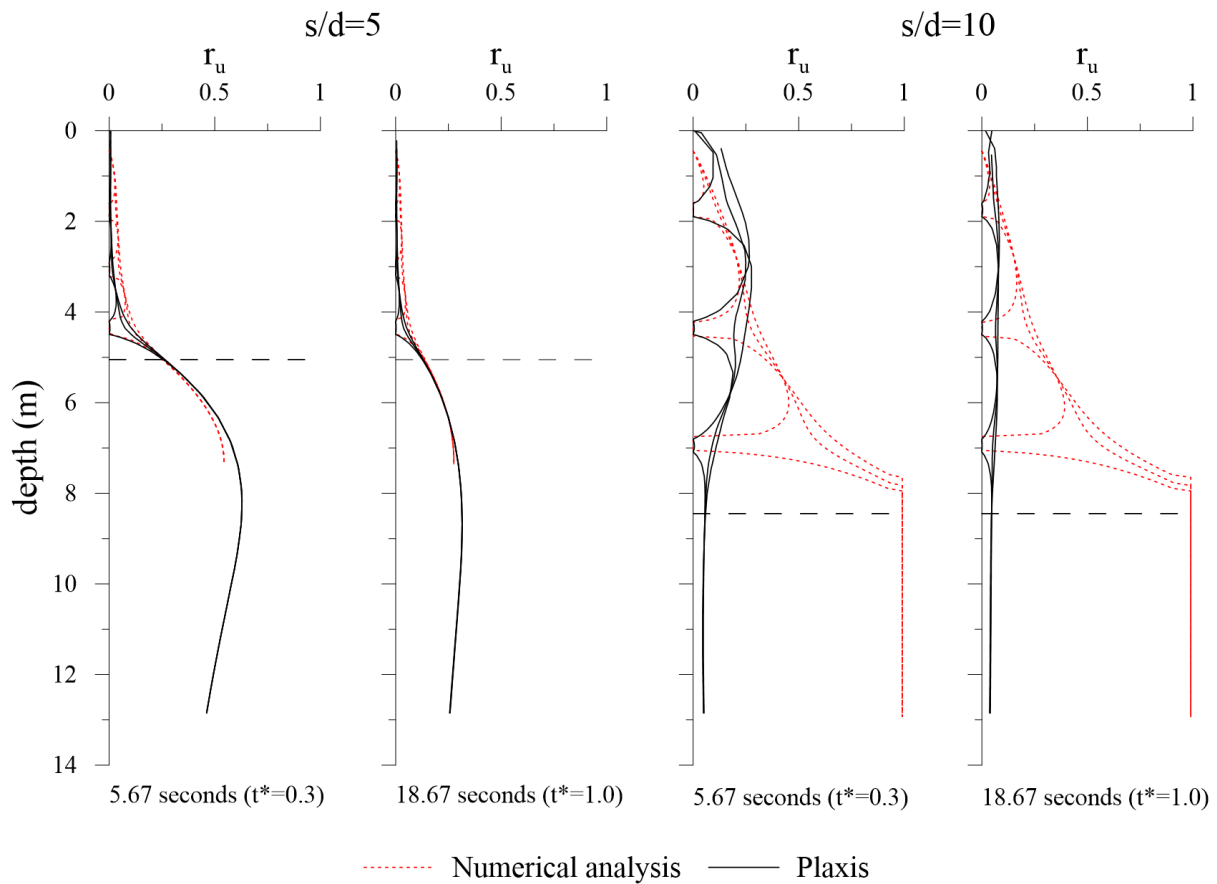


Figure 5.9 - Vertical profiles of excess pore pressure ratio for  $s/d$  equal to 5 and 10 at two times ( $t^*=t/t_d$ ). Continuous and dashed lines refer to Plaxis and numerical analyses, respectively.



This project has received funding from the European Union's Horizon 2020 research and innovation programme under grant agreement No. 700748

### 5.3.3 Charts of excess pore pressure ratio with upper pervious surface.

The results of the previously commented analyses were summarized in charts, as shown in Figure 5.10, Figure 5.11 and Figure 5.12.

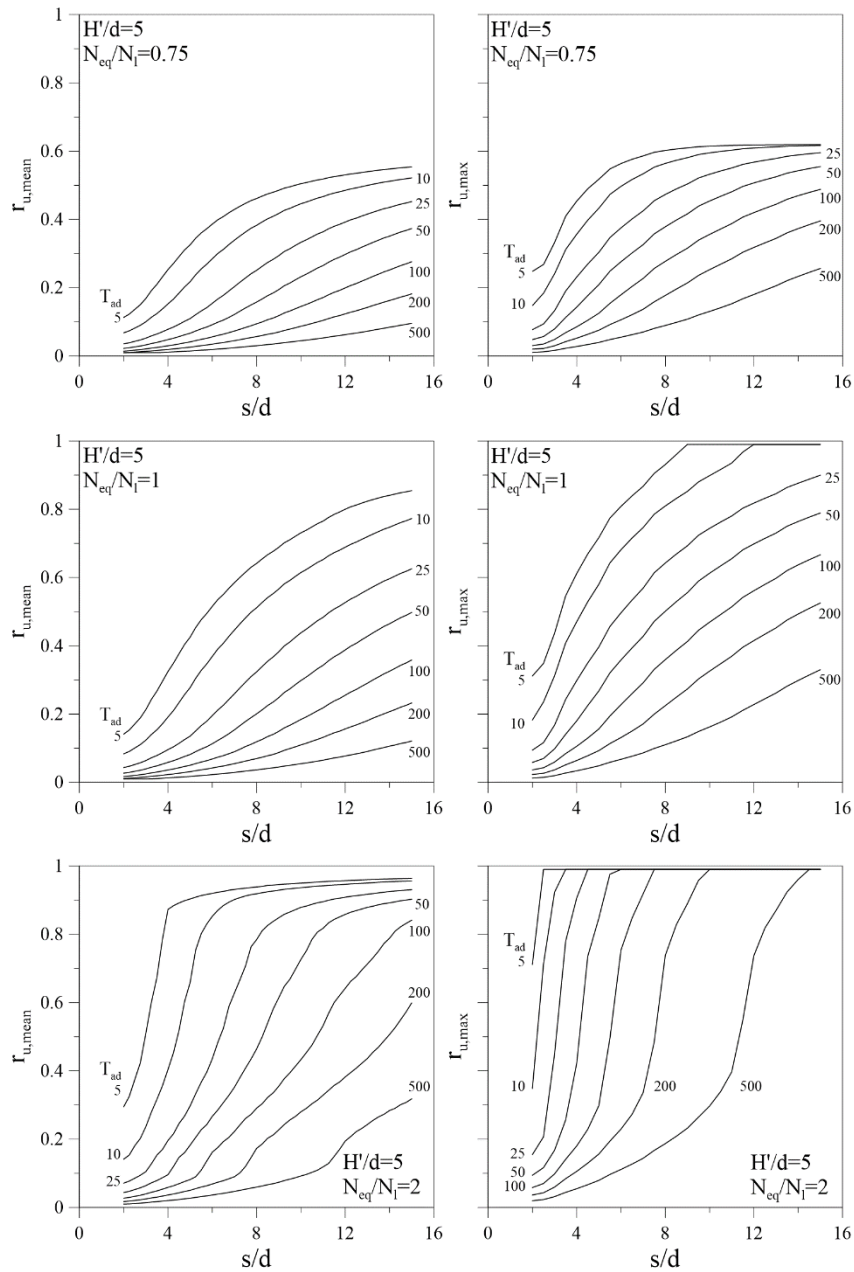


Figure 5.10 -  $r_u$  charts for  $H'/d=5$ . (Fasano et al, 2019).



This project has received funding from the European Union's Horizon 2020 research and innovation programme under grant agreement No. 700748

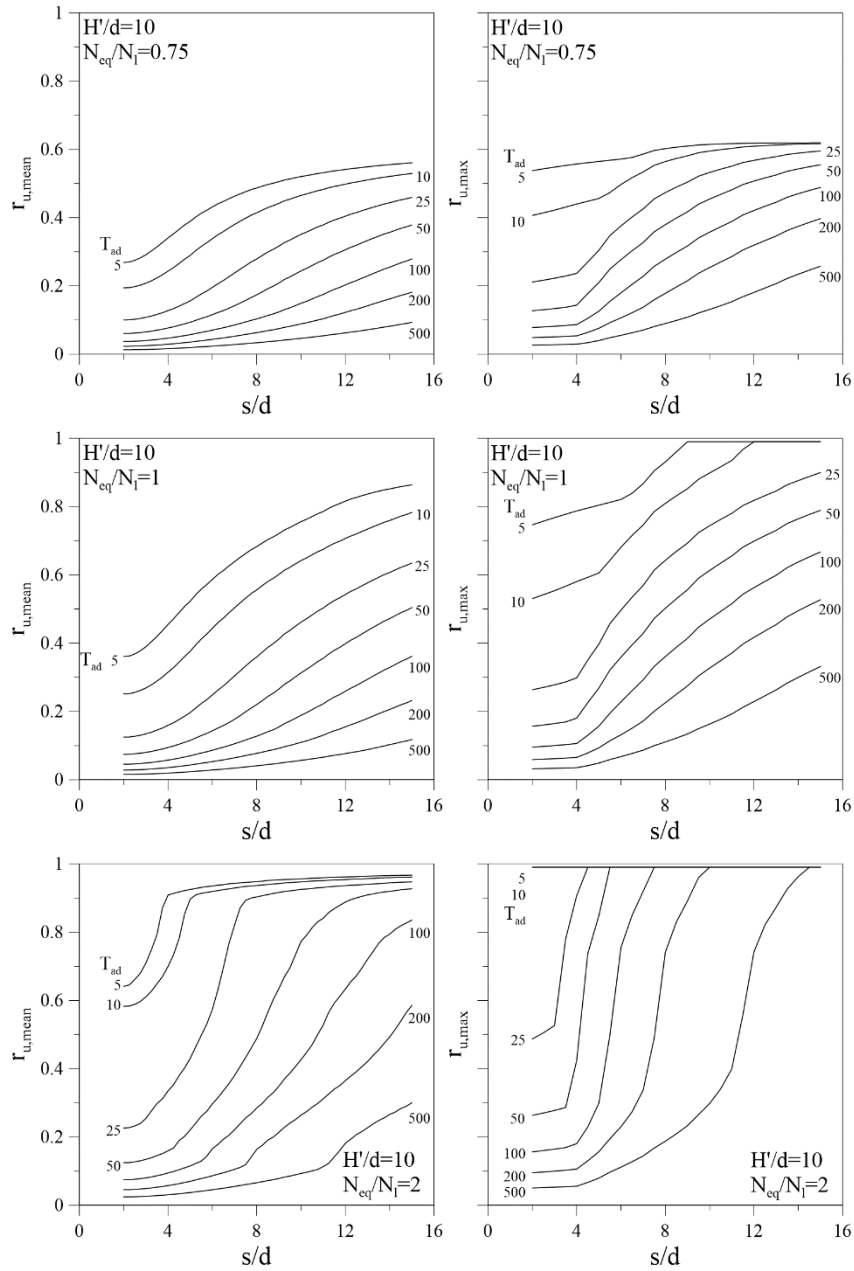


Figure 5.11 -  $r_u$  charts for  $H'/d=10$ . (Fasano et al, 2019).



This project has received funding from the European Union's Horizon 2020 research and innovation programme under grant agreement No. 700748

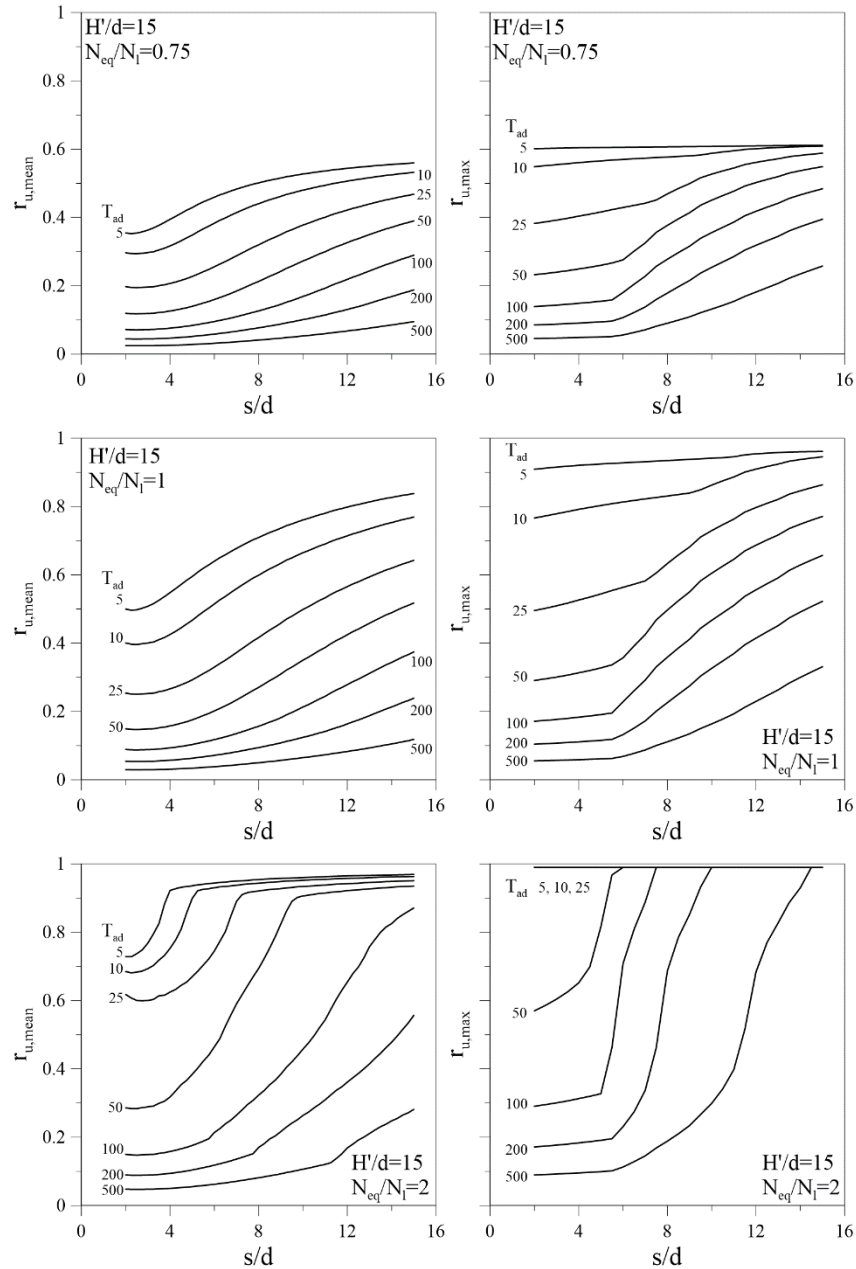


Figure 5.12 -  $r_u$  charts for  $H'/d=15$ . (Fasano et al, 2019).

The charts represent the excess pore pressure ratio,  $r_u$ , in the solution domain for different sets of parameters. For each instant  $t$ , the mean and maximum excess pore pressure ratios in the solution domain were evaluated. Because of the seepage induced by the hydraulic gradients around drains, the worst conditions are not necessarily attained at the end of the



This project has received funding from the European Union's Horizon 2020 research and innovation programme under grant agreement No. 700748

shaking, being possible to observe them during the shaking. Therefore, the maximum values in time of the mean and maximum excess pore pressure ratios calculated over the whole domain,  $r_{u,mean}$  and  $r_{u,max}$ , were considered in the design charts. Each one of them is related to specific values of the ratios  $H'/d$  and  $N_{eq}/N_i$ ; each curve refers to a value of  $T_{ad}$  and represents the excess pore pressure ratio (as explained before) for different values of  $s/d$ .

### 5.3.4 Charts of excess pore pressure ratio with upper impervious surface.

For the horizontal drains system considered before the upper boundary was represented by a pervious surface, this condition allows the vertical drainage through this surface with a consequent reduction of the excess pore water pressure. In common practice it is possible the presence of a low permeability soil upon the liquefiable one. In this case the drainage through the upper surface is not possible and a larger excess pore water pressure is achieved. As for the domain in Figure 5.1, a numerical solution for the domain with an upper impervious surface was done for the domain shown in Figure 2.1Figure 5.13.

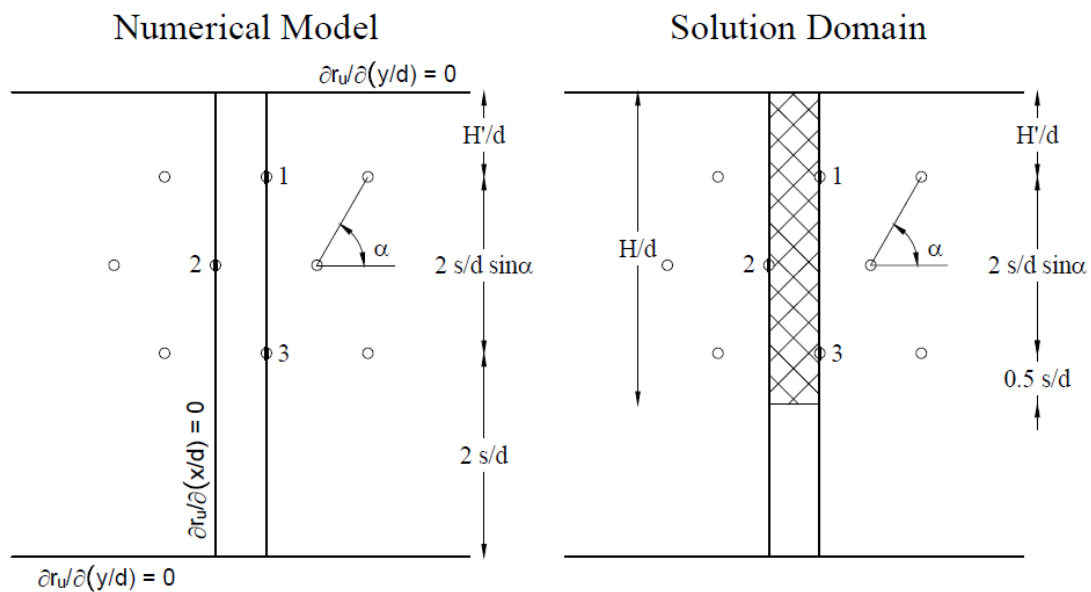


Figure 5.13 – numerical model and solution domain for impervious upper surface.

As for the domain with pervious upper surface, the numerical results have been summarized in some design charts.



This project has received funding from the European Union's Horizon 2020 research and innovation programme under grant agreement No. 700748

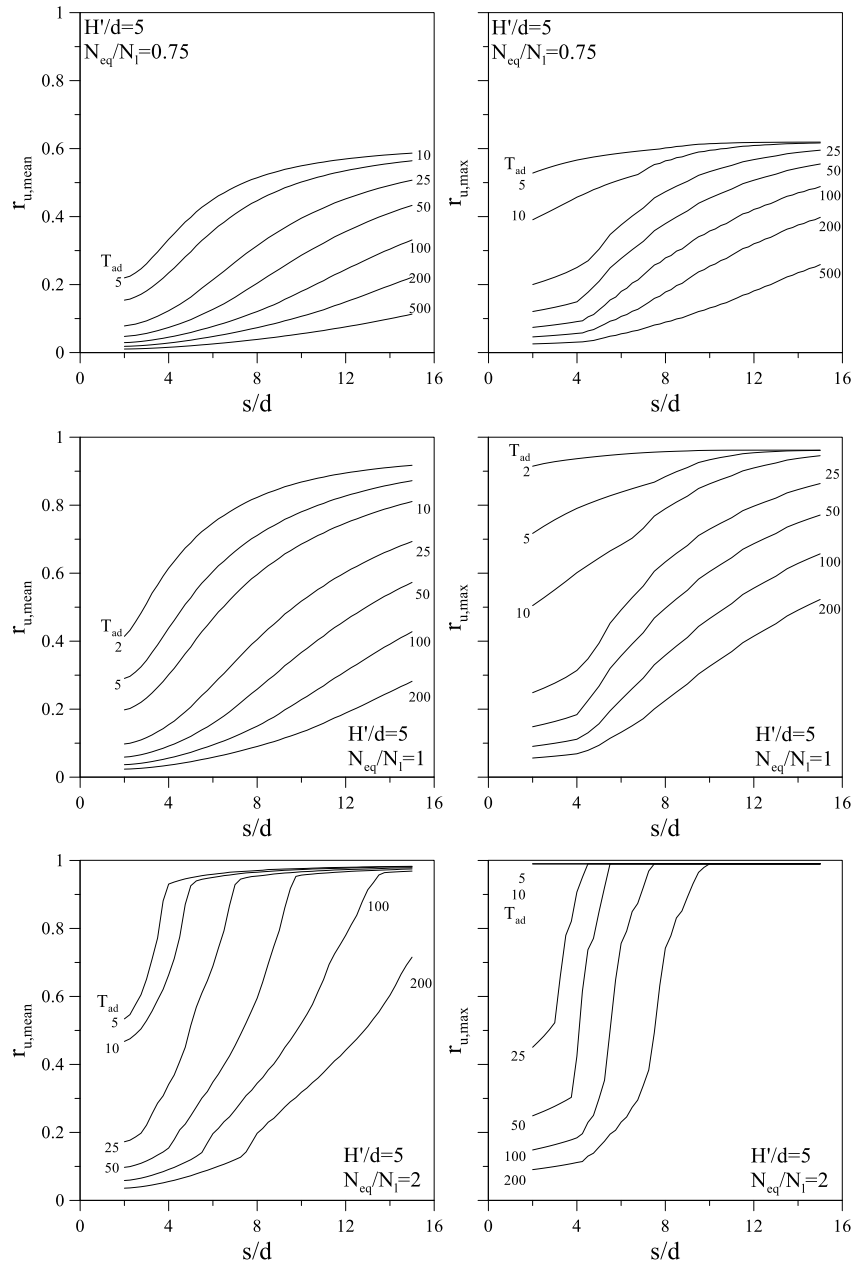


Figure 5.14 -  $r_u$  charts for  $H'/d=5$ . (De Sarno et al, 2019).



This project has received funding from the European Union's Horizon 2020 research and innovation programme under grant agreement No. 700748

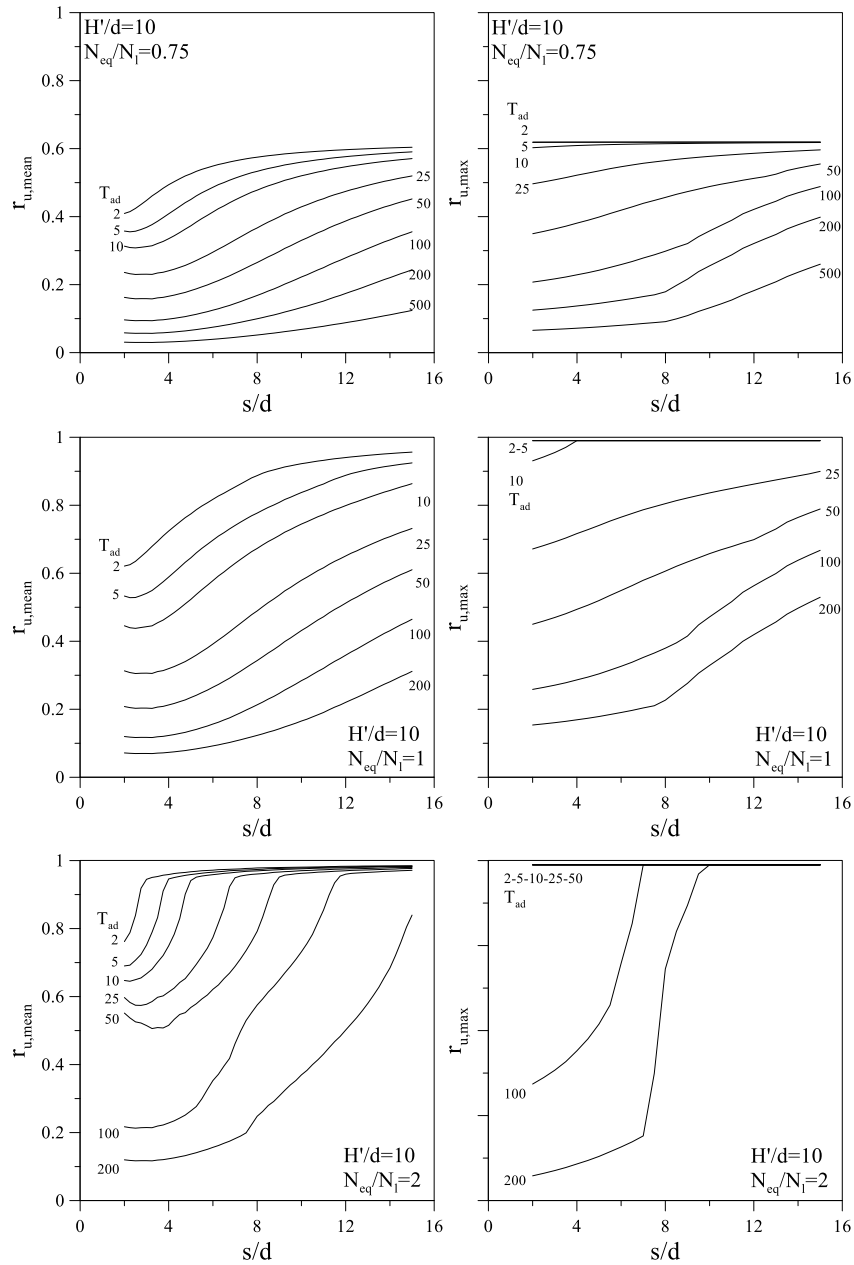


Figure 5.15 -  $r_u$  charts for  $H'/d=10$ . (De Sarno et al, 2019).



This project has received funding from the European Union's Horizon 2020 research and innovation programme under grant agreement No. 700748

#### 5.4 DESIGN METHOD FOR HORIZONTAL DRAINS

Based on the charts presented in the previous sections, it is possible to define a simple and straightforward method to design a set of horizontal drains for the mitigation of soil liquefaction.

The use of the charts as tool of design requires the definition of  $N_{eq}$  and  $t_d$ . Both these parameters are related to the seismic hazard of the site, and in literature different ways to quantify them are available (e.g. Green and Terri, 2005; Trifunac and Brady, 1975). To quantify  $T_{ad}$ , the hydraulic and mechanical properties of the liquefiable soil (in terms of volumetric compressibility  $m_v$  and hydraulic conductivity coefficient  $k$ ) and the drain diameter must be defined. Finally, it is necessary to know the soil resistance to liquefaction in terms of the number of equivalent constant amplitude cycles that lead to liquefaction,  $N_l$ . Hence the ratio  $N_{eq}/N_l$  may be calculated. Once the depth of the first row of drains,  $H'$ , is chosen, the ratio  $H'/d$  can be calculated and the related chart (for a given value of  $N_{eq}/N_l$ ) can be selected, while the curve to be used is defined by  $T_{ad}$ .

The last step is the definition of the design target for the mean (or maximum)  $r_u$ . Its value can be decided based on a reference limit state. The target value of  $r_u$  is chosen according to the procedure described in section 3.

Finally, once the target excess pore pressure ratio  $r_u$  is defined, a dimensionless spacing  $s/d$  can be obtained from the relevant chart.

An application can be carried out using the chart shown in Figure 5.16, for  $H'/d=10$ ,  $T_{ad}=50$  and  $N_{eq}/N_l=1$ . Supposing that the design mean excess pore pressure ratio  $r_{u,mean}$  is equal to 0.4, from the chart the design spacing  $s/d$  is around 11.5. Given the spacing, it is possible to verify that the value of  $r_{u,max}$  is acceptable: in this case it is equal to 0.69. It is worth noting that the  $s/d$  obtained from the design chart is almost equal to  $H'/d$ , which means that the maximum excess pore pressure ratio is likely to be achieved in the lower part of the domain, as discussed before. The design spacing can be optimized to achieve the best performance for the drains. Some hints are given in the next section, based on the result of a numerical parametric analysis that is described in Appendix C.



This project has received funding from the European Union's Horizon 2020 research and innovation programme under grant agreement No. 700748

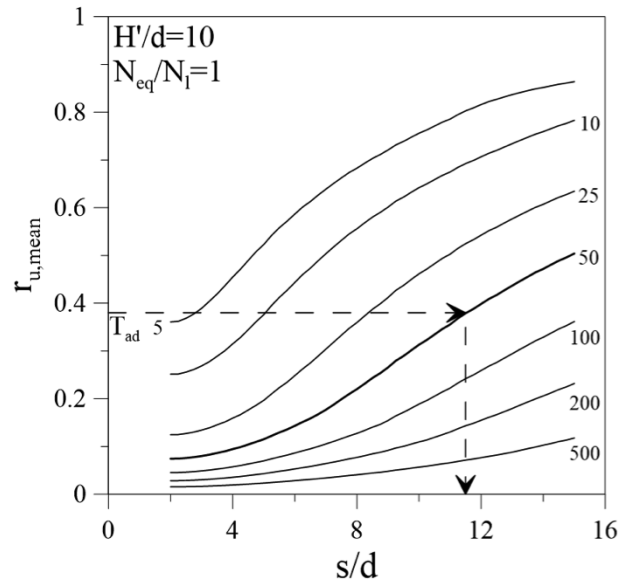


Figure 5.16 - Design charts for  $H'/d=10$  and  $N_{eq}/N_I=1$  (Fasano et al, 2019).

### 5.5 DESIGN HINTS

Parametric analyses described in detail in Appendix C (Liccardi, 2019) were performed by varying both the spacing between the drains ( $s/d$ ) and the depth of the first row ( $H'/d$ ). Efficiency was calculated both in terms of reduction of  $r_u$  and in terms of reduction of settlement at the ground surface, showing that the most efficient configurations are those characterised by the shallowest drains ( $H'/d=5$ ) with the smallest spacing ( $s/d=5$ ). Figure 5.17 sketches the effect of shallow drainage on the excess pore pressure distribution (single layer configuration). In the figure the black line represents the envelope of  $r_u$  distribution with depth during the earthquake without drains, the red line represents the corresponding envelope distribution with drains (enveloping the blue lines that are distributions at several epochs during the earthquakes).



This project has received funding from the European Union's Horizon 2020 research and innovation programme under grant agreement No. 700748

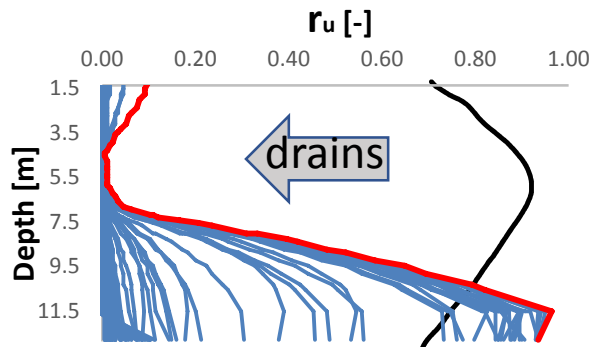


Figure 5.17 - Schematic effect of shallow drainage ( $H'/d=5$ ;  $s/d=5$ ).

It appears clearly in the figure that, for the chosen values of spacing, the presence of drains at a shallow depth reduces to very small (almost negligible) values the excess pore pressures around the drained area, while leaving substantially unchanged (or even increasing) the excess pore pressures in the deeper layers. Similar results were obtained also when a crust is present at the top of the liquefiable layer (see §C.2).

For such a reasons, attention was also paid to the accelerations at the ground surface or at the foundation level of the structure (see Appendix C). The results of the parametric analysis show that generally the use of horizontal drains produces an amplification of the response spectrum with respect to the conditions without drains. In fact, the presence of drains reduces excess pore pressure thus inhibiting the beneficial isolating effect provided by the liquefied layers. This may increase the amplitude of the acceleration spectrum at surface, which should be avoided since it may causes damage to the structures due to the inertial actions. However, shallow drains do not prevent excess pore pressure to build up in the deep soil, hence deep liquefaction can arise, avoiding amplification of the seismic signal that propagates to the ground surface. Therefore, shallow drains should be preferred also for this reason.

Finally, a further aspect that should be taken into account is the horizontal extension of the drains beyond the footprint of the building. In fact, the chart provided in the previous section are related to the geometrical condition of an infinite extension of the drain rows in the horizontal direction. From the results of the parametric analyses (Appendix C) it can be concluded that by extending the drained volume of ground to a distance  $B$  at the side of the structure, where  $B$  is the size of the footprint of the structure itself, the effectiveness of the mitigation action is very close to that occurring in the case of indefinite lateral extension of the drained ground.



This project has received funding from the European Union's Horizon 2020 research and innovation programme under grant agreement No. 700748

## 6 INDUCED PARTIAL SATURATION

### 6.1 INTRODUCTION

As well known, partial saturation increases the liquefaction resistance because of the very low volumetric stiffness of the gaseous phase in the soil. During undrained cyclic loading, if the soil tends to contract, the volume of the gas phase decreases and consequently the pore pressure build-up is reduced. This simple mechanism has a large effect even when the saturation degree is as high as 99%, and obviously becomes more and more relevant as the degree of saturation ( $S_r$ ) decreases as shown by several researchers (e.g. Chaney, 1978; Yoshimi et al., 1989; Ishihara et al., 2002; Nakazawa et al., 2004; Yegian, 2007; Kobayashi et al., 2010; Tsukamoto et al., 2014; Wang et al., 2016; Mele et al., 2018).

In unsaturated soils it is still possible to define an effective stress. Among the several proposals, the most used one to this aim is probably that proposed by Bishop and Blight (1963):

$$\sigma'_{un} = (\sigma - u_a) + \chi \cdot (u_a - u_w) \quad (19)$$

where  $\sigma$  is the total stress and  $u_a$ ,  $u_w$  and  $\chi$  are respectively the pore air pressure, the pore water pressure and the material parameter accounting for the effect of the degree of saturation. The term  $(\sigma - u_a)$  is called “net stress”, while  $(u_a - u_w)$  is the “matric suction” ( $s$ ). The parameter  $\chi$  is assumed equal to the degree of saturation  $S_r$  ( $\leq 100\%$ ), according to Wheeler et al., 2003; Gallipoli et al., 2003.

Based on an energetic interpretation of laboratory results of unsaturated tests, two possible design approaches have here proposed according to Mele and Flora, 2019, aiming at calculating the desired degree of saturation of a loose sand (design goal for IPS). To better understand these two approaches, the most important principles have been discussed as follow.

### 6.2 BACKGROUND ON ENERGETIC MODEL

During undrained cyclic triaxial loading of loose unsaturated sands, whatever the applied CSR,  $\epsilon_v$  increases to a final value  $\epsilon_{v,fin}$  at liquefaction which depends only on the initial state, defined for instance via the degree of saturation ( $S_{r0}$ ), the void ratio ( $e_0$ ) and the initial net stress  $(\sigma - u_a)_0$ , as shown in Figure 6.1 for tests carried out on unsaturated specimens of Sant'Agostino sand (D4.1).



This project has received funding from the European Union's Horizon 2020 research and innovation programme under grant agreement No. 700748

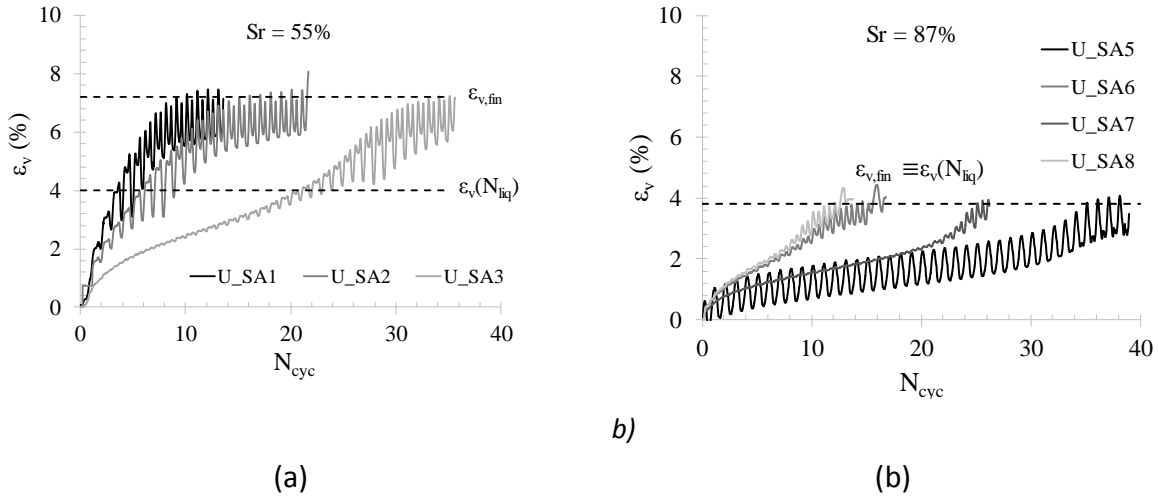


Figure 6.1 - Volumetric strain versus number of cycles (Mele et al., 2018).

Moreover, test results related to the same  $S_r$  plot in Figure 6.1a. All tests reach an effective stress,  $\sigma'_{un}$ , equal to 0 kPa at liquefaction, while as previously recalled the final volumetric strain depends on the initial degree of saturation. In Figure 6.1b the average curves for two different average degrees of saturation (55 and 87%) are also plotted.

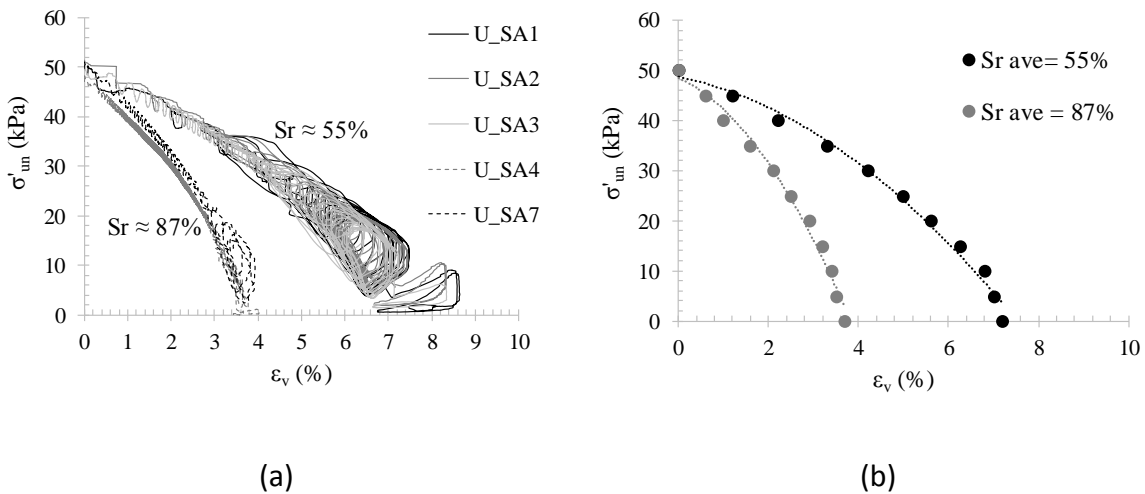


Figure 6.2 - Volumetric strain versus net stress for different degrees of saturation (a) and average curves (b) (Mele et al., 2018).

Considering the deformation process isothermal and applying Boyle and Mariotte law, the final volumetric strain at a constant confining total stress  $\sigma_c$  and with an initial air pressure  $u_{a,0}$  can be written as (Okamura and Soga, 2006; Mele et al., 2018):



This project has received funding from the European Union's Horizon 2020 research and innovation programme under grant agreement No. 700748

$$\varepsilon_{v,fin} = \frac{e_0}{1 + e_0} \cdot (1 - S_{r0}) \cdot \left(1 - \frac{u_{a,0}}{\sigma_c}\right) \quad (20)$$

Mele et al., 2018, showed that for the studied sands (Sant'Agostino, Bauxite and Inagi) a unique curve may be obtained in a non-dimensional plane ( $\sigma'_{un}/\sigma'_{un,0}:\varepsilon_v/\varepsilon_{v,fin}$ , Figure 6.2), having the expression:

$$\frac{\sigma'_{un}}{\sigma'_{un,0}} = 1 - \left(\frac{\varepsilon_v}{\varepsilon_{v,fin}}\right)^{1.7} \quad (21)$$

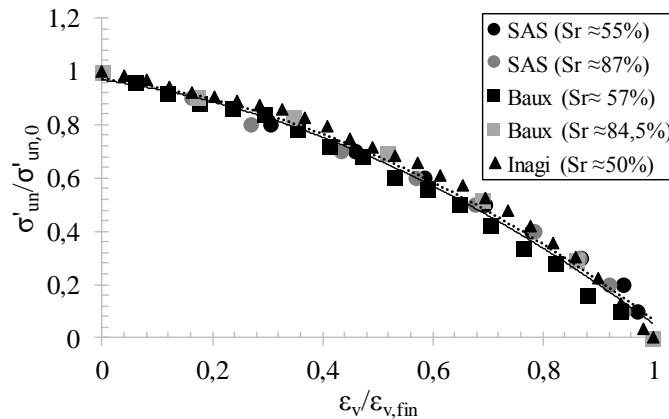


Figure 6.3 - Dimensionless effective stress vs. dimensionless volumetric strain for some of the tests reported by Mele et al. (2018).

Based on the showed experimental results, theoretical considerations have been done. A partially saturated soil can be considered as a three-phases thermodynamic system. In order to quantify the energy spent by the soil specimen during the pore pressure build-up process till liquefaction during laboratory testing, four hypotheses are introduced:

- the process is isothermal (i.e. no heat is generated or lost during the test);
- the mass of the system is constant (i.e. no increase or decrease of the mass of air, water or soil in the specimen during the test);
- the system is thermodynamically open (i.e. within the specimen, the deformation process implies internal flows of air and water);
- the pore gas (air) can be treated as an ideal gas.

The total specific energy of deformation  $E_{tot}$  needed to reach liquefaction can be seen as the sum of two components:



This project has received funding from the European Union's Horizon 2020 research and innovation programme under grant agreement No. 700748

$$E_{tot,liq} = E_{v,liq} + E_{s,liq} \quad (22)$$

where  $E_{v,liq}$  is the volumetric specific energy and  $E_{s,liq}$  is the deviatoric specific energy to reach liquefaction.

The volumetric specific energy can be seen as the sum of three components (Mele et al., 2018):

$$E_{v,liq} = E_{v,sk,liq} + E_{w,liq} + E_{air,liq} \quad (23)$$

$E_{v,sk,liq}$ ,  $E_{w,liq}$  and  $E_{air,liq}$  represent the specific work done respectively to cause the deformation of the soil skeleton, the flow of water and the flow of air into the pores network. They can be expressed as:

$$E_{v,sk,liq} = \int_0^{\varepsilon_{v,liq}} [(\sigma - u_a) + sS_r] \cdot d\varepsilon_v \quad (24)$$

$$E_{w,liq} = - \int_{S_{r0}}^{S_{r,liq}} \frac{e(S_r)}{1 + e(S_r)} s(S_r) \cdot dS_r \quad (25)$$

$$E_{air,liq} = \frac{e_0}{1 + e_0} (1 - S_{r,0}) u_{a,liq} d(\ln \rho_{a,liq}) \quad (26)$$

$E_{v,sk,liq}$  depends on the stress state ( $\sigma'_{un}$ ) and on the initial void ratio  $e_0$  ( $E_{v,sk,liq} = f(\sigma'(S_r), e_0)$ ), while it does not depend neither on CSR nor on  $N_{liq}$ . Obviously,  $E_{v,sk,liq}=0$  for undrained tests on saturated soils. The integral of eq.24 represents the area of the average curve  $\sigma'_{un}-\varepsilon_v$  (i.e. Figure 6.3) for a specific soil state. The integration extremes for the volumetric strains have to be assigned to calculate  $E_{v,liq}$ . These are 0 and  $\varepsilon_{v,liq}$ , respectively corresponding to the effective stresses (Bishop's notation)  $\sigma'_{un,0}$  and  $\sigma'_{un,liq}$ . The latter is the value of the effective stress at liquefaction and is not nil because of the conventional definition of liquefaction ( $\varepsilon_{DA}=5\%$ ). It can be calculated as a function of the initial degree of saturation  $S_{r0}$  using the following equation:

$$\frac{\sigma'_{un,liq}}{\sigma'_{un,0}} = -2 \cdot 10^{-4} \cdot S_{r0}^2 + 2 \cdot 10^{-2} \cdot S_{r0} + 0.1 \quad (27)$$

which is the best fitting curve of the experimental data presented by Mele et al. (2018).



This project has received funding from the European Union's Horizon 2020 research and innovation programme under grant agreement No. 700748

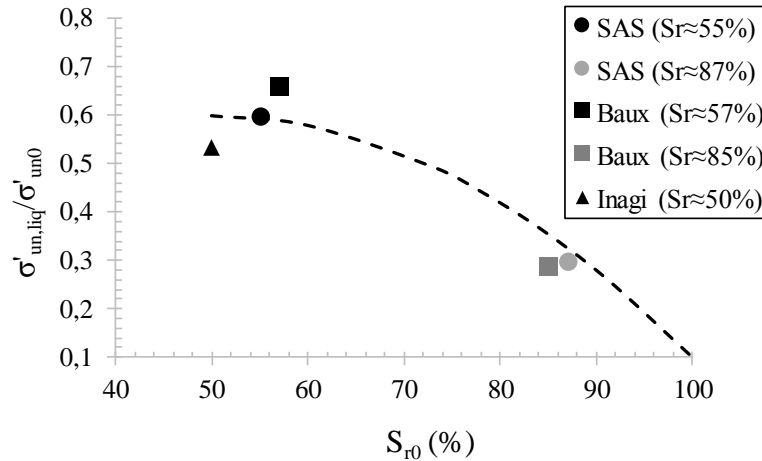


Figure 6.4 - Experimental values of  $\sigma'_{un,liq}/\sigma'_{un,0}$  and  $S_{r,0}$  (Mele et al, 2018), along with a best fitting curve (eq. 28).

$E_{w,liq}$  is the specific volumetric energy of water and it is due to the change of water content.  $E_{air,liq}$  describes the effect of pressure variation in the gas phase, and poses no problems in calculation.

Once the volumetric components have been defined, it is necessary to quantify the specific deviatoric energy of the soil skeleton spent to liquefaction,  $E_{s,liq}$ , connected to distortional strains  $\varepsilon_s$ . From a physical point of view,  $E_{s,liq}$  is the sum of the areas of all the cycles in the  $\varepsilon_s:q$  plane ( $D_{cyc}$  in Figure 6.5 for a single cycle) up to liquefaction (defined in terms of strains). Formally, for each cycle the energy is defined as:

$$E_{s,sk,liq} = \sum_{N_{cyc}=1}^{N_{cyc}=N_{liq}} \int \int_{D_{cyc}} dq \cdot d\varepsilon_s \quad (28)$$

Because of its definition,  $E_{s,liq}$  is strictly related to soil damping, and it thus quantifies the amount of energy dissipated during the distortional cyclic path. Therefore, it depends on soil properties, soil state and cyclic stress amplitude CSR.



This project has received funding from the European Union's Horizon 2020 research and innovation programme under grant agreement No. 700748

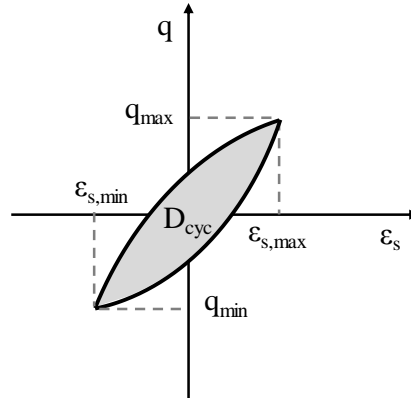


Figure 6.5 - Definition of the specific deviatoric energy  $E_{s,sk}$  for a single cycle in the  $q:\epsilon_s$  plane (Mele et al., 2018).

### 6.3 ENERGETIC APPROACHES TO PREDICT LIQUEFACTION RESISTANCE OF UNSATURATED SANDY SOILS

With the main aim to predict liquefaction resistance of unsaturated sandy soils, two simple approaches (Mele and Flora, 2019) have been discussed.

#### Approach 1

The volumetric specific energy  $E_{v,liq}$  (eqs. 24, 25, 26) is a function of the initial values of the effective confining stress (Bishop notation), of the void ratio and of the degree of saturation ( $E_{v,liq}=E_{v,liq}(\sigma'_{o, e0}, S_r)$ ), and increases from zero (for saturated soils) as  $S_r$  decreases. In this sense,  $E_{v,liq}$  may be seen as a synthetic state variable ruling the increment of liquefaction resistance of sands (at low confining stresses) from  $CRR_s$  ( $S_r=100\%$ ) to  $CRR_{un}$  ( $S_r<100\%$ ).

Mele and Flora (2019) showed the relationship between  $\Delta CRR^{ctx}$  (or  $\Delta CRR^{css}$ ) defined as  $\Delta CRR^{ctx}=CRR_{un}^{ctx}-CRR_s^{ctx}$  (or  $\Delta CRR^{css}=CRR_{un}^{css}-CRR_s^{css}$ ) for  $N_{liq} = 15$  and  $E_{v,liq}$  for the three tested sands, where  $CRR_{un}^{css}$  and  $CRR_s^{css}$  have been obtained by Castro's correlation (1975):

$$CRR^{css} = c_r \cdot CRR^{ctx} \quad (29a)$$

where  $c_r$  is:

$$c_r = \frac{2 \cdot (1 + 2K_0)}{3\sqrt{3}} \quad (29b)$$

in eq. (29b)  $k_0$  is the coefficient of earth pressure at rest, evaluated as  $K_0=1-\sin\phi_p$ , where  $\phi_p$  is the peak friction angle.



This project has received funding from the European Union's Horizon 2020 research and innovation programme under grant agreement No. 700748

Based on the experimental results reported in Figure 6.6, the relationships between  $E_{v,liq}$  and  $\Delta CRR_{N_{liq}}^{ctx}$  and  $\Delta CRR_{N_{liq}}^{css}$  (for  $N_{liq}=15$ ) can be expressed as:

$$\Delta CRR_{N_{liq}}^{ctx} = -105.7 \cdot \left(\frac{E_{v,liq}}{p_a}\right)^2 + 10.16 \cdot \frac{E_{v,liq}}{p_a} \quad (30a)$$

$$\Delta CRR_{N_{liq}}^{css} = -89.6 \cdot \left(\frac{E_{v,liq}}{p_a}\right)^2 + 7.81 \cdot \frac{E_{v,liq}}{p_a} \quad (30b)$$

Where  $p_a$  is the atmospheric pressure (98kPa).

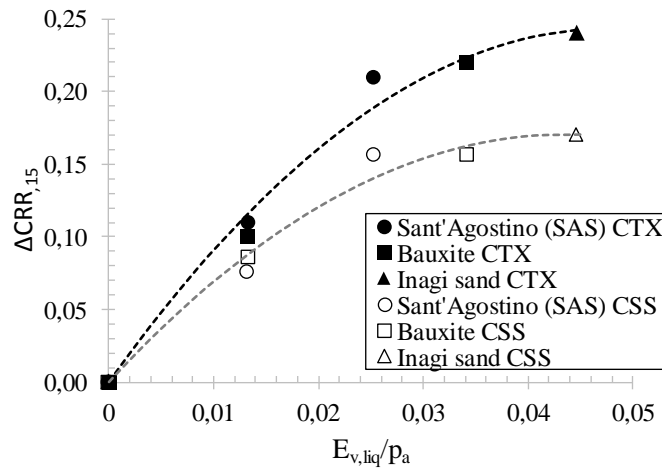


Figure 6.6 - Ratio between unsaturated and saturated liquefaction resistance at  $N_{cyc}=15$  ( $\Delta CRR_{,15}^{ctx}$  and  $\Delta CRR_{,15}^{css}$ ) versus  $E_{v,liq}/p_a$  (Mele and Flora, 2019).

### Approach 2

In this approach the deviatoric component of energy is also evaluated (eq. 28). Mele and Flora (2019) showed that a unique curve may be obtained by plotting the experimental data in the normalized plan in Figure 6.7 ( $E_{s,liq}$  vs  $(CRR^{ctx} \cdot (1 - 5 \cdot \frac{E_{v,liq}}{p_a})^{10})$ ). The equation has been provided:

$$E_{s,liq} = 0.297 \cdot p_a \cdot e^{-16.7 \cdot CRR^{ctx} \cdot \left(1 - 5 \cdot \frac{E_{v,liq}}{p_a}\right)^{10}} \quad (31a)$$



This project has received funding from the European Union's Horizon 2020 research and innovation programme under grant agreement No. 700748

Similarly, considering the cyclic resistance ratios in simple shear conditions a best fitting relationship is found as:

$$E_{s,liq} = 0.300 \cdot p_a \cdot e^{-23.7 \cdot CRR^{css} \cdot \left(1 - 5 \cdot \frac{E_{v,liq}}{p_a}\right)^{10}} \quad (31b)$$

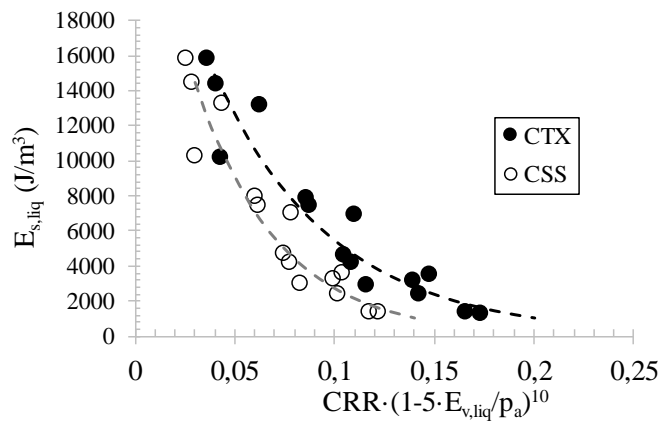


Figure 6.7 - Cyclic triaxial and corrected triaxial data (Castro correlation) in the plane  $CRR \cdot (1 - 5 \cdot E_{v,liq}/p_a)^{10}$  vs  $E_{s,liq}$  (Mele and Flora, 2019).

Moreover, a relationship between  $CRR^{ctx}/(1 + E_{tot,liq}/p_a)^6$  and  $N_{liq}$  have been reported in Fig. Figure 6.8.

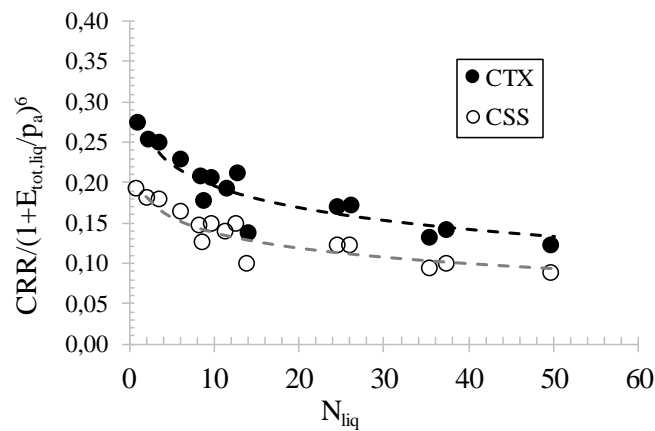


Figure 6.8 - Normalized cyclic resistance curves for cyclic triaxial and corrected data (Castro correlation) Mele and Flora, 2019).



This project has received funding from the European Union's Horizon 2020 research and innovation programme under grant agreement No. 700748

The best fitting of the experimental results in Figure 6.8 is:

$$\frac{CRR^{ctx}}{\left(1 + \frac{E_{tot,liq}}{p_a}\right)^6} = -0.039 \cdot \ln(N_{liq}) + 0.285 \quad (32a)$$

This can be transformed in simple shear conditions (eqs. 29a and 29b) as:

$$\frac{CRR^{css}}{\left(1 + \frac{E_{tot,liq}}{p_a}\right)^6} = -0.028 \cdot \ln(N_{liq}) + 0.202 \quad (32b)$$

### 6.3.1 CRR vs $q_{c1Ncs}$ for different value of $S_r$ .

From a technical point of view, the correlation between CRR and  $q_{c1Ncs}$  allows to evaluate the liquefaction susceptibility of a site. This correlation provided by Idriss and Boulanger (2014) has been reported in Figure 6.9 (eq. (33)).

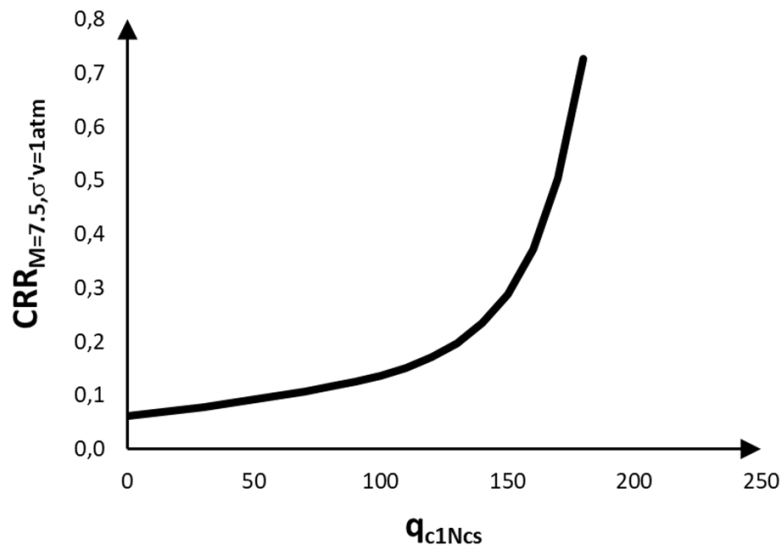


Figure 6.9 - CRR vs  $q_{c1Ncs}$  (Idriss and Boulanger, 2014).



This project has received funding from the European Union's Horizon 2020 research and innovation programme under grant agreement No. 700748

$$CRR_{M=7.5, \sigma' v=1atm} = \exp\left(\frac{q_{c1Ncs}}{113} + \left(\frac{q_{c1Ncs}}{1000}\right)^2 - \left(\frac{q_{c1Ncs}}{140}\right)^3 + \left(\frac{q_{c1Ncs}}{137}\right)^4 - 2.80\right) \quad (33)$$



This project has received funding from the European Union's Horizon 2020 research and innovation programme under grant agreement No. 700748

Where  $q_{c1Ncs}$  is given by:

$$q_{c1Ncs} = q_{c1N} + \Delta q_{c1N} \quad (34a)$$

$q_{c1N}$  and  $\Delta q_{c1N}$  may be evaluated by means of the following equations:

$$q_{c1N} = C_N \cdot q_{cN} = \frac{q_c}{p_a} \quad (34b)$$

$$\Delta q_{c1N} = \left( 11.9 + \frac{q_{c1N}}{14.6} \right) \exp \left( 1.63 - \frac{9.7}{FC+2} - \left( \frac{15.7}{FC+2} \right)^2 \right) \quad (34c)$$

Where  $q_c$  is cone tip resistance, FC is the fines content and  $C_N$  is the overburden correction factor defined as:

$$C_N = \left( \frac{p_a}{\sigma'_v} \right)^m \leq 1.7; \quad m = 1.338 - 0.249 \cdot (q_{c1Ncs})^{0.264} \quad (34d)$$

The relationship of Figure 6.9 has been found for saturated soils. Unsaturated curves for different  $S_r$  may be found through the energetic model as shown in Figure 6.10. The saturated curve of Boulanger and Idriss (2014) may be translated using the eq. (30b), once known  $E_{v,liq}$ , which can be easily calculated by eqs.(24, 25, 26). To evaluate  $E_{v,liq}$  the properties of Ticino sand (D4.1) have been considered, owing to the fact that it is a clean sand. In this simple condition  $q_{c1N}=q_{c1Ncs}$  and it is dependent on  $D_r$  as shown in the following equation (Idriss and Boulanger, 2008):

$$D_r = 0.478 \cdot (q_{c1Ncs})^{0.264} - 1.063 \quad (35)$$



This project has received funding from the European Union's Horizon 2020 research and innovation programme under grant agreement No. 700748

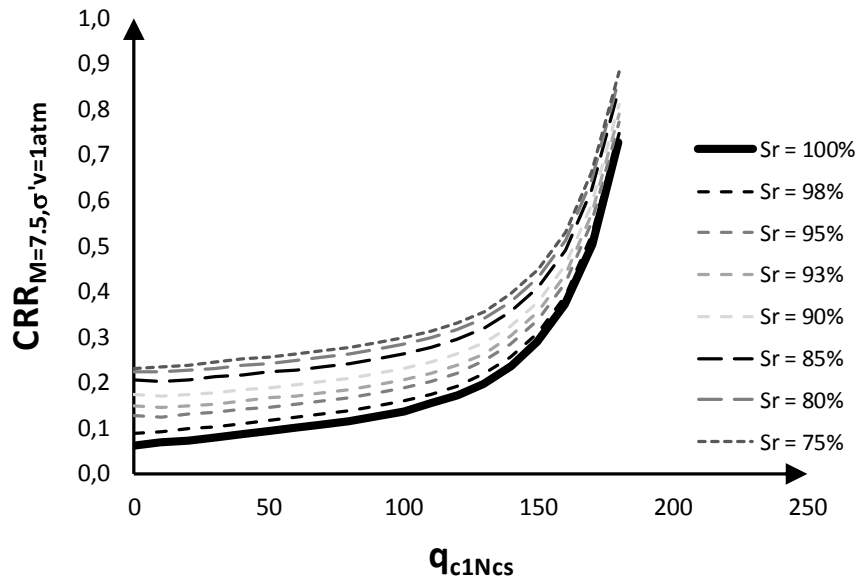


Figure 6.10 - CRR vs  $q_{c1Ncs}$  for different  $S_r$ .

#### 6.4 DESIGN METHOD FOR INDUCED PARTIAL SATURATION

In the design of IPS, the goal is to find what degree of saturation  $S_r$  is needed to guarantee for the structures to protect a satisfactory performance with reference to serviceability and limit conditions with the desired safety margins, with reference to any kind of mechanism related to liquefaction (Bray & Macedo, 2017). In particular, two scenarios may be foreseen: one in which the risk is linked to the attainment of liquefaction (i.e. a temporary but total loss of stiffness and strength of the liquefied soil), and one in which the pore pressure build up may trigger limit states in the structures (e.g. bearing capacity failure or excessive settlements) before liquefaction is reached. In the first case, an increase of  $CRR^{CSS}$  for the given value of  $N_{eq}$  (which is the number of cycles corresponding to the design seismic action) is needed. In the second case (which may refer to situations in which the safety margins against liquefaction may be sufficient in saturated conditions), it is simply asked to have lower pore pressures for  $N=N_{eq}$ . Formally, this may be seen as the need to increase, for the given value of CSR, the value of  $N_{liq}$  to a higher value  $N_{liq}^*$ . Both scenarios ask for an increase of soil capacity via IPS to cope with seismic demand, and the two procedures depicted in Figure 6.11 can be alternatively considered to this aim.



This project has received funding from the European Union's Horizon 2020 research and innovation programme under grant agreement No. 700748

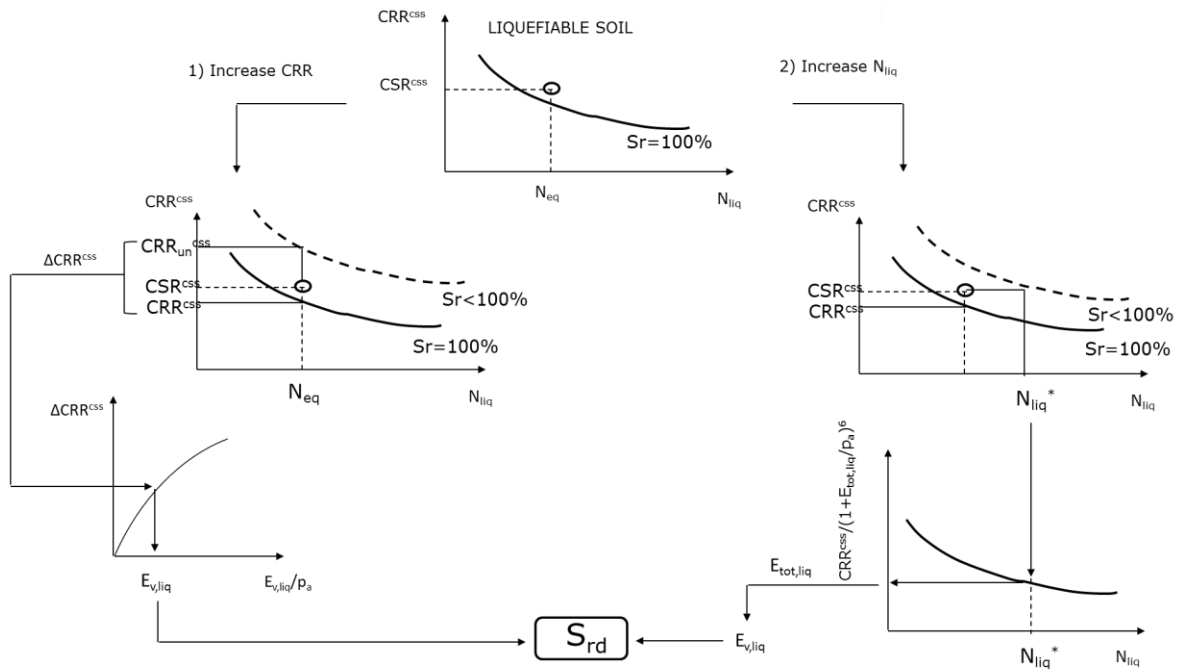


Figure 6.11 - Possible procedures to calculate the degree of saturation needed to increment liquefaction resistance of sandy soils. On the left: procedure 1 (increase CRR); on the right: procedure 2 (increase  $N_{liq}$ ).

#### 6.4.1 Procedure 1: increasing CRR

The first procedure, on the left side of Figure 6.11, refers to the need of increasing the safety factor against liquefaction. This means that the original safety margins are known (i.e., the saturated  $CRR^{CSS}-N_{liq}$  curve is known). In this case, it is trivial to know what increment of liquefaction resistance ( $\Delta CRR^{CSS}$ ) is needed once the desired safety margins are given, and therefore the previously proposed approach 1 is best suited as design tool. In fact, by knowing  $\Delta CRR^{CSS}$  it is possible to calculate  $E_{v,liq}$  (eq. 30b). For high values of  $S_r$  (as will generally be the case for IPS), the contribution of  $E_{w,liq}$  is negligible. Therefore,  $E_{v,liq}$  can be considered as the sum of two components ( $E_{v,sk,liq}$  and  $E_{air,liq}$ ). Through an iterative procedure, the design value of  $S_r$  ( $S_{rd}$ ) can be finally calculated. Notwithstanding the limitations of approach 1 previously discussed, it has to be highlighted that  $N_{liq}$  is usually lower than 20, and thus its use is confined to the range of values of  $N$  on which it has been experimentally tested.

#### 6.4.2 Procedure 2: increasing $N_{liq}$

In this case, the seismic action (CSR) leads for  $N=N_{eq}$  to excessive pore pressures (but not to liquefaction). There is the need to reduce such pore pressures, regardless of the original safety



This project has received funding from the European Union's Horizon 2020 research and innovation programme under grant agreement No. 700748

margins against liquefaction. The saturated liquefaction resistance curve is not a necessary design tool in this case, being the design goal to increase  $N_{liq}$  till  $N_{liq}^*$ .

The quantification of  $N_{liq}^*$  may be obtained once the maximum tolerable pore pressure  $u_{max}$  at  $N=N_{eq}$  has been evaluated with reference to the specific critical mechanism. In the case of bearing capacity failure triggered by pore pressure build up during seismic shaking, for instance, there are bearing capacity analytical formulations (e.g. Karamitros et al. 2013) from which the value of  $u_{max}(N_{eq})$  at failure can be calculated. Then, using an analytical expression for the pore pressure build up curve  $u=u(N)$  (e.g. Chiaradonna et al., 2018) calibrated on such a value,  $N_{liq}^*$  is obtained.

In this case, approach 2 is best suited as design tool, as depicted on the right side of Figure 6.11: once  $N_{liq}^*$  has been assigned, eq. 15b allows to know the ratio  $CRR^{CSS}/(1+E_{tot,liq}/p_a)^6$  (considering in this case  $CRR^{CSS}=CSR$ ). The total specific energy to liquefaction  $E_{tot,liq}$  is the sum of two components  $E_{v,liq}$  and  $E_{s,liq}$ , where  $E_{s,liq}$  can be computed as a function of CSR and  $E_{v,liq}$  (see Figure 6.2b, eq. 31b).  $E_{tot,liq}$  is therefore given by:

$$E_{tot,liq} = E_{v,liq} + 0.300 \cdot p_a \cdot e^{-23.7 \cdot CRR^{CSS} \cdot \left(1 - 5 \cdot \frac{E_{v,liq}}{p_a}\right)^{10}} \quad (36)$$

Using eq. (35), the design value  $S_{r,d}$  can be calculated as done with approach 1 with a simple iterative procedure.

## 6.5 DESIGN HINTS

A set of numerical parametric analyses, described in detail in Appendix D (Vaccaro, 2019), was performed by varying both the degree of saturation ( $S_r$ ) and the thickness of desaturated layer. Efficiency of desaturation was calculated both in terms of reduction of  $r_u$  and in terms of reduction of settlement at the ground surface. In general, similar values of efficiency were obtained both in terms of  $r_u$  and in terms of settlement. Results also show that the presence of an upper layer with low permeability (crust) has an important effect on the  $r_u$  profiles and this makes IPS less efficient.

The results indicate that the extension of the desaturated layer beyond the footprint of a building increases its efficiency in reducing excess pore pressure build-up. If desaturation is limited to the volume of ground just beneath the footprint of the building,  $B$ , its efficiency is about one third of that of an unsaturated layer of the same thickness that extends about  $3B$  on both sides of the building. This is obviously an issue to be considered in defining the extension of the mitigating action and the associated costs.

The target degree of saturation should be selected according to the criteria described in the previous section 7.4. However, it has to be considered that in order to guarantee the continuity of the fluid phase into the ground, such a value of  $S_r$  should not be too low. This



This project has received funding from the European Union's Horizon 2020 research and innovation programme under grant agreement No. 700748

implies that if the seismic demand is very high, desaturation can be ineffective (within an acceptable saturation degree).

Should the degree of saturation fall below the minimum accepted value, matrix suction may not be negligible. In this case the effect of suction on the soil stiffness, hence on the local seismic response, should be carefully considered. In fact, this may introduce local amplification of the acceleration at the ground (or foundation) level, that has not been considered within the scope of this study. On the other hand, the existence of suction would certainly have a beneficial effect on liquefaction related mechanisms, as bearing capacity failure or excessive settlement.



This project has received funding from the European Union's Horizon 2020 research and innovation programme under grant agreement No. 700748

## REFERENCES

- ACI Committee 440. Guide for the design and construction of externally bonded FRP systems for strengthening concrete structures. ACI 440.2R-08. Farmington Hills (MI): American Concrete Institute; 2008. p. 76.
- Airoldi, S., Fioravante, V., Giretti, D., Moglie, J., 2018. Validation of liquefaction retrofitting techniques from geotechnical centrifuge small scale models [WWW Document]. <https://doi.org/10.5281/ZENODO.1281598>
- Akguzel, U., and Pampanin, S., 2012. Assessment and design procedure for the seismic retrofit of reinforced concrete beam-column joints using FRP composite materials, *Journal of Composites for Construction*, ASCE, 16, 21-34.
- Alessio, G., Alfonsi, L., Brunori, C.A., Burrato, P., Casula, G., Cinti, F.R., Civico, R., Colini, L., Cucci, L., De Martini, P.M., Falcucci, E., Galadini, F., Gaudiosi, G., Gori, S., Mariucci, M.T., Montone, P., Moro, M., Nappi, R., Nardi, A., Nave, R., Pantosti, D., Patera, A., Pesci, A., Pezzo, G., Pignone, M., Pinzi, S., Pucci, S., Salvi, S., Tolomei, C., Vannoli, P., Venuti, A., Villani, F., 2013. Liquefaction phenomena associated with the Emilia earthquake sequence of May-June 2012 (Northern Italy). *Nat. Hazards Earth Syst. Sci.* 13, 935-947. <https://doi.org/10.5194/nhess-13-935-2013>
- Allouche, E.N., Ariaratnam, S.T., Lueke, J.S., 2000. Horizontal directional drilling: Profile of an emerging industry. *J. Constr. Eng. Manag.* 126, 68-76.
- Antonopoulos, C. P., and Triantafillou, T. C., 2003. Experimental investigation of FRP-strengthened RC beam-column joints, *Journal of Composite for Construction*, ASCE, 7, 39-50.
- Baker, W.H. (1982). "Planning and Performing Structural Chemical Grouting," *Proceedings, Grouting in Geotechnical Engineering*, held in New Orleans, Louisiana, on 10-12 February, Baker W.H. Ed., ASCE, New York, NY, Vol. 1, pp. 515-539.
- Bardet, J. P., Idriss, I. M., & O'Rourke, T. D. (1997). North America-Japan workshop on the geotechnical aspects of the Kobe, Loma Prieta, and Northridge earthquakes. A report to National Science Foundation, Air Force Office of Scientific Research, and Japanese Geotechnical Society, Osaka, Japan.
- Beaty, M.H., Byrne, P.M., 2011. UBCSAND CONSTITUTIVE MODEL Version 904aR, Itasca UDM Web Site.
- Biondi, G., Cascone, E., Di Filippo, G., 2012. Affidabilità di alcune correlazioni empiriche per la stima del numero di cicli di carico equivalente. *Riv. Ital. di Geotec.* 46, 9-39.
- Bishop A. W. & Blight G. E. (1963). Some aspects of effective stress in saturated and partly saturated soils. *Gèotechnique* 13, No. 3, 177-197, <https://doi.org/10.1680/geot.1963.13.3.177>.



This project has received funding from the European Union's Horizon 2020 research and innovation programme under grant agreement No. 700748

Booker JR, Rahman MS, Seed HB (1976) GADFLEA - A computer program for the analysis of pore pressure generation and dissipation during cyclic or earthquake loading. Earthquake Engineering Center, University of California, Berkeley.

Bouckovalas, G., Papadimitriou, A., Niarchos, D., 2009. Gravel drains for the remediation of liquefiable sites. Performance-Based Des. Earthq. Geotech. Eng. <https://doi.org/10.1201/NOE0415556149.ch4>

Boulanger R.W. and Hayden R.F. 1995. Aspects of compaction grouting of liquefiable soil. Journal of Geotechnical Engineering, ASCE, 121 (12), 844-855.

Boulanger RW, Idriss IM (2014) CPT and SPT based liquefaction triggering procedures. Report NO. UCD/CGM-14/01, Center for geotechnical modeling, Department of Civil and Environmental Engineering, University of California at Davis.

Boulanger, R. W., & Idriss, I. M. (2014). CPT and SPT based liquefaction triggering procedures. Report No. UCD/CGM.-14, 1.

Bousselham, A., 2010. State of research on seismic retrofit of RC beam-column joints with externally bonded FRP, Journal of Composite for Construction, ASCE, 14, 49-61.

Bray J. D. & Macedo J. (2017) Simplified procedure for estimating liquefaction-induced building settlement. Proceedings of the 19th International Conference on Soil Mechanics and Geotechnical Engineering, Seoul 2017.

Bray, J., Cubrinovski, M., Zupan, J., Taylor, M., 2014. Liquefaction effects on buildings in the central business district of Christchurch. Earthq. Spectra 30, 85-109. <https://doi.org/10.1193/022113EQS043M>

Brennan, A.J., Madabhushi, S.P.G. (2006). Liquefaction remediation by vertical drains with varying penetration depths. Soil Dynamics and Earthquake Engineering, 26 (5), pp. 469-475.

Brown D.R. and Warner J. (1973) Compaction grouting. Journal of soil mechanics and foundation division (ASCE) Vol.99 SM8 proceeding paper 9908, pp. 589-601.

Cascone E, Bouckovalas G (1998) Seismic bearing capacity of footings on saturated sand with a clay cap. Proceedings of the 11th European Conference on Earthquake Engineering, Paris.

Chaney R. (1978). Saturation effects on the cyclic strength of sands. In Earthquake engineering and soil dynamics, pp. 342-358. New York, NY, USA: American Society of Civil Engineers.

Chiaradonna A. and Flora A. (2019). On the estimate of seismically-induced pore water pressure increments before liquefaction. Submitted to Geotechnique Letters for possible publication.

Chiaradonna A., Tropeano G., d'Onofrio A., Silvestri F. (2018). Development of a simplified model for pore water pressure build-up induced by cyclic loading. Bulletin of Earthquake Engineering, BEE, 16, No. 9, 3627-3652, <https://doi.org/10.1007/s10518-018-0354-4>.



This project has received funding from the European Union's Horizon 2020 research and innovation programme under grant agreement No. 700748

- Chu, J., Stabnikov, V. & Ivanov, V. (2012). Microbially induced calcium carbonate precipitation on surface or in the bulk of soil. *Geomicrobiol. J.* 29, No. 6, 544-549
- Cooke, H.G.; Mitchell, J.K (1999) Guide to Remedial Measures for Liquefaction Mitigation at Existing Highway Bridge Sites. MCEER technical report 99/0015
- Copp, D. (2003). Partial saturation as a means of liquefaction mitigation in granular materials. PhD thesis, Swansea University, UK.
- Crank, J., Nicolson, P., Hartree, D.R., 1947. A practical method for numerical evaluation of solutions of partial differential equations of the heat-conduction type. *Math. Proc. Cambridge Philos. Soc.* 43, 50. <https://doi.org/10.1017/S0305004100023197>
- Croce P, Flora A, Modoni G (2014). *Jet Grouting: Technology, Design and Control.* CRC Press , 302 Pages.
- Cubrinovski M, Rhodes A, Ntritsos N, van Ballegooy S (2018) System Response of Liquefiable Deposits. *Soil Dynamics and Earthquake Engineering*, <https://doi.org/10.1016/j.soildyn.2018.05.013>
- D'Acunto, B., 2012. *Computational partial differential equations for engineering sciences.* Nova Science Publishers, New York.
- Der Kiureghian, A. (2002). Bayesian methods for seismic fragility assessment of lifeline components. *Acceptable Risk Processes-Lifelines and Natural Hazards*, 61-77.
- De Sarno D., Fasano G., Bilotta E., Flora A. (2018). Design method for horizontal drains in liquefiable soil. 7th International Conference on Earthquake Geotechnical Engineering, ICEGE 2019, Rome (Italy), June 2019.
- Di Ludovico, M., Balsamo, A., Prota, A., and Manfredi, G., 2008a. Comparative assessment of seismic rehabilitation techniques on a full-scale three-story RC moment frame structure, *Structural Engineering and Mechanics* 28, 727-747.
- Di Ludovico, M., Prota, A., Manfredi, G., and Cosenza, E., 2008b. Seismic strengthening of an under-designed RC structure with FRP, *Earthquake Engineering and Structural Dynamics* 37,141-162.
- Dobry, R., Leventis, G.E., Peck, R.B., Pecker, A. (2007). Rion-Antirion Bridge - an Olympian Effort Overcomes Extreme Geohazards, *Deep Foundations, The Magazine of the Deep Foundations Institute*, 5-8.
- El Ghoraiby MA, Park H, and Manzari MT (2017). LEAP 2017: Soil Characterization and Element Tests for Ottawa F65 Sand. The George Washington University, Washington DC.
- Engindeniz, M., Kahn, L. F., and Zureick, A. H., 2005. Repair and strengthening of reinforced concrete beam-column joints: state of the art, *ACI Structural Journal* 102, 187-197.



This project has received funding from the European Union's Horizon 2020 research and innovation programme under grant agreement No. 700748

- Eseller-Bayat, E. E. (2009). Seismic response and prevention of liquefaction failure of sands partially saturated through introduction of gas bubbles. PhD thesis, Northeastern University, Boston, MA, USA.
- Fasano G, De Sarno D., Bilotta E, and Flora A (2019) Design of horizontal drains for the mitigation of liquefaction risk. *Soils and Foundation*, (submitted).
- Fédération Internationale du Béton (fib), 2001. Externally bonded FRP reinforcement for RC structures, Bulletin 14, Lausanne, Switzerland, pp. 138.
- Ferritto, J. M. (1997). Seismic design criteria for soil liquefaction. Technical report TR-2077-SHR, Naval Facilities Engineering Service Center, Port Hueneme, California.
- Flora A, Lirer S, Silvestri F (2012) Undrained cyclic resistance of undisturbed gravelly soils. *Soil Dynamics and Earthquake Engineering* 43: 366-379.
- Flora A., G. Modoni, S. Lirer, P. Croce (2013). The diameter of single, double and triple fluid jet grouting columns: prediction method and field trial results. *Géotechnique*, 63, No. 11: 934-945. DOI 10.1680/geot.12.P.062.
- Gallipoli D., Gens A., Sharma R., Vaunat, J. (2003) An elastoplastic model for unsaturated soil incorporating the effects of suction and degree of saturation on mechanical behaviour. *Géotechnique* 53(1): 123-135.
- Graf E.D. (1969) Compaction grouting technique. *Journal of soil mechanics and foundation division (ASCE)* Vol.95 SM5 proceeding paper 6766, pp. 1151-1158.
- Graf, E. D. (1992). Compaction grout. In *Grouting, soil improvement and geosynthetics*, ASCE Geotechnical Special Publication No. 30, Vol. 1, pp. 275-287. Reston, VA: American Society of Civil Engineers.
- Green, R., Terri, G., 2005. Number of Equivalent Cycles Concept for Liquefaction Evaluations-Revisited. *J. Geotech. Geoenvironmental Eng.* 131, 477-488. [https://doi.org/10.1061/\(ASCE\)1090-0241\(2005\)131:4\(477\)](https://doi.org/10.1061/(ASCE)1090-0241(2005)131:4(477))
- Hamada, M., and O'Rourke, T. D., Eds. (1992). *Case Studies of Liquefaction and Lifeline Performance Duriruz Past Earthcwmkes: Technical Report NCEER-92-0001*. Vol. 1, National Center for Earthquake Engineering Research, State University of New York at Buffalo, NY.
- Harada, N., Towhata, I., Takatsu, T., Tsunoda, S., Sesov, V., 2006. Development of new drain method for protection of existing pile foundations from liquefaction effects. *Soil Dyn. Earthq. Eng.* 26, 297-312. <https://doi.org/10.1016/j.soildyn.2005.02.019>
- Harkes, M. P., van Paassen, L. A., Booster, J. L., Whiffin, V. S. & van Loosdrecht, M. C. M. (2010). Fixation and distribution of bacterial activity in sand to induce carbonate precipitation for ground reinforcement. *Ecol. Engng* 36, No. 2, 112-117



This project has received funding from the European Union's Horizon 2020 research and innovation programme under grant agreement No. 700748

Hausler E.A. and Sitar N. (2001). Performance of soil improvement techniques in earthquakes. Fourth International Conference on Recent Advances in Geotechnical Earthquake Engineering and Soil Dynamics, Paper 10.15.

Hayden, P.F., and Baez, J.I. (1994). "State of Practice for Liquefaction Mitigation in North America," Proceedings, International Workshop on Remedial Treatment of Liquefiable Soils, held in Tsukuba Science City, Japan, on 4-6 July.

HE, J., IVANOV, V., & CHU, J. (2013). Mitigation of liquefaction of saturated sand using biogas. *Géotechnique*, 63(4), 267-275.

Iai, S., Matsunaga, Y., Morita, T., and Sakurai, H. (1994a). "Effectiveness of Measures Against Liquefaction Confirmed at Recent Earthquake -A Case History During the 1993 Kushiro-Oki Earthquake, Proceedings of the 26th Joint Meeting of United States-Japan Panel on Wind and Seismic Effects: NIST SP 871, held in Gaithersburg, Maryland, on 17-20 May, N. Raufaste, Ed., U.S. Department of Commerce, National Institute of Standards and Technology, Gaithersburg, MD, pp. 213-325.

Iai, S., Matsunaga, Y., Morita, T., Miyata, M., Sakurai, H., Oishi, H., Ogura, H., Ando, Y., Tanaka, Y., and Kate, M. (1994b). "Effects of Remedial Measures Against Liquefaction at 1993 Kushiro-Oki Earthquake," Proceedings, Fifth Japan-U.S. Workshop on Earthquake Resistant Design of Lifeline Facilities and Countermeasures Against Soil Liquefaction: Technical Report NCEER-94-0026, held in Snowbird, Utah, on 29 September-1 October, T.D.

Idriss IM, Boulanger RW (2008) Soil liquefaction during earthquakes. Monograph MNO-12. Oakland, CA: Earthquake Engineering Research Institute.

Idriss, I. M., & Boulanger, R. W. (2008). Soil liquefaction during earthquakes. Earthquake Engineering Research Institute.

Idriss, I.M., 1999. An update to the Seed-Idriss simplified procedure for evaluating liquefaction potential. Proc., TRB Workshop New Approaches to Liq. Publ. n. FHWA-RD-99-165, Fed. Highw. Administration.

Ishihara K., Tsukamoto Y., Nakazawa H., Kamada K., and Huang Y. (2002). Resistance of partly saturated sand to liquefaction with reference to longitudinal and shear wave velocities. *Soils Found.*, 42, No. 6, 93-105.

Ishihara, K., Kawase, Y., and Nakajima, M (1980). "Liquefaction Characteristics of Sand Deposits at an Oil Tank Site during the 1978 Miyagiken-Oki Earthquake," *Soils and Foundation*, Japanese Society of Soil Mechanics and Foundation Engineering, Vol. 20, No. 2, pp. 97-111.

Ivanov, V. & Chu, J. (2008). Applications of microorganisms to geotechnical engineering for bioclogging and biocementation of soil in situ. *Rev. Environ. Sci. Biotechnol.* 7, No. 2, 139-153

Iwasaki T, Arakawa T, Tokida K (1984) Simplified Procedures for Assessing Soil Liquefaction During Earthquakes. *Soil Dynamics and Earthquake Engineering*, 3(1):49-58.



This project has received funding from the European Union's Horizon 2020 research and innovation programme under grant agreement No. 700748

JGS, 1998. The Japanese Geotechnical Society (Ed.), Remedial Measures against Soil Liquefaction. A.A. Balkema, Rotterdam.

Kakderi, K., & Argyroudis, S. (2014). Fragility Functions of Water and Waste-Water Systems. In SYNER-G: Typology Definition and Fragility Functions for Physical Elements at Seismic Risk (pp. 221-258). Springer Netherlands.

Karamitros D.K., Bouckovalas G.D., Chaloulos Y.K., Andrianopoulos K.I. (2013). Numerical analysis of liquefaction-induced bearing capacity degradation of shallow foundations on a two-layered soil profile. Soil Dynamics and Earthquake Engineering. Elsevier.

Karamitros DK, Bouckovalas GD, Chaloulos KI, Adrianopoulos KI (2013) Numerical analysis of liquefaction-induced bearing capacity degradation of shallow foundations on a two-layered soil profile. Soil Dynamics and Earthquake Engineering 44: 90-101

Kavazanjian, E., Jr. and O'Donnell, S. (2015). Mitigation of Earthquake-Induced Liquefaction via Microbial Denitrification: A Two-Phase Process. IFCEE 2015: pp. 2286-2295. doi: 10.1061/9780784479087.212

Kobayashi, M., Suemasa, N., Katada, T., & Nagao, K. (2010). Feasibility Study on Countermeasure against Liquefaction Using Micro Bubble. In The Twentieth International Offshore and Polar Engineering Conference. International Society of Offshore and Polar Engineers.

Kosho, A. (2011). Ground Improvement Using the Vibro - Stone Column Technique, 21st EYGEC, Rotterdam, 6 pages, 2011.

Lalic?, D. (2006). Metoda poboljšanja tla eksplozivom (A method of soil improvement by explosives), Gra?evinar 58, No. 3, 215-220, (in Croatian).

Liccardi E. (2019) Dreni orizzontali per la mitigazione del rischio di liquefazione del terreno. MSc Thesis University of Napoli Federico II (in Italian).

Marcuson WF III, Hynes ME, Franklin AG (1990). Evaluation and use of residual strength in seismic safety analysis of embankments. Earthquake Spectra 6(3): 529-572.

Mavroidou, M., Morgan, N.L., Sibanda, T., Serumaga, M., Bhamidimarri, R. (2011). Innovative Environmentally Responsible Techniques of Ground Improvement Stimulating Natural Processes, Proc. of the 12th Int. Conf. on Environmental Science and Technology, Rhodes, Greece, 8 p.

Mele L (2019) Personal communication.

Mele L, Lirer S, Flora A (2019) The specific deviatoric energy to liquefaction in saturated cyclic triaxial tests. 7th International Conference on Earthquake Geotechnical Engineering, Rome (Italy), June 2019.



This project has received funding from the European Union's Horizon 2020 research and innovation programme under grant agreement No. 700748

Mele L, Tan Tian J, Lirer S, Flora A, Koseki J (2018) Liquefaction resistance of unsaturated sands: experimental evidence and theoretical interpretation. *Géotechnique*. DOI: 10.1680/jgeot.18.p.042.

Mele L. and Flora A. (2019). On the prediction of liquefaction resistance of unsaturated sands. Submitted to *Soil Dynamics and Earthquake Engineering*.

Mitchell, J. K., Baxter, C. D. P., and Munson, T. C. 1995. "Performance of improved ground during earthquakes." *Soil improvement for earthquake hazard mitigation*, ASCE Geotechnical Special Publication No. 49, 423-438.

Mitchell, J.K., Cooke, H.G., Schaeffer, J.A., 1998. Design considerations in ground improvement for seismic risk mitigation. *Proc., Geotechnical Earthquake Engineering and Soil Dynamics III*. ASCE Geotechnical Special Publication No. 75, vol. 1, pp. 580- 613.

Mitchell, J.K., Wentz, F.J., 1991. Performance of improved ground during the Loma Prieta Earthquake University of California, Berkeley UCB/EERC Report 91/12.

Moseley M.P. and Priebe H.J. (1993), "Vibro techniques In Ground Improvement" (Moseley M.P. (ed.)). Blackie Academic and Professional, London, pp. 1-19

Nakazawa, H., Ishihara, K., Tsukamoto, Y., & Kamata, T. (2004). Case studies on evaluation of liquefaction resistance of imperfectly saturated soil deposits. In *Proceedings of International Conference on Cyclic Behaviour of Soils and Liquefaction Phenomena*, Bochum, Germany. Vol. 31, pp. 295-304.

National Academies (2016) *State of the Art and Practice in the Assessment of Earthquake-Induced Soil Liquefaction and Its Consequences*. Washington, DC: The National Academies National Academies of Sciences, Engineering, and Medicine. doi: 1017226/23474.

National Research Council (CNR DT-200/2004), 2004. *Guide for the Design and Construction of Externally Bonded FRP Systems for Strengthening Existing Structures*, Advisory Committee on Technical Recommendation for Construction of National Research council, Rome, 154 pp.

Okamura M. & Soga Y. (2006). Effects of pore fluid compressibility on liquefaction resistance of partially saturated sand. *Soils Found.* 46, No. 5, 695-700.

Okamura, M. & Soga, Y. (2006). Effects of pore fluid compressibility on liquefaction resistance of partially saturated sand. *Soils Found.* 46, No. 5, 695-700.

Okamura, M. & Teraoka, T. (2006). Shaking table tests to investigate soil desaturation as a liquefaction countermeasure. *Proceedings of seismic performance and simulation of pile foundations in liquefied and laterally spreading ground (GSP 145)*, pp. 282-293. University of California, Davis, CA, USA

Okamura, M., Ishihara, M. & Tamura, K. (2006). Degree of saturation and liquefaction resistances of sand improved with sand compaction pile. *J. Geotech. Geoenviron. Engng*, ASCE 132, No. 2, 258-264



This project has received funding from the European Union's Horizon 2020 research and innovation programme under grant agreement No. 700748

- Okamura, M., Takebayashi, M., Nishida, K., Fujii, N., Jinguji, M., Imasato, T., Yasuhara, H. & Nakagawa, E. (2011). In-situ desaturation test by air injection and its evaluation through field monitoring and multiphase flow simulation. *J. Geotech. Geoenviron. Engng, ASCE* 137, No. 7, 643-652.
- Ono, Y., Ito, K., Nakajima, Y., and Oishi, H. (1991). "Efficient Installation of Gravel Drains," Proceeding. Second International Conference on Recent Advances in Geotechnical Earthquake Engineering and Soil Dynamics, held in St. Louis, Missouri, on 11-15 March, S. Parkash, Ed., University of Missouri-Rolls, MO, Vol. 1, pp. 437-444.
- O'Rourke and M. Hamada, Eds., National Center for Earthquake Engineering Research, State University of New York at Buffalo, NY, pp. 135-152.
- O'Rourke, T. D., and Hamada, M., Eds. (1992). Case Studies of Liquefaction and Lifeline Performance During Past Earthquakes: Technical Report NCEER-92-0002. Vol. 2, National Center for Earthquake Engineering Research, State University of New York at Buffalo, NY.
- OYO Corporation. 2014. Report of soil investigation: Sendai District and Onahama District. Report from the PRENOLIN Project, Nice, France.
- Pande, G. N. & Pietruszczak, S. (2008). Assessment of risk of liquefaction in granular materials and its mitigation. Proc. 12th Int. Conf. Int. Assoc. Comput. Methods Adv. Geomech. (IACMAG), Goa, India, 2619-2627
- Pecker, A. (2006). Enhanced Seismic Design of Shallow Foundations: Example of the Rion Antirion Bridge, 4th Athenian Lecture on Geotechnical Engineering, 23 p.
- Petalas, A., 2012. PLAXIS LIQUEFACTION MODEL UBC3D-PLM.
- Pietruszczak, S., Pande, G. N. & Oulapour, M. (2003). A hypothesis for mitigation of risk of liquefaction. *Geotechnique* 53, No. 9, 833-838, <http://dx.doi.org/10.1680/geot.2003.53.9.833>.
- Pitilakis, K., Alexoudi, M., Argyroudis, S., Monge, O., & Martin, C. (2006). Earthquake risk assessment of lifelines. *Bulletin of Earthquake Engineering*, 4(4), 365-390.
- Pitilakis, K., Crowley, H., & Kaynia, A. (2014). SYNER-G: typology definition and fragility functions for physical elements at seismic risk. *Geotechnical, Geological and Earthquake Engineering*, 27.
- Plomteux, C., Ciortan, R. (2010). Integrated Ground Improvement Solution for the Largest Wind Farm Project in Europe, Proc. of the XIVth Danube-European Conf. on Geot. Engng., Bratislava, 8 p.
- Polito CP, Green RA, Lee J (2008) Pore pressure generation models for sands and silty soils subjected to cyclic loading. *Journal of Geotechnical and Geoenvironmental Engineering* 134(10): 1490-1500.



This project has received funding from the European Union's Horizon 2020 research and innovation programme under grant agreement No. 700748

- Priebe, H.J., 1989. The prevention of liquefaction by vibro-replacement. Proc., Earthquake Resistance Construction and Design, Berlin, Germany.
- Priebe, H.J., 1991. Vibro-replacement-design criteria and quality control. In: Esrig, Bachus (Eds.), Deep Foundation Improvements: Design, Construction, and Testing, ASTM STP 1089, pp. 62- 72. Philadelphia.
- Prota, A., Nanni, A., Manfredi, G., and Cosenza, E., 2004, Selective upgrade of under-designed reinforced concrete beam-column joints using carbon fiber-reinforced polymers, ACI Structural Journal 101, 699-707
- Puebla, H., Byrne, P.M., Phillips, R., 1997. Analysis of CANLEX liquefaction embankments: prototype and centrifuge models. Can. Geotech. J. 34, 641-657. <https://doi.org/10.1139/t97-034>
- Ramirez J, Barrero AR, Cheng L et al. (2018) Site Response in a Layered Liquefiable Deposit: Evaluation of Different Numerical Tools and Methodologies with Centrifuge Experimental Results. Journal of Geotechnical and Geoenvironmental Engineering ASCE 144(10): 04018073, <http://ascelibrary.org/doi/10.1061/%28ASCE%29GT.1943-5606.0001947>.
- Régnier J, Bonilla L-F, Bard P-Y et al. (2018) PRENOLIN: International benchmark on 1D nonlinear site-response analysis - Validation phase exercise. Bull Seismol Soc Am 108(2): 876-900. DOI: <https://doi.org/10.1785/0120170210>.
- Rendulic, L., 1936. Porenziffer und porenwasserdruck in tonen. Der Bauingenieur 17, 559-564.
- Robertson PK, Wride CE (1998) Evaluating cyclic liquefaction potential using the cone penetration test. Canadian Geotechnical Journal 35(3): 442-459.
- Sasaki, Y., and Taniguchi, E. (1982). "Shaking Table Tests on Gravel Drains to Prevent Liquefaction of Sand Deposits," Soils and Foundations, Japanese Society of Soil Mechanics and Foundation Engineering, Vol. 22, No. 3, pp. 1-14.
- Seed HB and Idriss IM (1971) Simplified Procedure for Evaluating Soil Liquefaction Potential. Journal of the Soil Mechanics and Foundations Division ASCE 97(SM9): 1249-1273.
- Seed, H.B., and Booker, J.R. (1977). "Stabilization of Potentially Liquefiable Sand Deposits Using Gravel Drains," Journal of the Geotechnical Engineering Division, ASCE, New York, NY, Vol. 103, No. GT7, July, pp. 757-768.
- Seed, H.B., Booker, J.R., 1976. Stabilization of potentially liquefiable sand deposits using gravel drains. ASCE, J. Geotech. Eng. Div. <https://doi.org/10.1017/CBO9781107415324.004>
- Seed, H.B., Idriss, I.M., Makdisi, F., Banerjee, N., 1975. Representation of irregular stress time histories by equivalent uniform stress series in liquefaction analyses. Rep. No. EERC 75-29, Earthq. Eng. Res. Center, Univ. California, Berkeley, Calif. 40 pp.
- Seed, H.B., Martin, P.P., Lysmer, J., 1975. The generation and dissipation of pore water pressures during soil liquefaction. College of Engineering, University of California.



This project has received funding from the European Union's Horizon 2020 research and innovation programme under grant agreement No. 700748

- Seed, R. B., Cetin, K. O., Moss, R. E. S., Kammerer, A. M., Wu, J., Pestana, J. M., Faris, A. (2003). Recent advances in soil liquefaction engineering: A unified and consistent framework. Proceedings of the 26th Annual ASCE Los Angeles Geotechnical Spring Seminar. H.M.S. Queen Mary, Long Beach, California.
- Stabnikov, V., Naemi, M., Ivanov, V. & Chu, J. (2011). Formation of water-impermeable crust on sand surface using biocement. *Cement Concrete Res.* 41, No. 11, 1143-1149
- Stamatopoulos, K., Petridis, P., Balla, L., Allkja, S., Bozo, L., Vatselas, G., Loukatos, G., Modaressi, A., Lopez-Caballero, F., Small, A. (2011). Preloading to Mitigate Seismic Liquefaction Risk, Albanian Geotechnical Society, Landslides and Geo-Environment, Geotechnical Symposium in Balkan Region, Tirana, 8 pages.
- Stevenson, J.R., Kachali, H., Whitman, Z., Seville, E., Vargo, J., Wilson, T., 2011. Preliminary observations of the impacts the 22 February Christchurch earthquake had on organisations and the conomy: A Report from the Field (22 February-22 March 2011). *Bull. New Zeal. Soc. Earthq. Eng.* 44, 65.
- Trifunac, M.D., Brady, A.G., 1975. A study on the duration of strong earthquake ground motion. *Bull. Seismol. Soc. Am.* 65, 581-626. [https://doi.org/10.1016/0148-9062\(76\)90487-3](https://doi.org/10.1016/0148-9062(76)90487-3)
- Tsukamoto, Y., Kawabe, S., Matsumoto, J., & Hagiwara, S. (2014). Cyclic resistance of two unsaturated silty sands against soil liquefaction. *Soils and Foundations*, 54(6), 1094-1103.
- Vaccaro D. (2019) Parziale saturazione indotta per la mitigazione del rischio di liquefazione del terreno. MSc Thesis University of Napoli Federico II (in Italian).
- Van Ballegooy S, Malan P, Lacrosse V et al. (2014) Assessment of liquefaction-induced land damage for residential Christchurch. *Earthquake Spectra*, 30(1):31-55.
- Vasko A (2015) An Investigation into the Behavior of Ottawa Sand through Monotonic and Cyclic Shear Tests. Masters Thesis, The George Washington University.
- Wang H., Koseki J., Sato T., Chiaro G., and Tan Tian J. (2016). Effect of saturation on liquefaction resistance of iron ore fines and two sandy soils. *Soils Found.* 56, No. 4, 732-744.
- Watanabe, T. (1966). "Damage to Oil Refinery Plants and a Building on Compacted Ground by the Niigata Earthquake and Their Restoration," *Soils and Foundations*, Japanese Society of Soil Mechanics and Foundation Engineering, Vol. 6, No. 2, pp. 86-99.
- Wheeler S. J., Sharma R. S., Bulsson M. S. R. (2003) Coupling of hydraulic hysteresis and stress-strain behavior in unsaturated soils. *Gèotechnique* 53(1): 41-54.
- Whiffin, V. S., van Paassen, L. A. & Harkes, M. P. (2007). Microbial carbonate precipitation as a soil improvement technique. *Geomicrobiol. J.* 24, No. 5, 417-423
- Woeste D., Green R., Rodriguez-Marek A., Ekstrom L. (2016). A review of verification and validation of ground improvement techniques for mitigating liquefaction. Center for Geotechnical Practice and Research, Virginia Tech, Blacksburg, VA, 106 pp.



This project has received funding from the European Union's Horizon 2020 research and innovation programme under grant agreement No. 700748

Yegian M. K., Eseller-Bayat E., Alshawabkeh A. and Ali S. (2007). Induced-Partial Saturation for liquefaction mitigation: experimental investigation. *J. Geotech. Geoenviron. Engng ASCE* 133, No. 4, 372-380.

Yegian M.K., Eseller-Bayat E., Alshawabkeh A., Ali S. (2007) Induced-Partial Saturation for Liquefaction Mitigation: Experimental Investigation *Journal of Geotechnical and Geoenvironmental Engineering*, Vol. 133, No. 4, April 1, 2007. ©ASCE, ISSN 1090-0241/2007/4-372-380.

Yegian, M. K., Eseller, E. & Alshawabkeh, A. (2006). Preparation and cyclic testing of partially saturated sands. *Proc. 4th Int. Conf. on Unsaturated Soils (GSP 147)*, Carefree, AZ, 508-518

Yoshimi Y., Yanaka K., and Tokimatsu K., (1989). Liquefaction resistance of partially saturated sand. *Soils Found.*, 29, No. 2, 157-162.

Youd T. L., Idriss I .M, Andrus R. D., Arango I., Castro G., Christian J. T, Dobry R., Finn W. D. L., Harder L. F. Jr, Hynes M. E., Ishihara K., Koester J. P., Liao S. S. C., Marcuson W. F III, Martin G. R., Mitchell J. K., Moriwaki Y., Power M. S., Robertson P. K., Seed R. B., Stokoe II K. H. 2001. "Liquefaction resistance of soils: Summary report from the 1996 NCEER and 1998 NCEER/NSF workshops on evaluation of liquefaction resistance of soils." *Journal of Geotechnical and Geoenvironmental Engineering* 127 (10), 817-833).

Zen, K. et al. (1997) "Study on a reclamation method with cement-mixed sandy soils - Fundamental characteristics of treated soils and model tests on the mixing and reclamation." *Technical Note of the Port and harbor Research Institute*, no. 579, 41 p.

Ziotopoulou K (2010) Evaluating model uncertainty against strong motion records at liquefiable sites. *Master of Science in Civil and Environmental Engineering*, University of California, Davis, USA.



This project has received funding from the European Union's Horizon 2020 research and innovation programme under grant agreement No. 700748

## Appendix A – definition of $q_{c1Ncs}$ and $(N_1)_{60cs}$

Boulanger and Idriss (2014) define the following normalized resistances:

For CPT

$$q_{c1Ncs} = q_{c1N} + \Delta q_{c1N} \quad (A1)$$

where:

$$q_{c1N} = C_N \cdot \frac{q_c}{P_a} \quad (A2)$$

$$C_N = \left( \frac{P_a}{\sigma'_v} \right)^m \leq 1.7 \quad (A3)$$

$$m = 1.338 - 0.249 \cdot q_{c1Ncs}^{0.264} \quad (A4)$$

$$\Delta q_{c1N} = \left( 11.9 + \frac{q_{c1N}}{14.6} \right) \exp \left( 1.63 - \frac{9.7}{FC+2} - \left( \frac{15.7}{FC+2} \right)^2 \right) \quad (A5)$$

where  $q_c$  is the cone resistance measured during CPT,  $p_a$  is the atmospheric pressure and FC is the fine content, i.e., the percentage of soil having particles diameter smaller than 0.075 mm. The value of  $q_{c1Ncs}$  must be found by trial and error.

For SPT

$$(N_1)_{60cs} = (N_1)_{60} + \Delta(N_1)_{60} \quad (A6)$$

where:

$$(N_1)_{60} = C_N \cdot N_{60} \quad (A7)$$

$C_N$  is given by equation (17), the exponent  $m$  being:

$$m = 0.784 - 0.0768 \cdot (N_1)_{60cs}^{0.5} \quad (A8)$$

$$\Delta(N_1)_{60} = \exp \left( 1.63 + \frac{9.7}{FC+0.01} - \left( \frac{15.7}{FC+0.01} \right)^2 \right) \quad (A9)$$

where  $N_{60}$  is the energy-corrected blow count measured during SPT.



This project has received funding from the European Union's Horizon 2020 research and innovation programme under grant agreement No. 700748

## Appendix B – procedure to build the analytical expressions of $b(q_{c1Ncs})$ , $b((N_1)_{60cs})$ , $\beta(FC, q_{c1Ncs}, \Delta q_{c1N})$ , $\beta(FC, (N_1)_{60cs}, \Delta(N_1)_{60})$

The magnitude scaling factor is defined as:

$$MSF = \frac{CSR}{CSR_{M=7.5}} = \left( \frac{N_{M=7.5}}{N} \right)^b \quad (B1)$$

where  $N_{M=7.5}$  and  $CSR_{M=7.5}$  are the number of equivalent loading cycles and the cyclic stress ratio for a magnitude,  $M$ , equal to 7.5. The maximum value of  $MSF$  ( $MSF_{max}$ ) corresponds to the minimum number of cycles,  $N_{min}$ . Then, from equation (B1):

$$MSF_{max} = \left( \frac{N_{M=7.5}}{N_{min}} \right)^b \quad (B2)$$

Boulanger and Idriss (2014) propose to express  $N_{min}$  as:

$$N_{min} = \left( \frac{1}{0.65} \right)^{1/b} \cdot \left( \frac{3}{4} \text{cycles} \right) \quad (B3)$$

and  $N_{M=7.5}$  can be expressed as a function of the parameter  $b$  interpolating the mean values of a large number of data collected by Boulanger and Idriss (2014) (Figure B. 1) with the following analytical expression:

$$N_{M=7.5} = \frac{18.61 \cdot b^2 - 3.71 \cdot b + 0.38}{b^2 - 0.091 \cdot b + 0.0021} \quad (B4)$$



This project has received funding from the European Union's Horizon 2020 research and innovation programme under grant agreement No. 700748

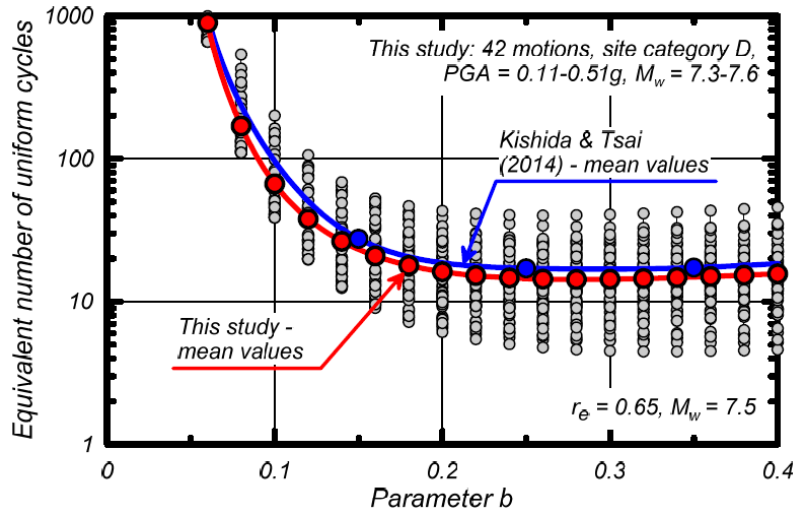


Figure B. 1 - Variation of (a)  $N_{M=7.5}$  with the parameter  $b$  (after Boulanger and Idriss, 2014)

Boulanger and Idriss (2014) also relate  $MSF_{max}$  to  $q_{c1Ncs}$  and  $(N_1)_{60cs}$  as:

$$MSF_{max} = 1.09 + \left( \frac{q_{c1Ncs}}{180} \right)^3 \leq 2.2 \quad (B5)$$

$$MSF_{max} = 1.09 + \left( \frac{(N_1)_{60cs}}{31.5} \right)^2 \leq 2.2 \quad (B6)$$

Finally, by combining equations from (B2) to (B5), the parameter  $b$  of equation (6) can be expressed as a function of  $q_{c1Ncs}$  or  $(N_1)_{60cs}$  as shown in Figure B. 2 and equations (13).



This project has received funding from the European Union's Horizon 2020 research and innovation programme under grant agreement No. 700748

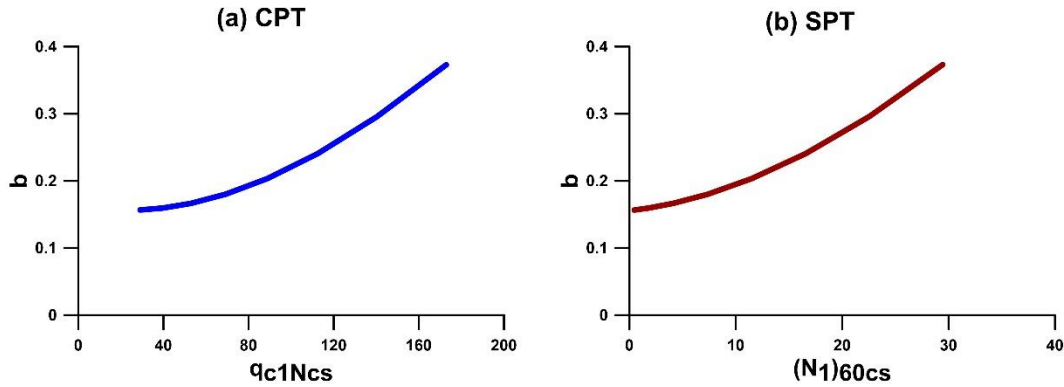


Figure B. 2 - Relationship between  $\beta$  and  $q_{c1Ncs}$  (a) or  $(N_1)_{60cs}$  (b)

The parameter  $\beta$  of equation (11) can be conveniently expressed as a function of FC and  $D_r$  in percent as (Polito et al., 2008):

$$\beta = 0.01166 \cdot FC + 0.007397 \cdot D_r + 0.5058 \quad (B7)$$

Valid for  $FC < 35\%$ .  $D_r$  can be related to  $q_{c1N}$  or  $(N_1)_{60}$  as (Idriss and Boulanger, 2008):

$$D_r = 100 \cdot (0.478 \cdot q_{c1N}^{0.264} - 1.063) \quad (B8a)$$

$$D_r = 100 \cdot \sqrt{\frac{(N_1)_{60}}{46}} \quad (B8b)$$

Then, by substituting equations (B7) in equation (B6),  $\beta$  can be expressed as a function of either  $q_{c1N}$  and FC, or  $(N_1)_{60}$  and FC. Since the combination of  $q_{c1N}$  and FC results into the parameter  $q_{c1Ncs}$ , and the combination of  $(N_1)_{60}$  and FC result into  $(N_1)_{60cs}$ ,  $\beta$  can be also expressed directly as a combined function of FC and  $q_{c1Ncs}$ , or  $(N_1)_{60cs}$ , as indicated by equations (14) and shown in Figure B. 3.



This project has received funding from the European Union's Horizon 2020 research and innovation programme under grant agreement No. 700748

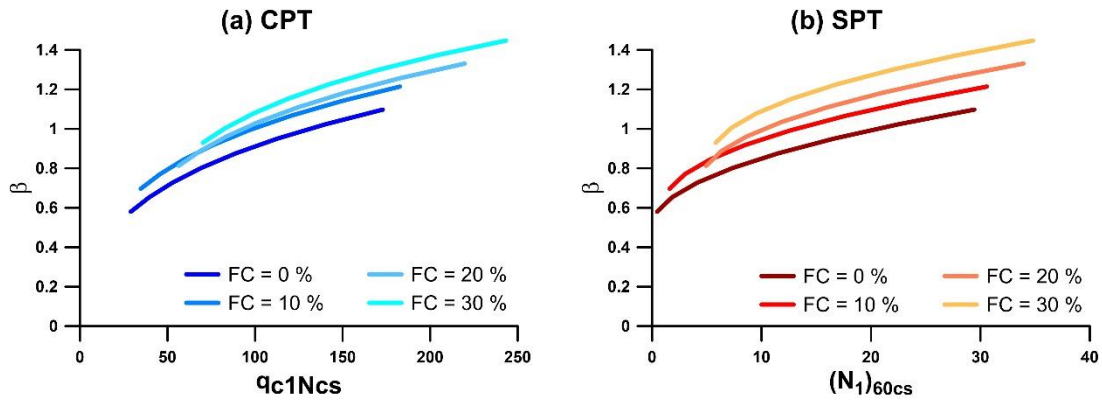


Figure B. 3 - Relationship between  $\beta$  and  $qc1Ncs$  (a) or  $(N_1)_{60cs}$  (b) for different FC



This project has received funding from the European Union's Horizon 2020 research and innovation programme under grant agreement No. 700748

## Appendix C – HORIZONTAL DRAINS PARAMETRIC ANALYSES

The parametric study for the case of horizontal drains has been carried out by using the Finite Element code Plaxis 2D, as described in chapter 6 of Deliverables D4.4 “Database of calibrated numerical modelling results”. The numerical model was initially calibrated against the results of centrifuge tests. Hence the analyses were carried out considering to other configurations, in order to verify the efficiency of this technique.

In the parametric analyses the spacing between the drains ( $s/d$ ) and the depth of the first row of drains from the groundwater ( $H'/d$ ) were changed (Figure C. 1). The main set of analyses is aimed to reproduce the same geometrical layout of the numerical solution describe in §5.3, that is an indefinite horizontal drained layer (made of three rows of horizontal drains). However, the effect of the horizontal extension of the layer has been also investigated (§C.4).

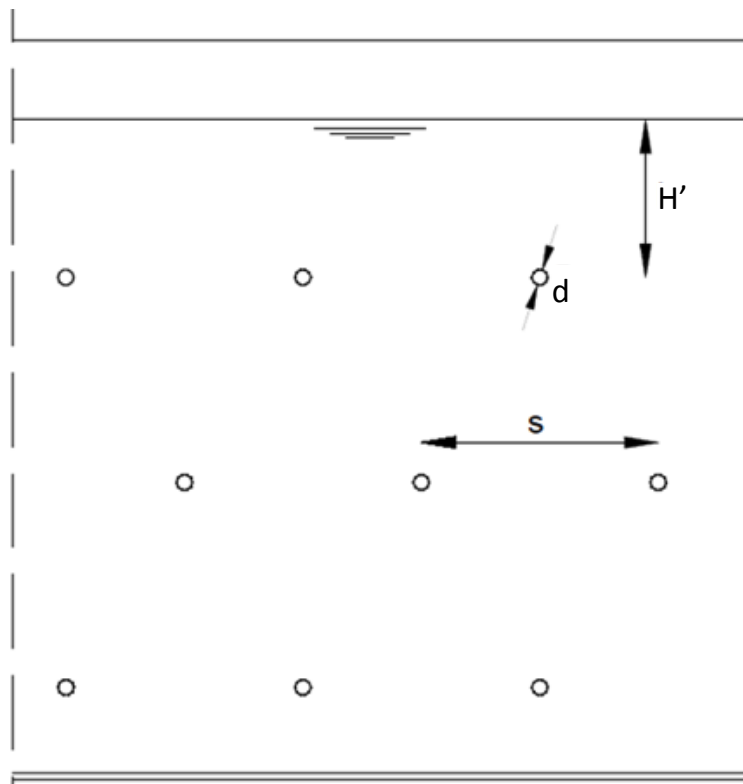


Figure C. 1 - Scheme of the adopted configurations.

The soil behaviour was modelled by PM4sand constitutive model (see D4.4). The drains were modelled by imposing a constant hydraulic head condition along their surface. Tied degrees of freedom between vertical sides of the mesh were used as boundary conditions to



This project has received funding from the European Union's Horizon 2020 research and innovation programme under grant agreement No. 700748

reproduce the equivalent shear box used in the centrifuge. This option proposed by Zienkiewicz et al. (1989) connects the nodes on the same elevation at the left and right model boundaries. The nodes at the base of the finite element model were fixed in the vertical direction and a time history of acceleration was applied in the horizontal direction. Drainage across the top surface is allowed whereas flow across the lateral boundaries is restricted. The input signal used and the structure are the same used in the centrifuge tests.

The adopted configurations are summarized in the Table C. 1.

Table C. 1 - Layout of drains

<b>H'/d</b>	5	5	5	10	10	10	15	15	15
<b>s/d</b>	5	10	15	5	10	15	5	10	15

For each layout of drains both the free-field and the model including a structure (single frame model building as in the centrifuge tests) were analysed. Starting from the simulation of the centrifuge test, with a model depth of 13 m at prototype scale, the analyses were repeated for a deeper layer (17 m deep) to verify possible boundary effect in the models with the deepest drains.

The profiles of  $r_u$  every 0.5 seconds are plotted in Figure C. 2 for one of the analysed configurations of (H'/s=5, s/d=5) and the red line represents the envelope of all curves.



This project has received funding from the European Union's Horizon 2020 research and innovation programme under grant agreement No. 700748

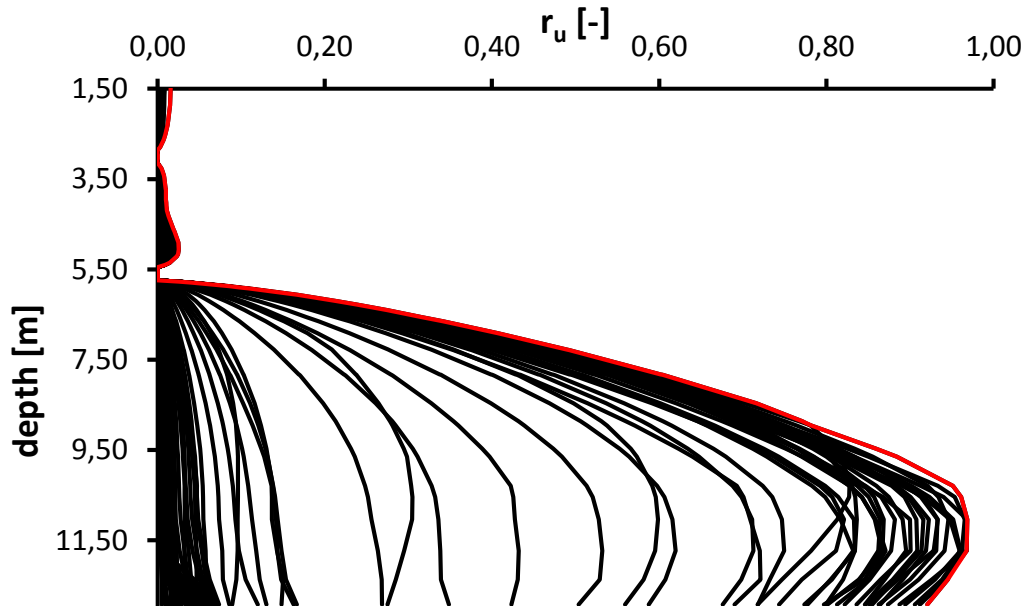


Figure C. 2 –  $r_u$  profile every 0.5s in a vertical of the model ( $H' / d = 5$  s /  $d = 5$ , without structure)

In free field conditions the  $r_u$  profiles were computed along a vertical line at the mid-span of the model. In the models with the structure, the profiles were computed:

- along a vertical line outside the footprint of the structure;
- beneath the structure, along its the vertical axis;
- beneath the structure, along the vertical axis of a foundation beam.

To compare the results of the different analyses two parameters were used, capable of providing information regarding the drains efficiency:

- efficiency in terms of  $r_u$ , defined as:

$$E_{r_u} = 1 - \frac{\int_0^z r_{u,treated}}{\int_0^z r_{u,untreated}} \quad (C1)$$

- efficiency in terms of settlement, defined as:

$$E_{\delta} = 1 - \frac{\delta_{treated}}{\delta_{untreated}} \quad (C2)$$

The efficiency in terms of  $r_u$  has always been evaluated considering the envelopes of the  $r_u$  profiles over time. It has been calculated up to a certain depth, z. Choosing a depth of



This project has received funding from the European Union's Horizon 2020 research and innovation programme under grant agreement No. 700748

integration in Eqs. C1 and C2 corresponds to consider a volume of ground below the groundwater level, that is affected by a change in pore pressure build-up.

The thickness of such a ground layer has been increased from 1 m to 11.5 m (or 15.5 m for the deeper models) and the corresponding efficiency parameters,  $E_{r_u}$  and  $E_{\delta}$ , have been plotted. This allowed a direct comparison between the different models of Table C. 1.

### C.1 MODEL WITHOUT STRUCTURE (SINGLE LAYER)

#### C.1.1 Efficiency in term of $r_u$

Starting from the single layer case, the efficiency in terms of  $r_u$  is plotted in Figure C. 3. It can be observed that in all the cases considered, horizontal drains have a very high efficiency in reducing pore pressure build-up in a layer of ground between 1 and 6 m thick, ranging  $E_{r_u}$  from 0.7 to 0.99. The most efficient configurations appear those characterized by a smaller value of  $s/d$  and  $H'/d$  (i.e. spacing and depth of the first row from the groundwater level).

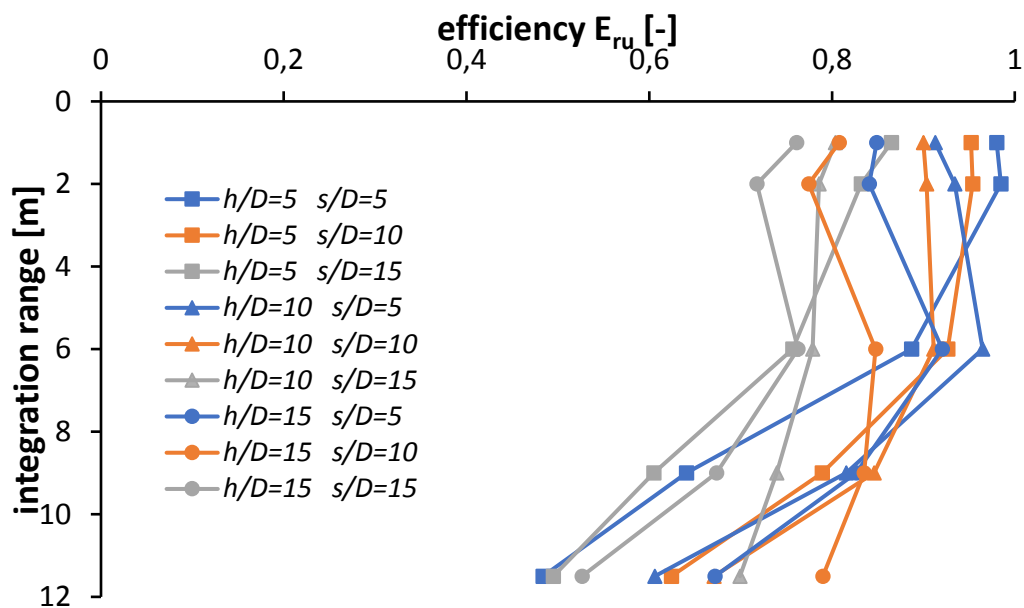


Figure C. 3 - Efficiency in terms of  $r_u$  in free field conditions

The effect of the distance of the base of the model on the numerical solution has been checked, as mentioned in the previous section (§C.2)., by deepening the soil layer from 13m (as in the centrifuge models) to 17 m. The results of both set of analyses are compared in terms of  $E_{r_u}$  in Figure C. 4 (efficiency in the first 2 m below the groundwater level) and Figure



This project has received funding from the European Union's Horizon 2020 research and innovation programme under grant agreement No. 700748

C. 5 (efficiency in the first 11.5 m below the groundwater level, corresponding to the whole model for the layer 13 m deep)

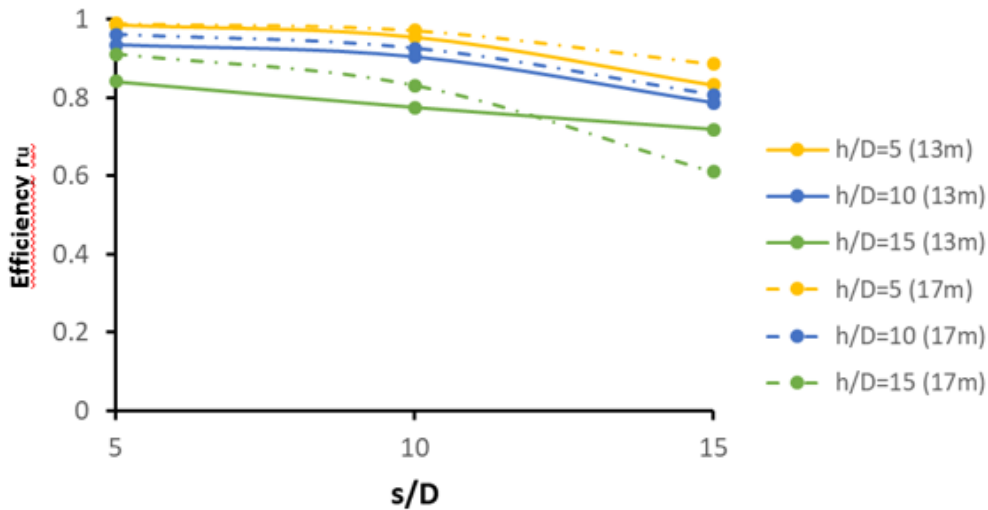


Figure C. 4 - Comparison of  $E_{ru}$  within 2 m from the groundwater level.

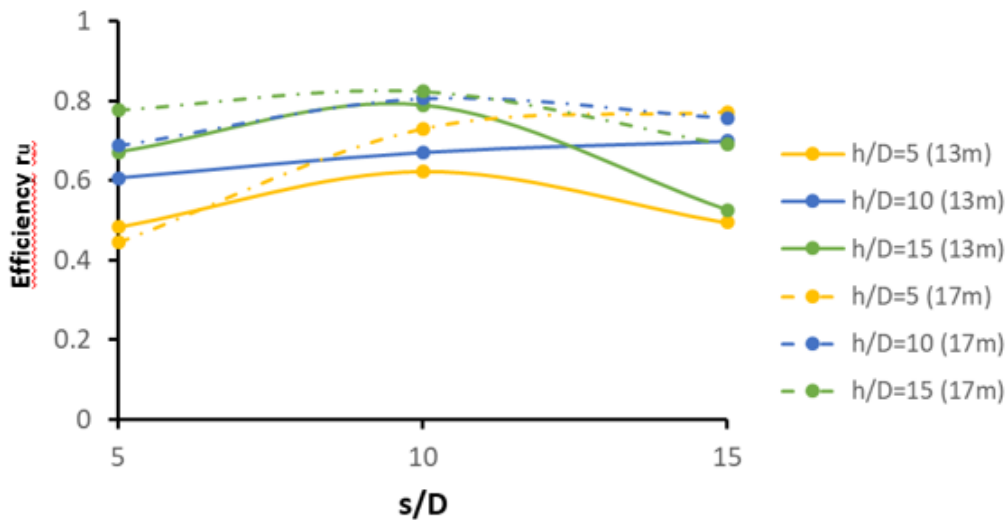


Figure C. 5 - Comparison of  $E_{ru}$  within 11.5 m from the groundwater level.

It is observed that differences between the results of the two sets of models (13 m deep and 17 m deep) are negligible within 2 meters from the groundwater level, especially in the case of  $s/d=5$  and  $H'/d=5$  that resulted the more efficient. Differences tend to increase with depth, however the values of efficiency calculated in the models 13 m deep are generally lower than



This project has received funding from the European Union's Horizon 2020 research and innovation programme under grant agreement No. 700748

in the deeper model (i.e. 17 m deep). It can be concluded that, although somehow affected by boundary effects, the results plotted in Figure C. 3 are on the safe side.

### C.1.2 Efficiency in terms of settlements

On the other hand, in free field conditions the ground surface settlement in the model with drains is larger than in the model without (Figure C. 6). In fact drains allow for large dissipation of excess pore pressure during shaking, that cause large volumetric settlement.

Since a larger influence of the base boundary was observed in some results for the model 13 m deep, in Figure C. 6 only the results pertaining to the model 17 m are shown, being more accurate.

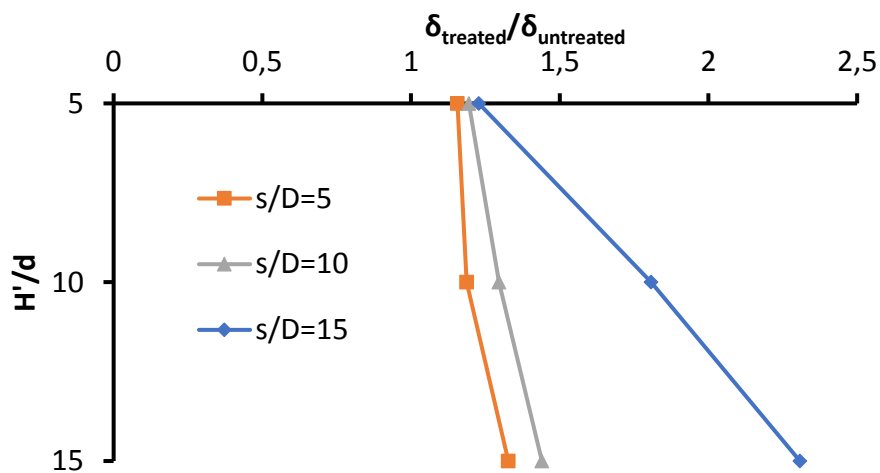


Figure C. 6 - Ratio between the free-field ground surface settlement with drains and without (model 17 m deep)

### C.1.3 Local response

The Figure C.7 shows the response spectra of pseudo-acceleration calculated at surface in the different cases of Table C.1. It is evident that a larger amplification of the spectrum occurs in the models with drains with respect to the case without (black bold line). In fact by preventing soil to liquefy, drains also prevent the creation of an isolating layer i(the liquefied soil). Therefore, larger acceleration can be transmitted at the ground level, compared to the case without drains, where liquefaction occurs.



This project has received funding from the European Union's Horizon 2020 research and innovation programme under grant agreement No. 700748

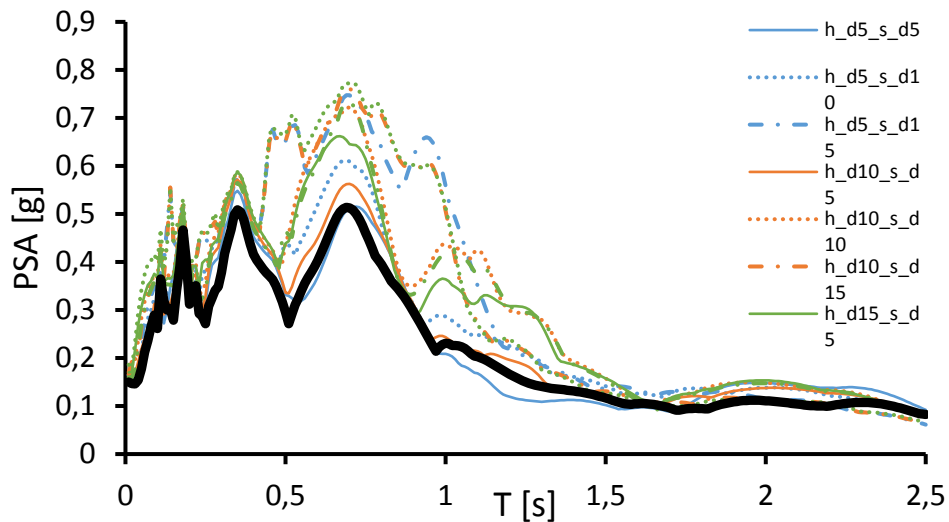


Figure C. 7 - Response spectra of models in free field conditions (13 m model).

However, it can be observed that the configurations with shallower drains, while reducing pore pressure build-up in the shallower layers, do not prevent liquefaction in the underlying deeper layers (see for instance Figure C. 2): in these cases the amplification at the ground level is limited and comparable to the case without drains.

## C.2 MODEL WITHOUT STRUCTURE (DOUBLE LAYER)

### C.2.1 Excess pore pressure ratio: $r_u$

Parametrical analyses were carried out also for the double layer case to study the effect of the presence of a lower permeability soil upon the liquefiable one (crust) on the excess pore pressure ratio distribution.



This project has received funding from the European Union's Horizon 2020 research and innovation programme under grant agreement No. 700748

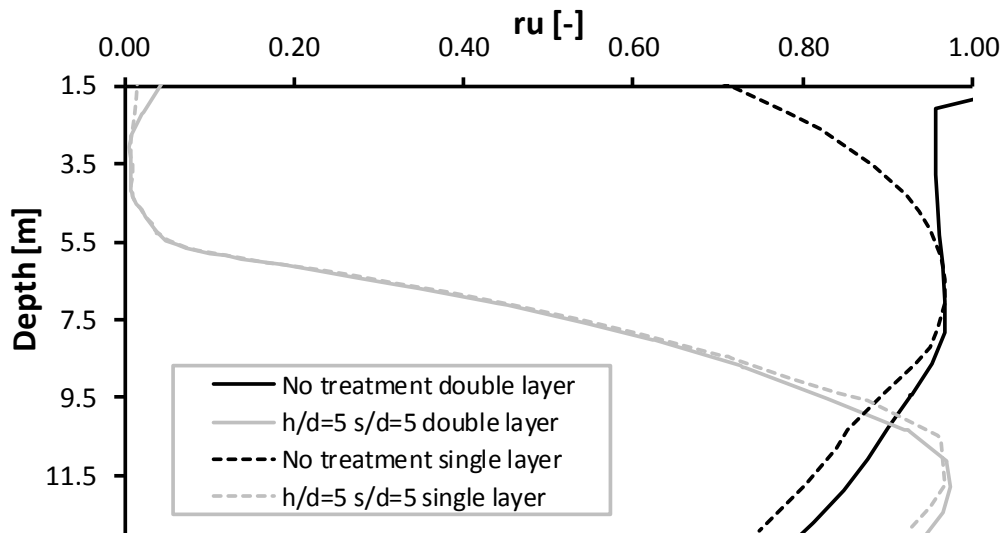


Figure C. 8 – Comparison between envelopes of  $r_u$  for single and double layer.

Figure C. 8 shows the envelopes of the excess pore pressure ratio in the ground. In the double layer configuration without drains (solid black line),  $r_u$  in correspondence of the interface between lower permeability soil and liquefiable soil achieve larger values than in the single layer configuration (dashed black one). This effect is due to the upper boundary that prevents drainage.

By considering the drains system with  $h/d=5$  and  $s/d=5$  the vertical profiles of the calculated  $r_u$  distributions are overlapped (solid gray line and dashed gray one). This result shows that the efficiency of the drain system is large in both cases and the influence of the upper boundary condition is negligible.

However, it is not possible extend this conclusion to all the considered drains layout. Indeed, a deeper arrangement of the drains leads to an increase of the excess pore pressure ratio near the upper boundary, that is larger for the two-layer (crust) configuration. Such effect is considered in the design charts showed in section 5.3.4.

### C.2.2 Efficiency in terms of $r_u$

The profile of efficiency as a function of the interation range is showed in Figure C. 9. The efficiency of system is almost independent by the upper boundary condition and it achieves its maximum value in correspondence of the horizontal drains system.

Figure 5.9



This project has received funding from the European Union's Horizon 2020 research and innovation programme under grant agreement No. 700748

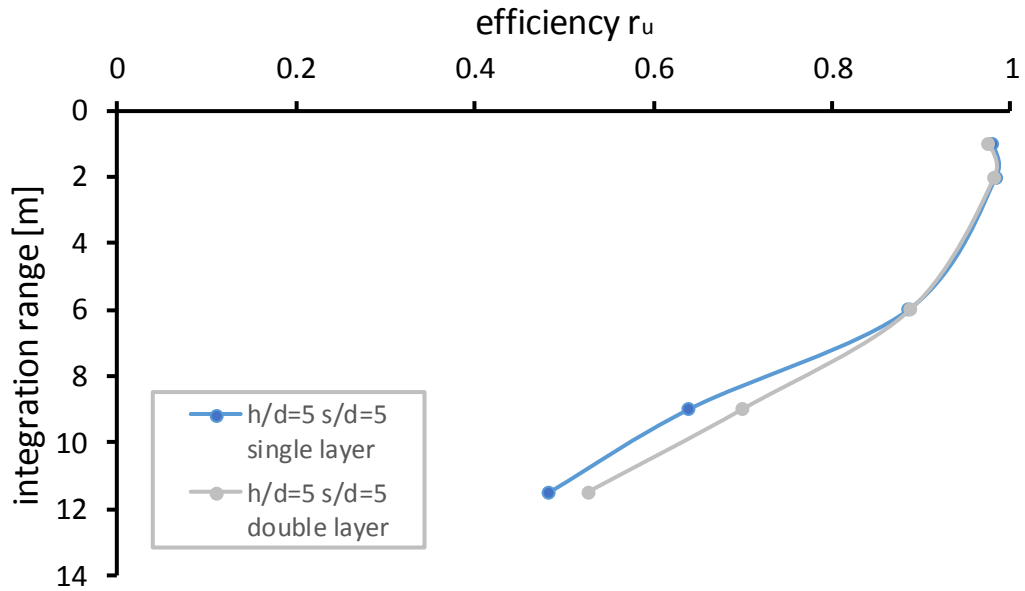


Figure C. 9 - Efficiency in terms of  $r_u$  as a function of the integration range



This project has received funding from the European Union's Horizon 2020 research and innovation programme under grant agreement No. 700748

### C.3 MODELS WITH STRUCTURE (SINGLE LAYER)

#### C.3.1 Efficiency in term of $r_u$

In the models with structure, as shown in Figure C. 10, Figure C. 11 and Figure C. 12 efficiency is still very high. in the considered range of thickness, the most efficient configurations in terms of reduction of  $r_u$  are the shallowest ones, as in the free field case.

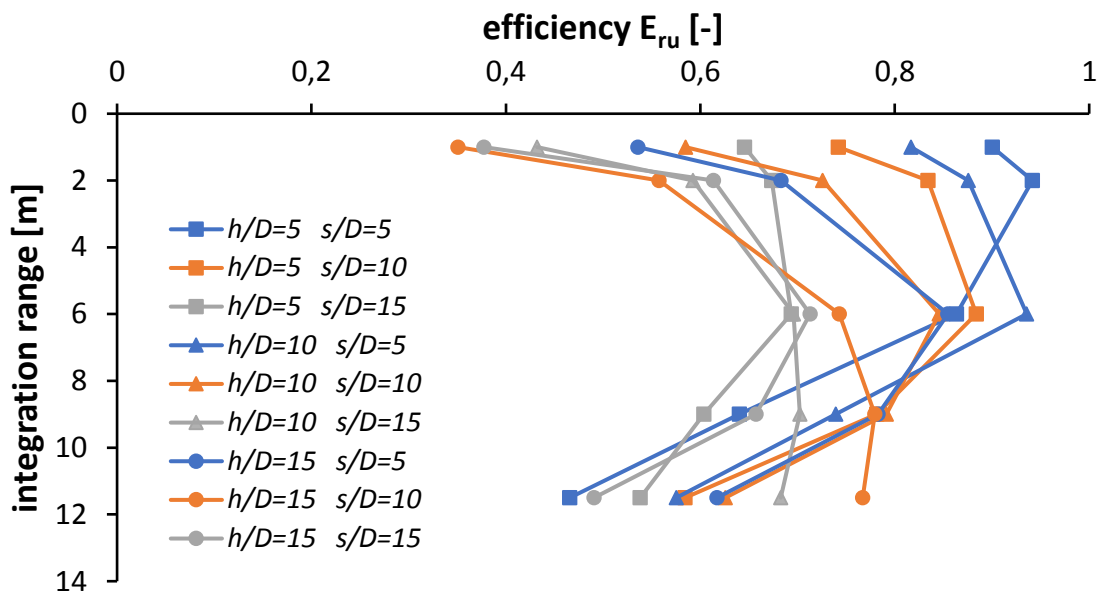


Figure C. 10 - Efficiency in terms of  $r_u$  as a function of the integration range.



This project has received funding from the European Union's Horizon 2020 research and innovation programme under grant agreement No. 700748

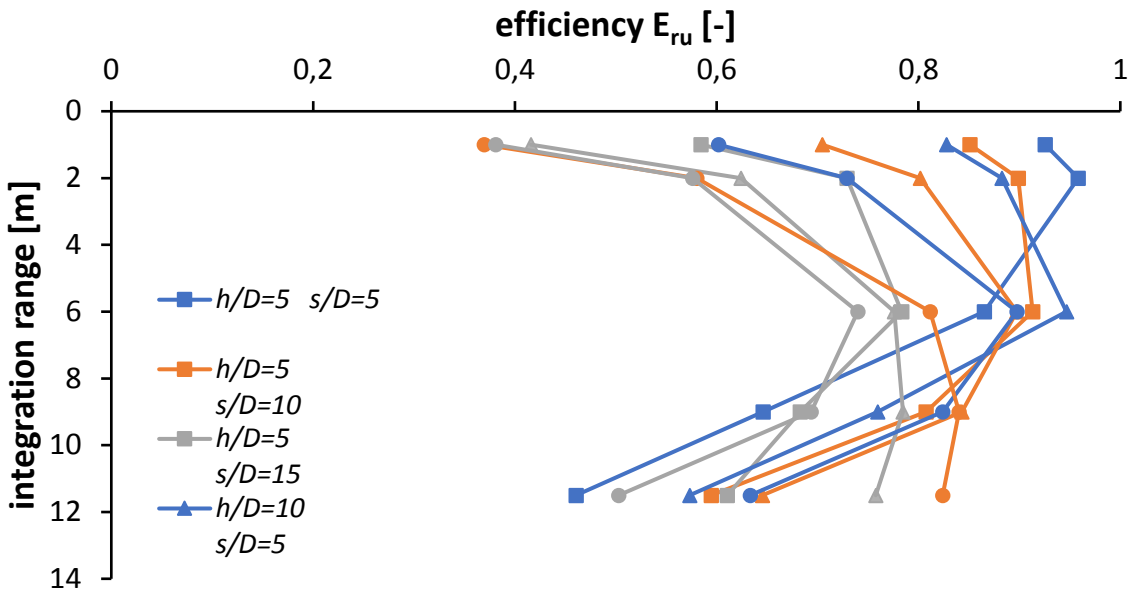


Figure C. 11 - Efficiency in terms of  $r_u$  beneath the structure, along its the vertical axis.

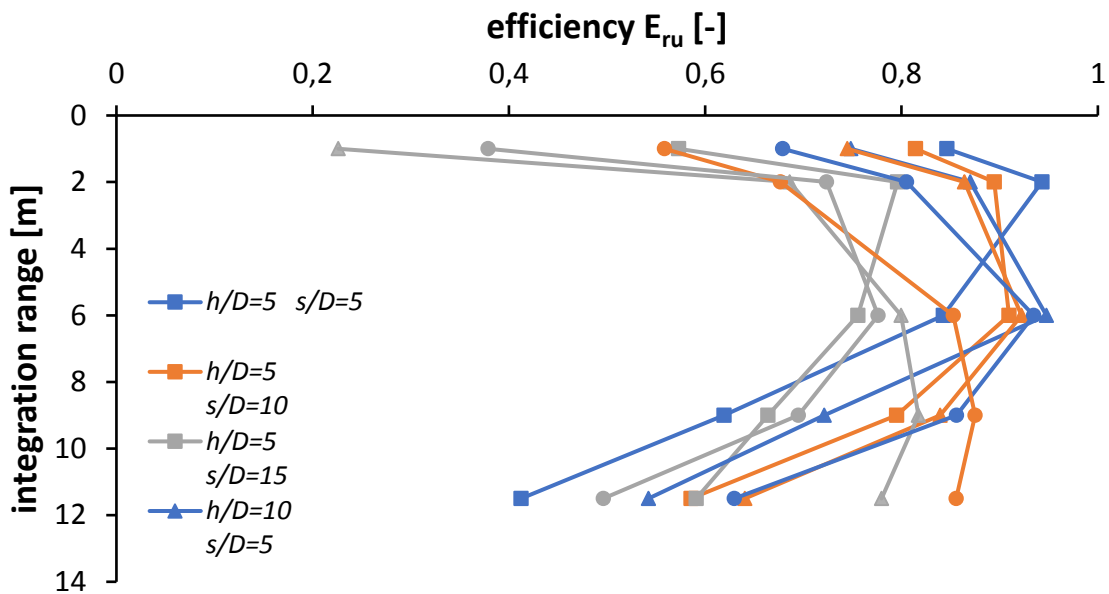


Figure C. 12 - Efficiency in terms of  $r_u$  beneath the foundation beam.

### C.3.2 Efficiency in terms of settlements

The settlements of the building in the model with drains are smaller than those calculated in the model without drains. In fact, while the free-field settlement at ground surface is governed by volumetric strain, thus enhanced by drainage and cyclic consolidation, the



This project has received funding from the European Union's Horizon 2020 research and innovation programme under grant agreement No. 700748

building settlements are mainly governed by the deviatoric strains in the foundation ground, hence reduced by drains, since they prevent pore pressure build-up and soil stiffness reduction. Smaller excess pore pressure is generated and consequently smaller displacement occur. Hence positive values of efficiency in terms of settlements,  $E_{\delta}$ , could be calculated and they are plotted in Figure C.11. A consistent trend is observed in the figure since by increasing both  $s/d$  and  $H'/d$  the efficiency in terms of settlement tends to reduce.

As far as the pseudo-acceleration response spectra at the ground surface are concerned, they are plotted in Figure C.12, confirming what has been already observed for the free-field cases (see Figure C.7).

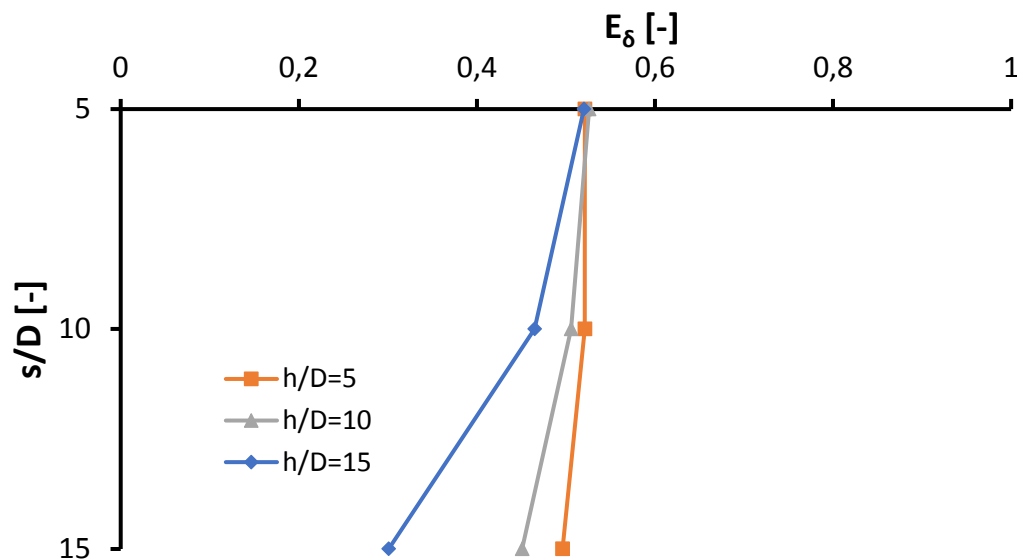


Figure C. 13 - Efficiency in terms of settlement in the models with structure (model 17m deep).

### C.3.3 Local response

The effect on the acceleration spectra on the ground surface is studied. Figure C. 14 shows the response spectra for different dispositions of the horizontal drains. It is possible to see that the peak acceleration is generally higher than the untreated configuration. Maybe this effect is due to the less decrease of soil stiffness due to the presence of the drains.



This project has received funding from the European Union's Horizon 2020 research and innovation programme under grant agreement No. 700748

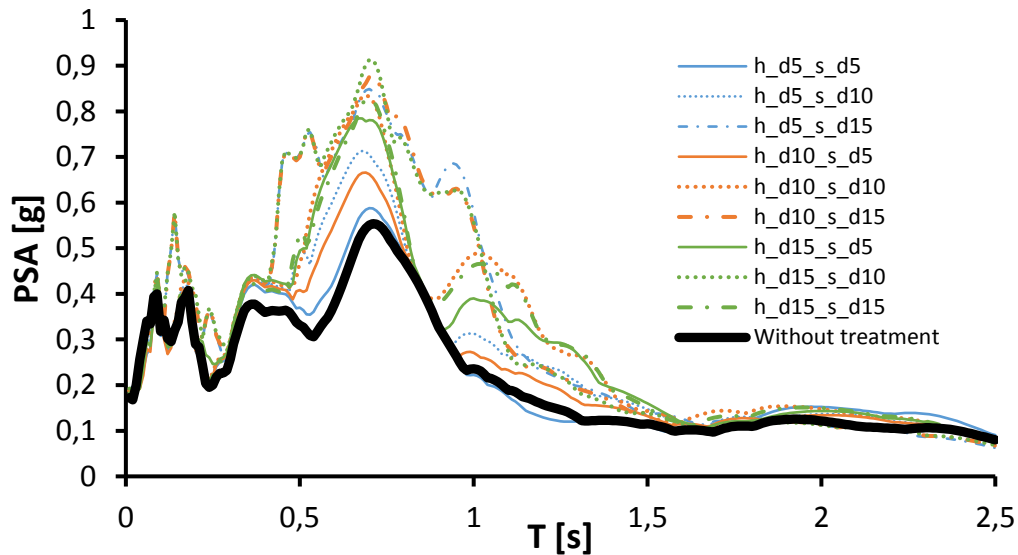


Figure C. 14 - Pseudo-acceleration response spectra at the ground surface of models with structure

#### C.4 COMPARISON BETWEEN EFFICIENCY WITHOUT AND WITH STRUCTURE

The efficiency in terms of  $r_u$  calculated in the without the structure models is compared in Figure C. 15 with that calculated in the models with structure, beneath the foundation beam. For the clarity of representation only a few cases have been plotted in the figure, for which the highest efficiency values were computed (see also Figure C. 3 and Figure C. 12). Moreover, the plot has been limited to the values calculated up to 6 m below the ground water level.

Due to the different distribution of stresses in the two conditions, smaller efficiencies were calculated beneath the foundation beam of the building (dashed lines), than in the free field (continuous lines). Although such differences are the considered cases comprised between 10% and 15% (at most), results may vary in dependence of the loads applied by the building. This suggests a possible limitation in the use of the design charts introduced in section 6, that refer to free field conditions.



This project has received funding from the European Union's Horizon 2020 research and innovation programme under grant agreement No. 700748

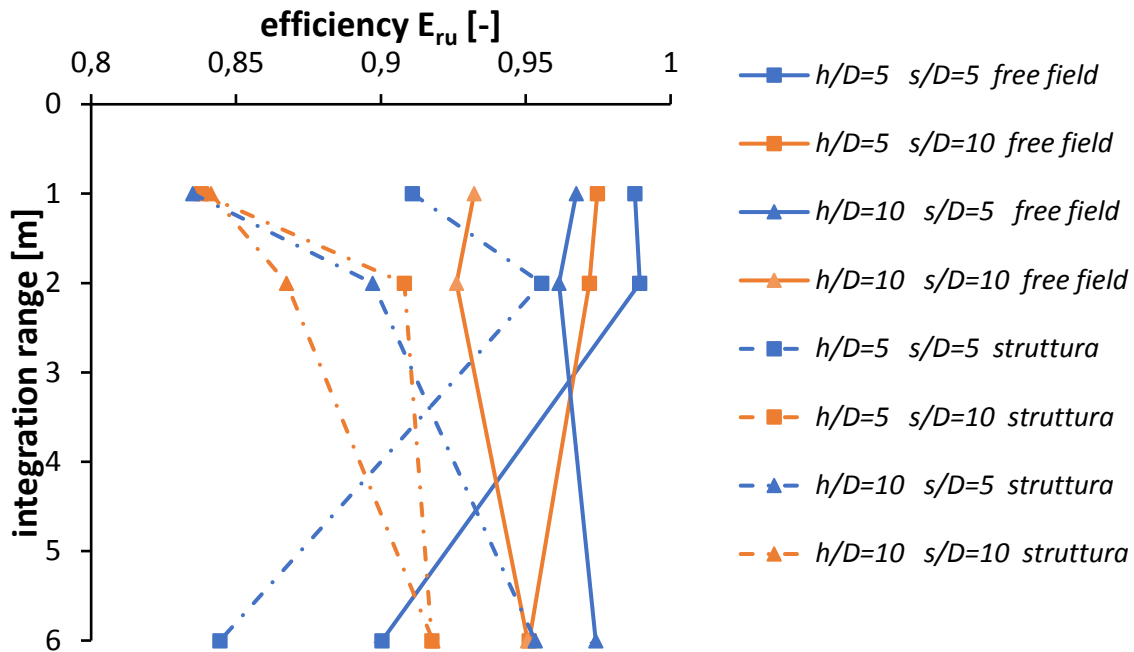


Figure C. 15 - Efficiency comparison in terms of  $r_u$  between the models with structure and free field in the vertical axis foundation beam.

### C.5 EFFECT OF HORIZONTAL EXTENSION OF DRAINAGE SYSTEM

The parametric analyses performed in the previous section were carried out assuming that drainage extends indefinitely in horizontal direction at both sides of the building.

Obviously, this hypothesis conflicts with the applicability of the technique, since it turns out to be an ideal hypothesis and not a real one. Therefore, the need arises to understand effectively which is the minimum extension that must be adopted so that the efficiency of drainage turns out to be the same as that occurring with an indefinite extension of drains.

Starting with an extension limited only to the footprint of the building (configuration 0), the insertion of drains was extended laterally. Three further configurations were analysed, that were obtained by increments equal to  $0.5B$ , where  $B$  indicates the size of the footprint of the building (Figure C. 16).

This study was carried out only for the two most efficient drain configurations, namely  $H'/d = 5$   $s/d = 5$  and  $H'/d = 5$   $s/d = 10$ .



This project has received funding from the European Union's Horizon 2020 research and innovation programme under grant agreement No. 700748

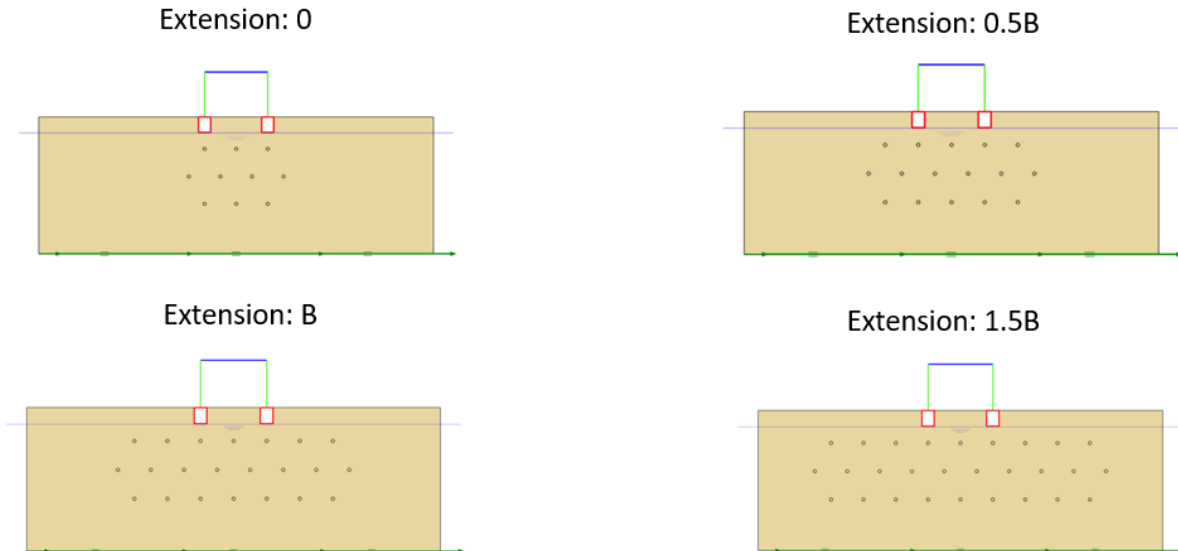


Figure C. 16 - Schemes used to analyse the extension of the drained ground

### C.5.1 Configuration $H'/d=5$ $s/d=5$

For each scheme in Figure C. 16 the efficiency was calculated both in terms of  $r_{ru}$  and of settlement.

Figure C. 17 shows that even with a null extension of the drains from the structure there is an efficiency in terms of reduction of excess pore pressure very close to the case of indefinite extension.

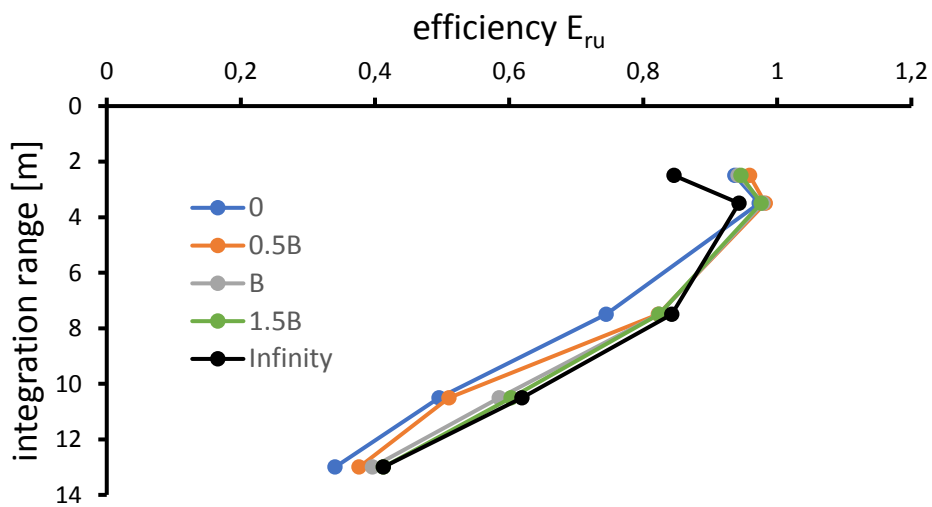


Figure C. 17 - Comparison of the efficiencies  $E_{ru}$  calculated in the various schemes of Figure C.14 for the case  $H'/d=5$   $s/d=5$ .



This project has received funding from the European Union's Horizon 2020 research and innovation programme under grant agreement No. 700748

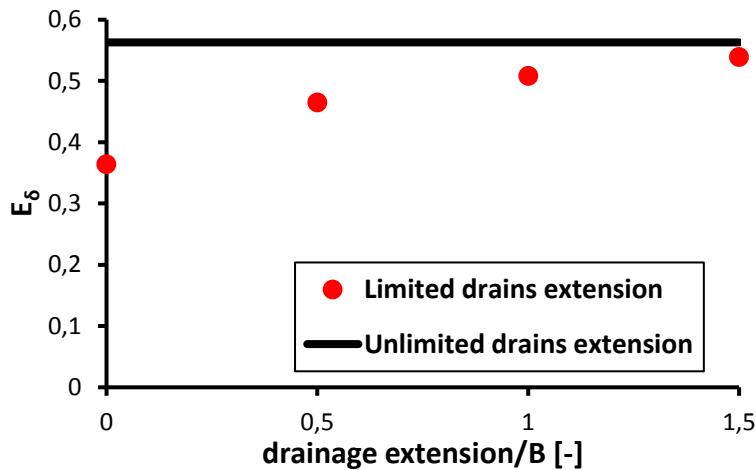


Figure C. 18 - Efficiency in terms of settlement calculated in the various schemes of Figure C. 16 for the case  $H'/d=5$   $s/d=5$ .

As far as the building settlement are concerned, Figure C. 18 shows that the efficiency  $E_s$  increases as long as the lateral extension of the drained ground increases, tending to that achieved in the scheme with an indefinite drainage.

Therefore, looking at the efficiency in terms of settlement, it is possible to say that by extending the drainage to a distance from the building equal to B from it, the reduction of building settlement will be as effective as that provided by an indefinite extension of drains.

### C.5.2 Configuration $H'/d=5$ $s/d=10$

Similar results were obtained for the case  $h/D = 5$  and  $s/D = 10$  (Figure C. 19 and Figure C. 20), leading to the same conclusions.



This project has received funding from the European Union's Horizon 2020 research and innovation programme under grant agreement No. 700748

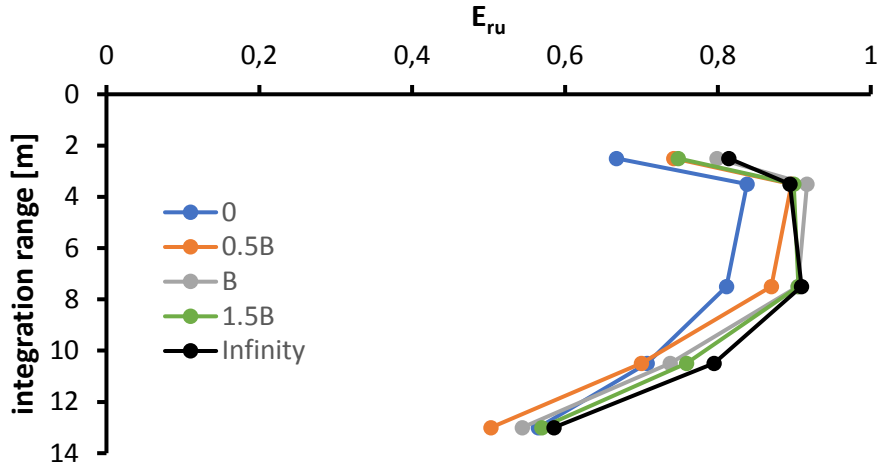


Figure C. 19 - Comparison of the efficiencies  $E_{ru}$  calculated in the various schemes of Figure C.14 for the case  $H'/d=5$   $s/d=10$ .

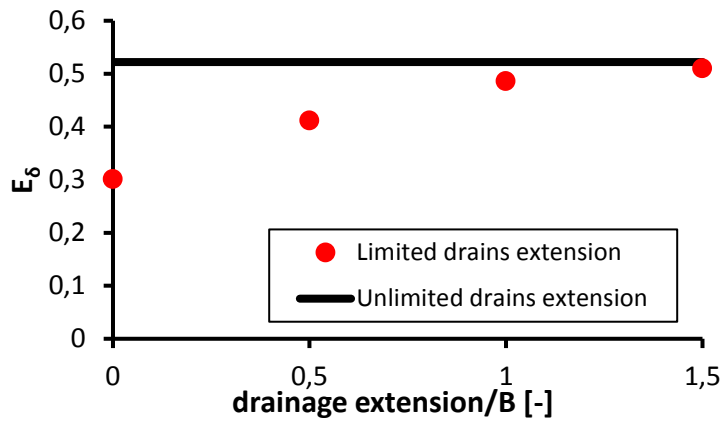


Figure C. 20 - Efficiency in terms of settlement calculated in the various schemes of Figure C.14 for the case  $H'/d=5$   $s/d=10$ .



This project has received funding from the European Union's Horizon 2020 research and innovation programme under grant agreement No. 700748

## Appendix D – IPS PARAMETRIC ANALYSES

A parametric analysis of the effects of induced partial saturation in simplified ground conditions was carried out using the finite element software Plaxis 2D, starting from the configurations that were studied in centrifuge tests (see deliverable D4.2). The constitutive model used for soil is PM4Sand (see deliverable D4.4).

The partial saturated condition induced in a shallow layer of ground, below the groundwater level, was modelled in a simplified way by changing the value of the fluid compressibility as a function of depth and degree of saturation, according to the equation (*Rebata-Landa, Santamarina, 2012*)

$$k_f = \frac{1}{S \frac{1}{k_w} + (1 - S) \frac{3 \cdot r}{2 \cdot T_s}} \quad (D1)$$

where  $S$  is the degree of saturation,  $k_w$  the water compressibility,  $r$  the critical radius and  $T_s$  the surface tension.

The lateral contours were modelled with the tied degree of freedom elements that allow equal movements to nodes at the same depth, in order to reproduce the boundary conditions imposed by the box in centrifuge tests. The groundwater level was set at a depth of 1.5 m. At the base of the model a time history of acceleration was applied. This time history does not correspond to the seismic input used in the centrifuge test (GM31IPS), since it was not able to trigger liquefaction of the soil layer, but to the same GM31IPS amplified by 60%.

Figure D. 1 shows the cyclic resistance curves defined for different degrees of saturation. The curve corresponding to  $S_r=100\%$  (full saturation) matches the relevant experimental curve obtained for the Ticino sand (see calibration of the PM4sand model in Deliverable D4.4). The other curves were obtained by numerical simulation of simple shear tests, where the partial saturation condition was modelled as above described by changing the fluid volumetric compressibility. The resulting curves were compared with those obtained by modifying the curve for  $S_r=100\%$  as a function of the volumetric specific energy corresponding to the relevant degree of saturation  $S_r$ , as described in section 7.3. The comparison showed a good fit between the two sets of curves, indicating that the effect of condition of partial saturation on the cyclic resistance has been correctly simulated within the framework of the Rebata-Landa and Santamarina (2012) approach.

The figure also shows that the considered seismic input action lays above the saturated curve but below other curves corresponding to different degree of saturation, thus indicating the potential for IPS to mitigate pore pressure build-up and prevent liquefaction.



This project has received funding from the European Union's Horizon 2020 research and innovation programme under grant agreement No. 700748

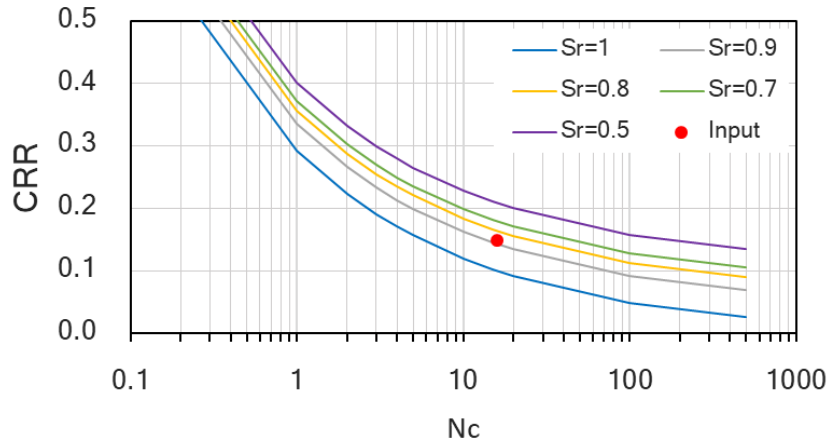


Figure D. 1 - Cyclic resistance curves ( $D_r=52\%$ ,  $\sigma'_{v0}=50$  KPa) with different degree of saturation and point representative of the seismic input (red dot)

#### D.1 ANALYSED SCHEMES

Both in free field conditions and in presence of the structure, the parametric analyses were carried out to investigate the most efficient IPS configuration, from the point of view of both the excess pore pressure ratio and the induced settlements.

Firstly, the model was analysed (with and without structure) without any treatment, to have a reference set of results. Then the thickness of the induced partially saturated layer,  $t_{IPS}$  (Figure D. 2), was varied as summarised in Table D. 1. The size of the structure was kept constant and equal to that of the centrifuge models (see D4.2 and D4.4). The IPS layer is created just below the groundwater level, that is starting from 1.5 m from the ground level.



This project has received funding from the European Union's Horizon 2020 research and innovation programme under grant agreement No. 700748

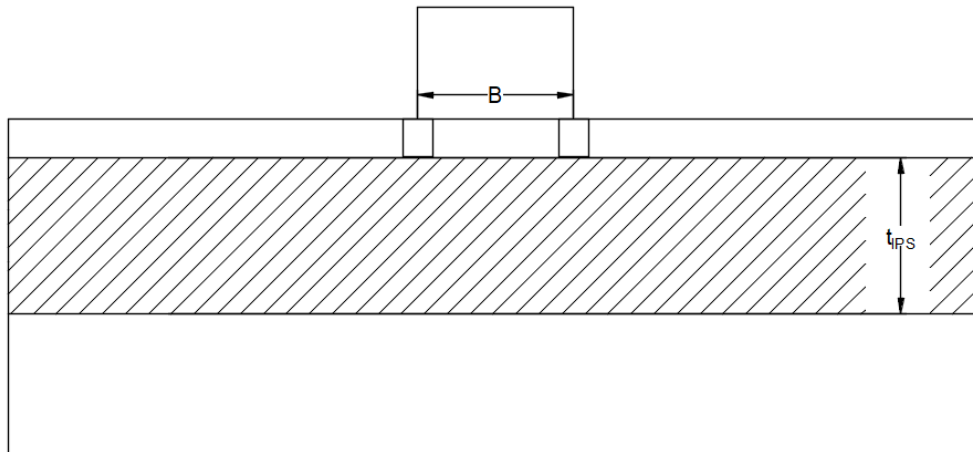


Figure D. 2 - Schematic of the numerical model with framed structure

Table D. 1 - Configurations adopted for parametric analyses

degree of saturation	thickness IPS layer (m)
100%	-
80%	2, 4, 6
85%	4, 6
90%	4, 6
variable	6
100% - 80%	

In Table D. 1, the “variable degree of saturation” case corresponds to the assumption that a variability of the level of desaturation is determined in the ground, depending on the way this is induced. For instance, insufflation from the deepest point (at 7.5 m depth) may induce larger desaturation at depth being less effective close to surface. Hence in this case the desaturated layer was divided in three sub-layers with different degree of saturation, in function of depth and namely:  $S_r = 80\%$  between 5.5 m and 7.5 m,  $S_r = 90\%$  between 3.5 m and 5.5 m,  $S_r = 100\%$  between 1.5 m and 3.5 m.



This project has received funding from the European Union's Horizon 2020 research and innovation programme under grant agreement No. 700748

## D.2 ANALYSES WITHOUT STRUCTURE (SINGLE LAYER)

### D.2.1 Excess pore pressure ratio $r_u$

For each of the configurations in Table D. 1 an envelope of  $r_u$  achieved during shaking in function of depth has been calculated. This envelope refers to the central section of the model and represents the maximum  $r_u$  values of the different considered isochrones. Figure D. 3 shows an example: the curves start from 1.5 m depth, that is the groundwater level depth. In the following,  $r_u$  distribution will be always to be intended as the envelope, unless differently stated.

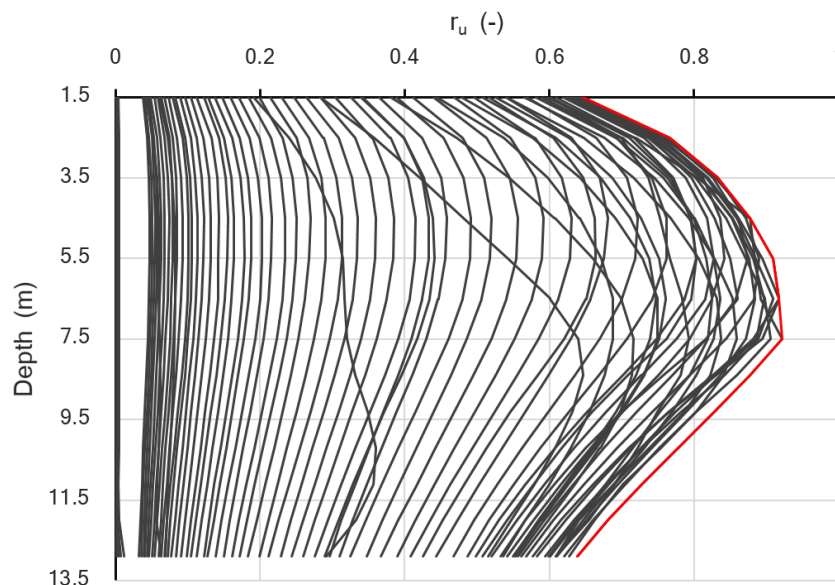


Figure D. 3 - Isochrones of  $r_u$  every 0.5 s (black lines) and maximum envelope (red line)

From Figure D. 4 the  $r_u$  envelopes corresponding to  $S_r=0.8$  and different values of  $t_{IPS}$  are compared. As the treated thickness increases, reduction of the ratio  $r_u$  can be noticed. The greatest reduction occurs when the treatment reaches the depth in which the distribution of  $r_u$  in the untreated case has a maximum (that is where liquefaction is triggered, around 6 m below the groundwater level). Furthermore, it is observed how treating the soil only in the first 2 m below the groundwater level produces a negligible effect.



This project has received funding from the European Union's Horizon 2020 research and innovation programme under grant agreement No. 700748

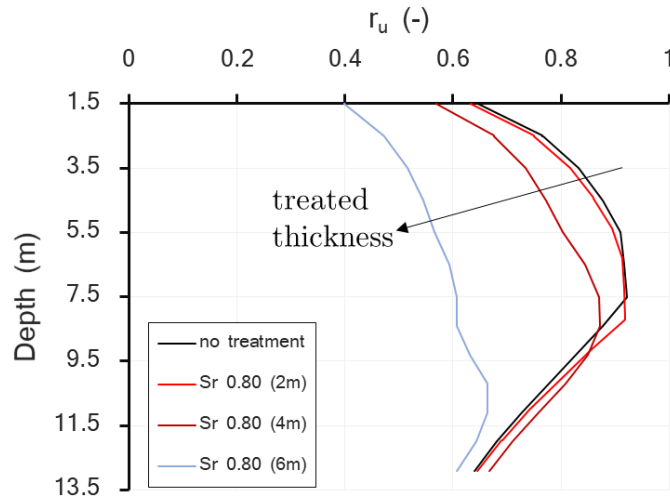


Figure D. 4 - Envelopes of  $r_u$  for different value of the treated thickness,  $t_{IPS}$ .

Since for  $t_{IPS} = 6$  m the largest reduction of  $r_u$  is observed, such a thickness was assumed to investigate the effect of different degree of saturation, according to Table D. 1. The results are shown in Figure D. 5, indicating positive correlation between the reduction of  $S_r$  and the decrease of  $r_u$ .

It is also observed that the distribution of  $r_u$  calculated by assuming a variable distribution of  $S_r$  (between 1 and 0.8) is equivalent to that calculated for a uniform average saturation degree ( $S_r = 0.85$ ). It is worth noting that the weighted average of  $S_r$  in the thickness  $t_{IPS}=6$ m is 0.9, while 0.85 is the weighted average calculated between 3.5 m and 7.5 m. This result confirms the minor influence of the condition of saturation in the upper 2 m of the treated ground layer, as observed in Figure D. 4.



This project has received funding from the European Union's Horizon 2020 research and innovation programme under grant agreement No. 700748

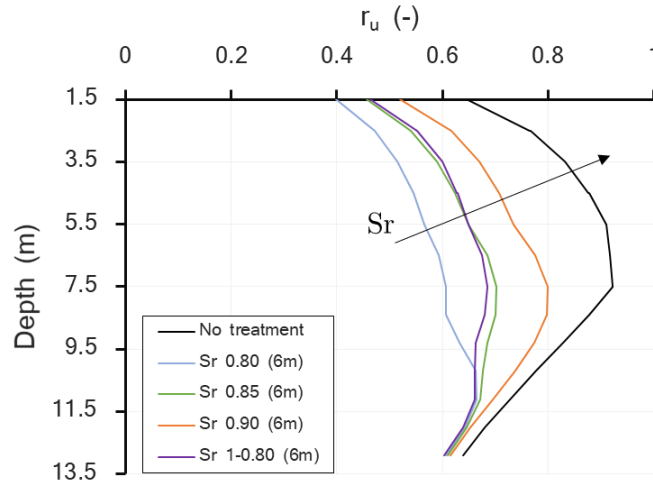


Figure D. 5 - Envelopes of  $r_u$  for different degree of saturation ( $t_{IPS}=6m$ )

### D.2.2 Efficiency in terms of $r_u$

It is possible to consider an efficiency of the treatment both in terms of  $r_u$  and in terms of settlements. In the first case, efficiency can be defined as:

$$E_{r_u} = 1 - \frac{\int_0^z r_{u,desat} dz}{\int_0^z r_{u,sat} dz} \quad (D2)$$

In Figure D.6 the values of  $E_{r_u}$  calculated over different ranges of integration are plotted as a function of such a range. The figure shows that, as already commented above, the curves with higher efficiency are those in which the thickness treatment  $t_{IPS}$  is larger and the liquefying ground layer is reached. Among these, efficiency increases in relation to the level of desaturation induced.

It is also evident, although trivial, that when the integration range is larger than  $t_{IPS}$ , the efficiency decreases, since pore pressure developed in the untreated deeper layers are included in the integration.



This project has received funding from the European Union's Horizon 2020 research and innovation programme under grant agreement No. 700748

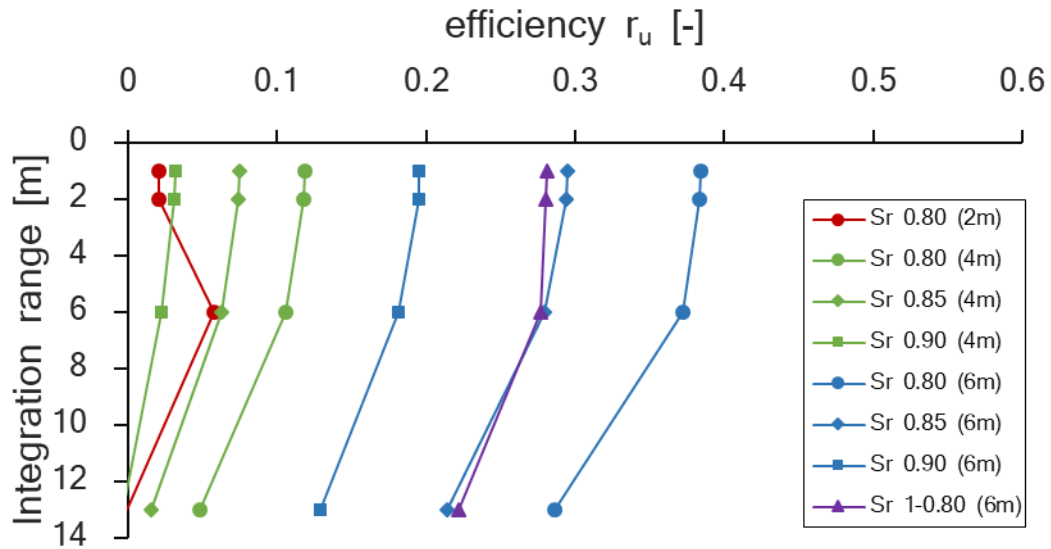


Figure D. 6 - Efficiency in terms of  $r_u$  as a function of the integration range

### D.2.3 Efficiency in terms of settlements

For the settlements it is possible to define the efficiency as:

$$E_\delta = 1 - \frac{\delta_{desat}}{\delta_{sat}} \tag{D3}$$

where  $\delta$  is absolute average settlement calculated at ground level, calculated in the fully saturated model ( $\delta_{sat}$ ) and in each of the analysed desaturated conditions ( $\delta_{desat}$ ).

In Figure D. 7 it is possible to see how for a given  $t_{IPS}$  such an efficiency parameter tends to decrease as the considered degree of saturation increases. Settlements are reduced of about 40% for the more efficient condition  $t_{IPS} = 6$  m  $S_r = 80\%$ .

It should be noted that in free-field conditions the efficiency of IPS calculated in terms of settlements is practically the same as that calculated in terms of  $r_u$ .



This project has received funding from the European Union's Horizon 2020 research and innovation programme under grant agreement No. 700748

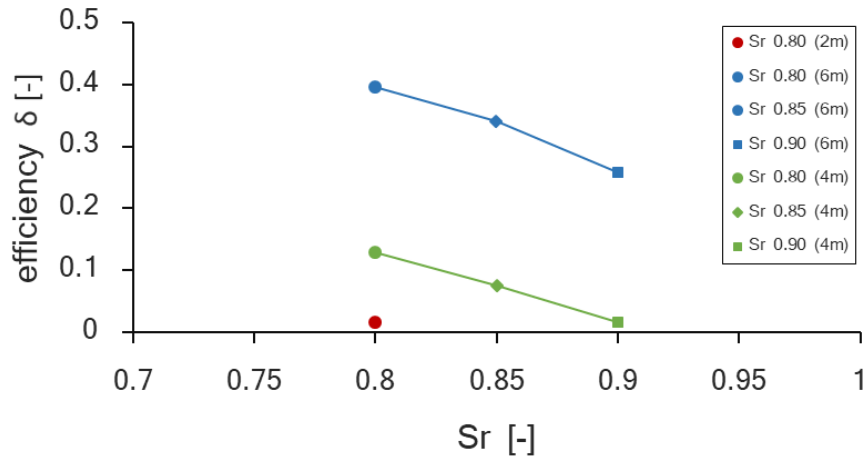


Figure D. 7 - Efficiency in terms of settlements as a function of the degree of saturation.

#### D.2.4 Local response

Another aspect that was taken into account was the effect of desaturation on the local amplification, due to its relevance on the seismic action transmitted at the ground surface. Therefore, the response spectra of pseudo-acceleration and PGA values were compared, for each configuration considered, in Figure D. 8 Figure D. 9.

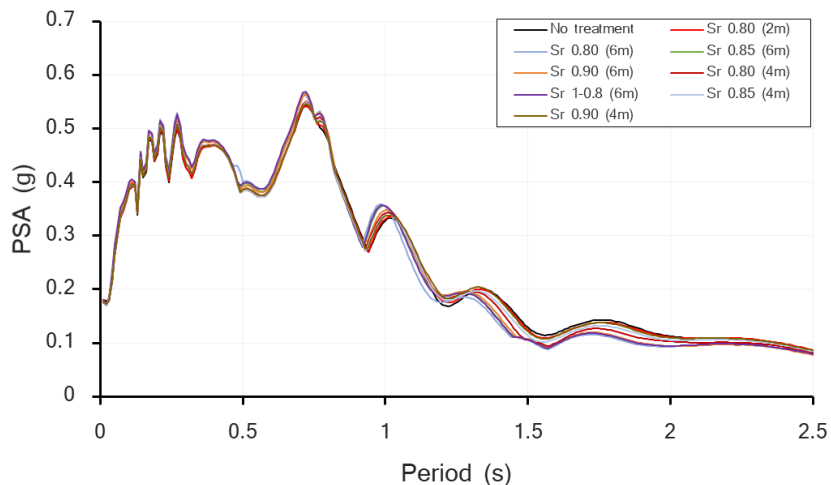


Figure D. 8 - Response spectra of pseudo-acceleration at ground level for all configurations.



This project has received funding from the European Union's Horizon 2020 research and innovation programme under grant agreement No. 700748

From the figures it is possible to observe how the treatment modifies very little the local response of the model, probably due to the fact that it involves a shallow layer of ground, not beyond the 7.5 m of depth, hence it does not affect the pore pressure build-up in the deepest layers (see Figure D. 5 and Figure D. 6) and their dynamic behaviour.

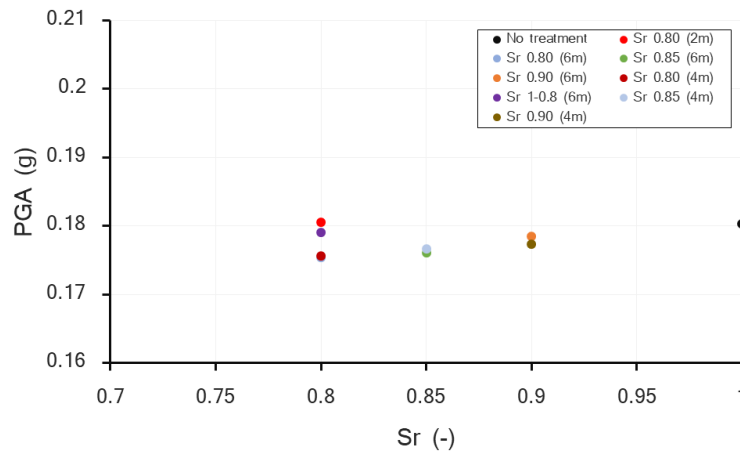


Figure D. 9 - PGA values at ground level for all configurations

### D.3 ANALYSES WITHOUT STRUCTURE (DOUBLE LAYER)

#### D.3.1 Excess pore pressure ratio $r_u$

Parametric analyses were carried out also in a double layer ground conditions. The liquefiable soil lays beneath a low permeability soil layer (crust) which prevents the drainage through the upper boundary.



This project has received funding from the European Union's Horizon 2020 research and innovation programme under grant agreement No. 700748

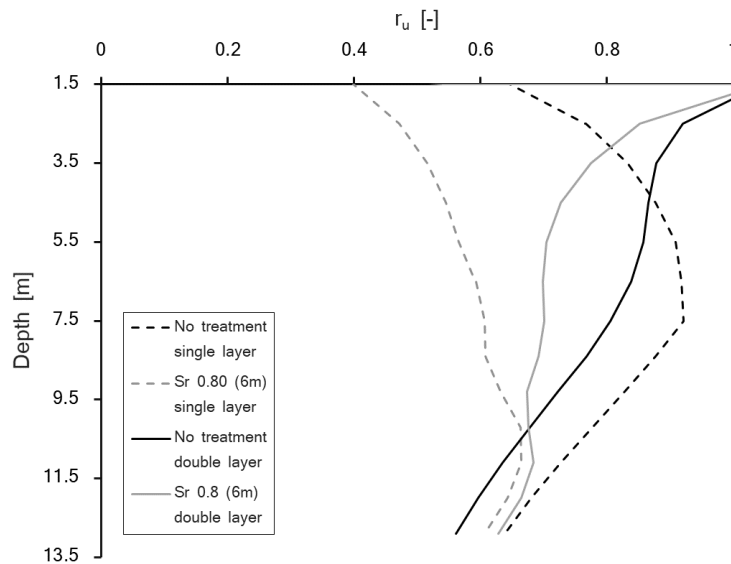


Figure D. 10 – Comparison between envelopes of  $r_u$  for single and double layer layout.

In Figure D. 10 the comparison between envelopes of excess pore pressure ratio with depth is shown. Even though the numerical analyses was carried out on a limited set of conditions, it seems that the presence of the upper low permeability layer has an important effect on the  $r_u$  profiles and this makes IPS less efficient compared to the single layer analysed in the previous section. Since the largest value of  $r_u$  is achieved near the ground surface, this issue should be taken into account in presence of buildings.

### D.3.2 Efficiency in terms of $r_u$

The difference of efficiency of the IPS as a function of the integration range is shown in Figure D. 11.



This project has received funding from the European Union's Horizon 2020 research and innovation programme under grant agreement No. 700748

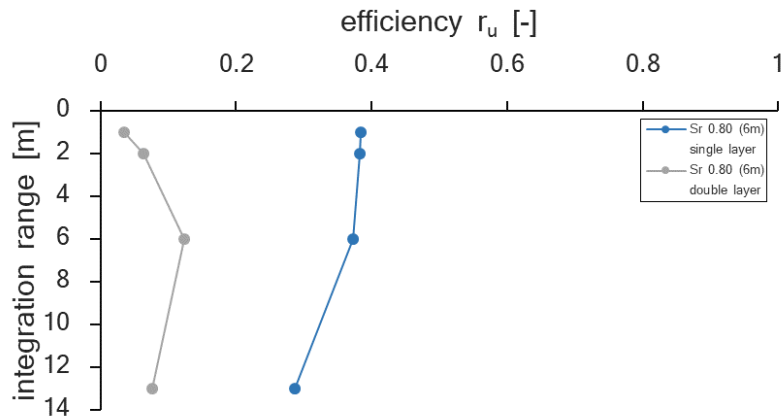


Figure D. 11 – Comparison between efficiency of IPS for single and double layer layout.

#### D.4 ANALYSES WITH STRUCTURE (SINGLE LAYER)

The same configurations considered in the free field conditions were also analysed in the presence of the structure. The results are shown in the following.

##### D.4.1 Excess pore pressure ratio: $r_u$

The envelopes of  $r_u$  shown in Figure D. 12 are calculated in the central section of the model, that is in axis with the structure. Hence, although not directly located beneath the foundation beam, they are affected by the loads applied to the ground by the structure. As a matter of fact, the figure shows that in presence of a structure, in fully saturated conditions liquefaction is not triggered ( $r_{u\max} \approx 0.7$ ).

However, by setting the degree of saturation at 0.8 and varying the thickness  $t_{IPS}$ , a similar decrease of the  $r_u$  was calculated as the thickness  $t_{IPS}$  increases. Hence desaturation shows similar potential in reducing pore pressure build-up also in those cases when excess pore pressure may be detrimental (e.g reducing bearing capacity) although liquefaction is not triggered.



This project has received funding from the European Union's Horizon 2020 research and innovation programme under grant agreement No. 700748

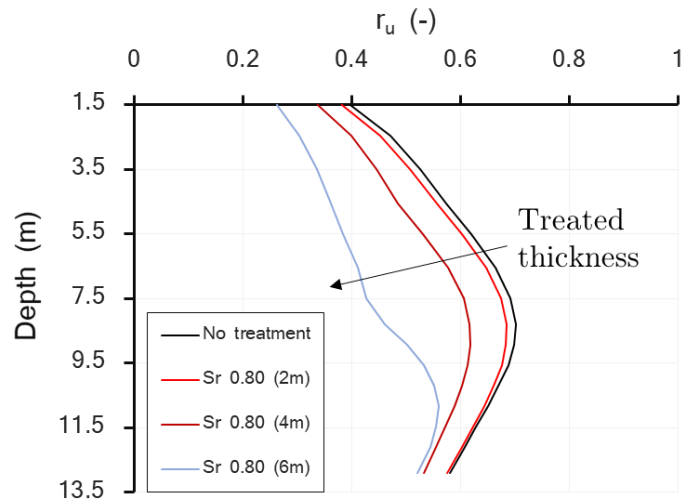


Figure D. 12 - Envelopes of  $r_u$  for different value of the treated thickness,  $t_{IPS}$  (with building)

Then, assuming for treatment the most effective thickness (6 m) and varying the degree of saturation, in presence of the building similar results to free field conditions were obtained, that is a reduction of  $r_u$  when the degree of saturation decreases and comparable behaviour of the two cases of (i)  $S_r$  varying with depth between 1 and 0.8 and (ii) uniform average saturation degree  $S_r = 0.85$  (Figure D. 13)

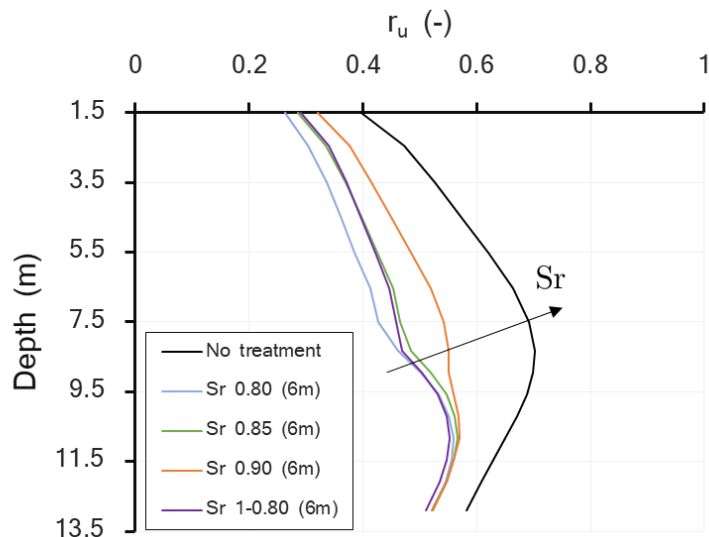


Figure D. 13 - Envelopes of  $r_u$  for different degree of saturation ( $t_{IPS}=6m$ ), with building



This project has received funding from the European Union's Horizon 2020 research and innovation programme under grant agreement No. 700748

### D.4.2 Efficiency in terms of $r_u$

The treatment efficiency in terms of  $r_u$  was calculated and plotted in Figure D. 14. The results fully compare with those obtained in free-field conditions (Figure D. 6).

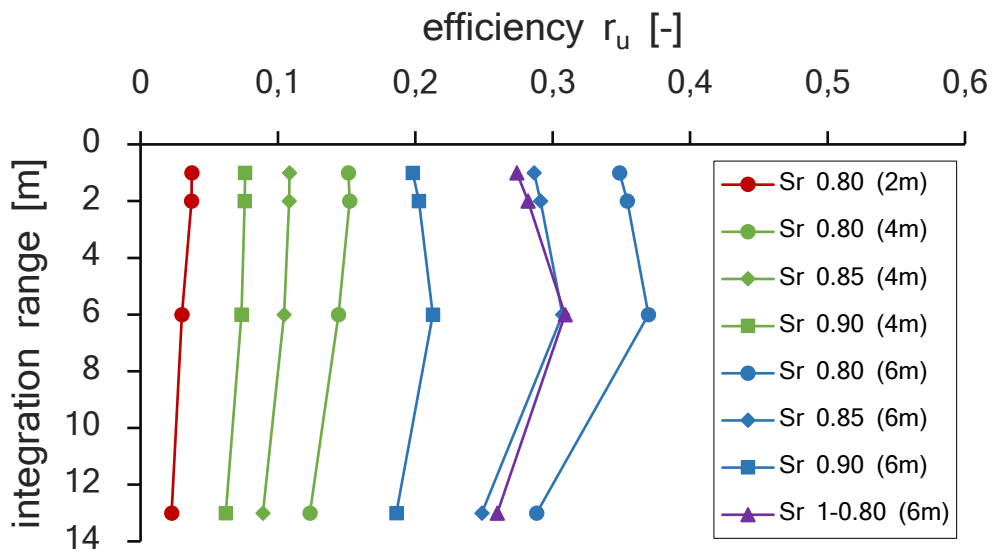


Figure D. 14 - Efficiency in terms of  $r_u$  as a function of the integration range.

### D.4.3 Efficiency in terms of settlements

The efficiency in terms of settlements is shown in Figure D. 15 as a function of the degree of saturation. The same trends as in the free field conditions are confirmed.

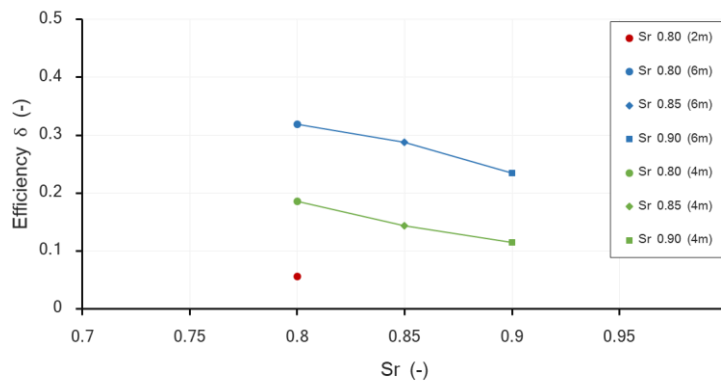


Figure D. 15 - Efficiency in terms of settlements as a function of the degree of saturation.



This project has received funding from the European Union's Horizon 2020 research and innovation programme under grant agreement No. 700748

#### D.4.4 Local response

Finally, also in this case the local response was analysed and both response spectra of pseudo-acceleration at the base of the structure and PGA values were compared, for each configuration considered (Figure D. 16 and Figure D. 17). Figure D. 16 shows that the presence of a structure does not substantially modify the dynamic response of the desaturated models with respect to the untreated case. However, Figure D. 17 shows that PGA at the base of the structure is reduced by decreasing  $S_r$  and by increasing  $t_{IPS}$ . This implies that when the better efficiency is achieved in reducing pore pressure build up (i.e.  $r_u$ ) and the absolute settlement of the building, also the inertial actions on the building are reduced. This conclusion, however, is affected by the assumption that suction was neglected in this study, which is reasonable only in the limited range of desaturation degrees and permeability considered in this case.

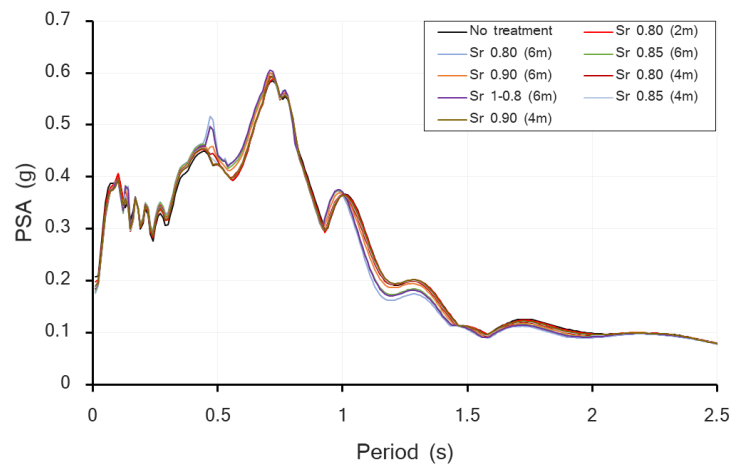


Figure D. 16 - Response spectra at ground level for all configurations.

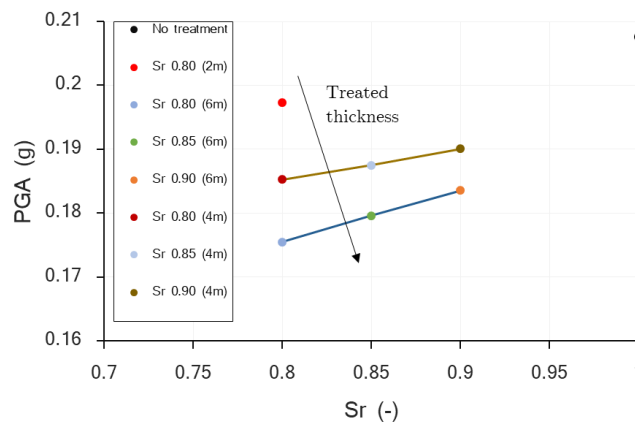


Figure D. 17 - PGA values at the base of the structure for all configurations



This project has received funding from the European Union's Horizon 2020 research and innovation programme under grant agreement No. 700748

### D.5 COMPARISON EFFICIENCY WITH AND WITHOUT STRUCTURE

Once the different configurations have been analysed, both with and without structure, it is possible to compare the efficiency values obtained in terms of  $r_u$ . Figure D. 18 shows that the two values are comparable, being in most cases larger the value achieved in presence of the structure. This would suggest that in the preliminary design of the mitigation action it is conservative to refer to free field conditions.

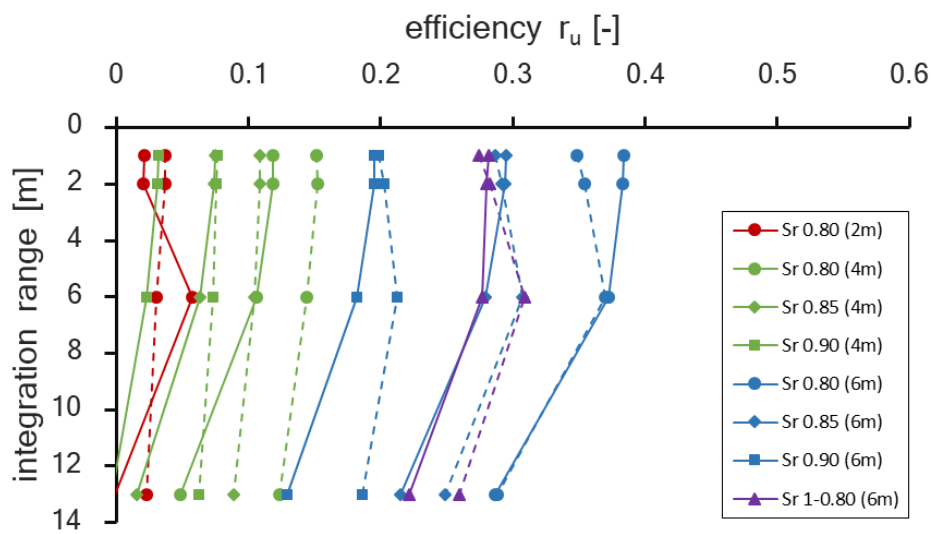


Figure D. 18 - Efficiency in free-field (continuous line) and with structure (dashed line)

### D.6 EFFECT OF HORIZONTAL EXTENSION OF IPS SYSTEM

In the previous sections, the desaturated ground has been assumed as extending indefinitely in the horizontal direction. This is a theoretical assumption that may be impossible to achieve in practice. In order to establish how much the treatment had to be extended laterally with respect to the structure, to obtain similar to those shown for the case of indefinite extension, a number of additional analyses were carried out. In all the additional analyses to the best conditions were modelled:  $S_r = 0.8$  and  $t_{IPS} = 6m$ . A distance  $d_{IPS}$  is defined as the lateral extension of the IPS layer from the building, while  $B$  is the footprint of the building (Figure D. 19). Models with  $d_{IPS}/B$  equal to 0 (IPS only under the building footprint), 0.5, 1.5 and 3 were analysed.



This project has received funding from the European Union's Horizon 2020 research and innovation programme under grant agreement No. 700748

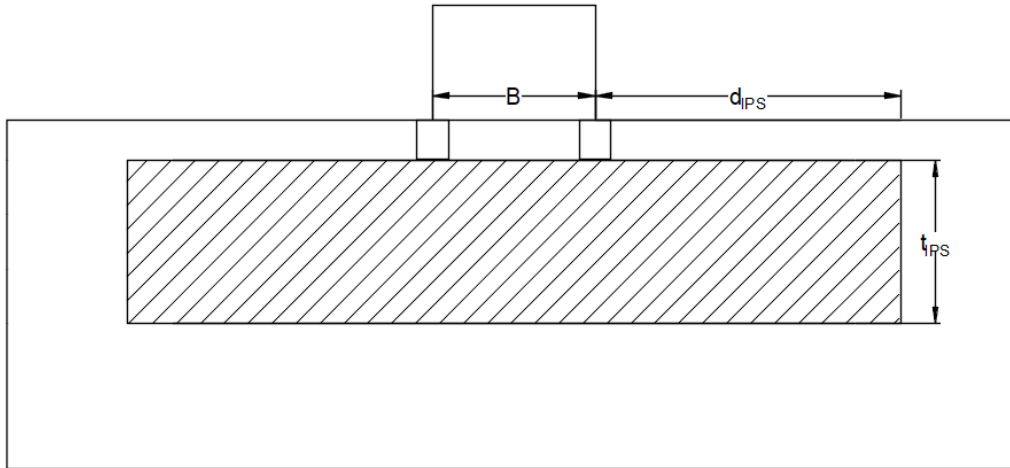


Figure D. 19 - Schematic of the numerical model:  $d_{IPS}$  is the lateral extension of the IPS layer from the building.

### D.6.1 Excess pore pressure ratio: $r_u$

Figure D. 20 plots the distribution of  $r_u$  with depth in the various configurations mentioned above. It can be noticed that, starting from the case without treatment, the excess pore pressure ratio decreases as the lateral extension of the intervention increases, tending towards the infinitely extended layer (this condition coincides in practice with  $d_{IPS}=3B$ ).

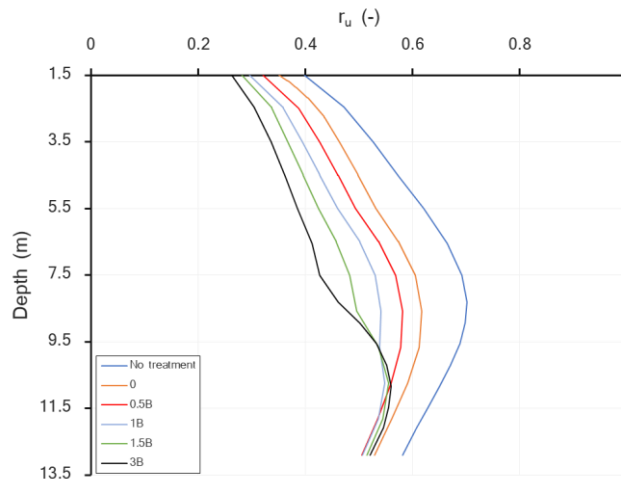


Figure D. 20 - Envelopes of  $r_u$  for different horizontal extension of IPS



This project has received funding from the European Union's Horizon 2020 research and innovation programme under grant agreement No. 700748

### D.6.2 Efficiency in terms of $r_u$

The conclusion can be drawn by plotting the efficiency in terms of  $r_u$  (Figure D. 21). It passes from a value as low as 10% when  $d_{IPS}=0$  (desaturation only below the footprint of the structure) to values of 35%-40%, when  $d_{IPS}= 3B$ .

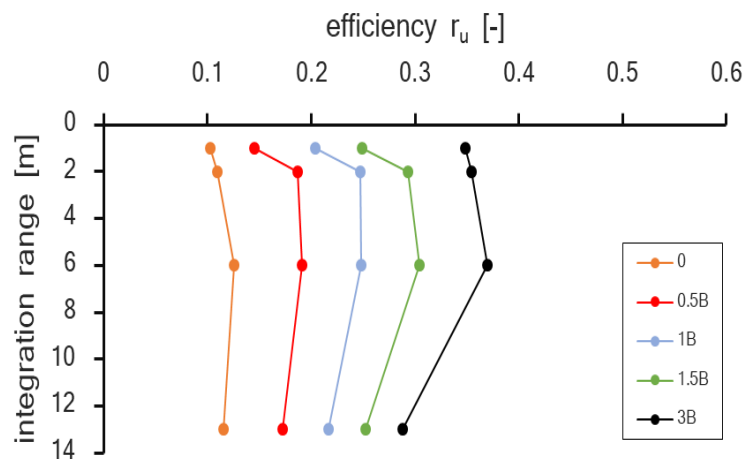


Figure D. 21 - Efficiency in terms of  $r_u$  as a function of the integration range

### D.6.3 Efficiency in terms of settlements

Figure D. 22 confirms that also in terms of settlement reduction a larger lateral extension of the IPS layer entails a greater benefit.

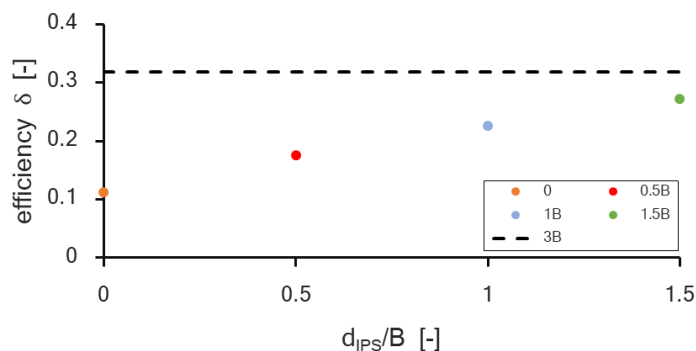


Figure D. 22 - Efficiency in terms of settlement in function of  $d_{IPS}/B$

### D.6.4 Local response

Finally, looking also the effects of the lateral extension of the IPS layer on the local response it can be noted, as shown by the spectra in Figure D. 23, that there are no substantial



This project has received funding from the European Union's Horizon 2020 research and innovation programme under grant agreement No. 700748

differences between the various cases. Up to periods of the order of 1 s, as the lateral extension of the layer increases, the accelerations tend to be reduced. While for periods greater than 1 s a slight amplification is observed.

In terms of PGA, Figure D. 24 shows that a slight reduction in accelerations is observed as the lateral extension of the IPS layer increases.

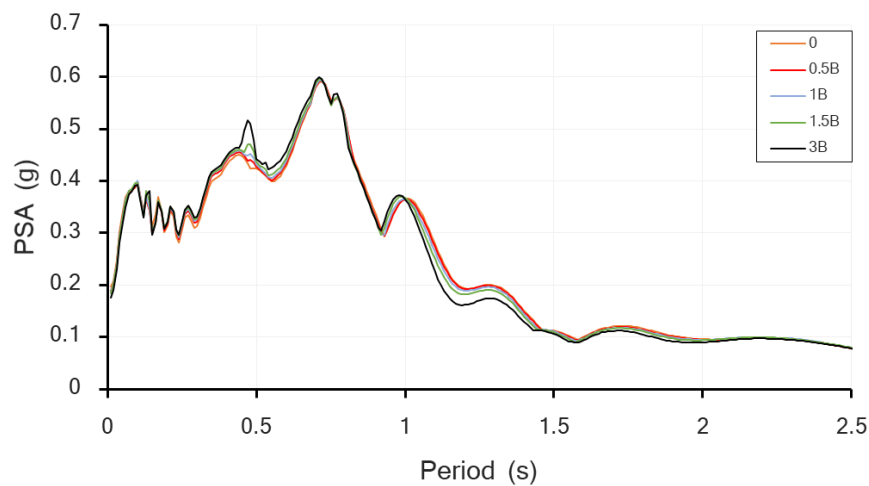


Figure D. 23 - Response spectra at ground level for different value of  $d_{IPS}/B$

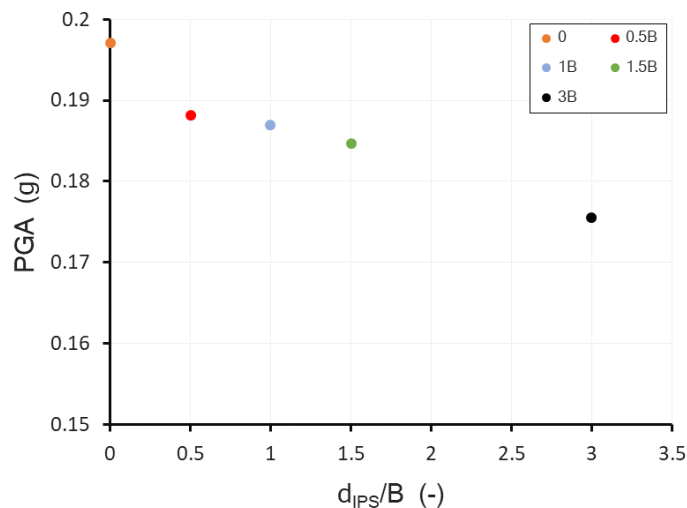


Figure D. 24 - PGA values at the base of the structure for different value of  $d_{IPS}/B$